

# BOSE-EINSTEIN CONDENSATION AND MACROSCOPIC INTERFERENCE WITH ATOMIC TUNNEL ARRAYS

A DISSERTATION  
SUBMITTED TO THE DEPARTMENT OF APPLIED PHYSICS  
AND THE COMMITTEE ON GRADUATE STUDIES  
OF STANFORD UNIVERSITY  
IN PARTIAL FULFILLMENT OF THE REQUIREMENTS  
FOR THE DEGREE OF  
DOCTOR OF PHILOSOPHY

Brian Philip Anderson  
January 2000

© Copyright 2000 by Brian Philip Anderson  
All Rights Reserved

I certify that I have read this dissertation and that in my opinion it is fully adequate, in scope and quality, as a dissertation for the degree of Doctor of Philosophy.

---

Mark Kasevich  
(Principal Adviser)

I certify that I have read this dissertation and that in my opinion it is fully adequate, in scope and quality, as a dissertation for the degree of Doctor of Philosophy.

---

Steven Chu  
(Physics and Applied Physics)

I certify that I have read this dissertation and that in my opinion it is fully adequate, in scope and quality, as a dissertation for the degree of Doctor of Philosophy.

---

Alexander Fetter  
(Physics and Applied Physics)

Approved for the University Committee on Graduate Studies:

# Abstract

Bose-Einstein condensation in a dilute vapor of magnetically trapped  $^{87}\text{Rb}$  was achieved, and the condensed atoms were used to observe de Broglie-wave interference due to atom tunneling between the barriers of an array of traps. The condensed atoms were loaded into a vertically-oriented one-dimensional optical lattice formed by a retro-reflected laser beam, creating the trap array. In the limit of negligible interactions between atoms, the energy difference between adjacent array sites was determined by the gravitational potential energy shift between the sites. This energy difference initiated an oscillating atom mass current similar to an electric current in the ac Josephson effect for two coupled superconductors. In the optical lattice, de Broglie-wave interference occurred between atoms in localized lattice states, and the interference was observed as a train of falling pulses of atoms.

In a separate experiment, using a dilute vapor of lithium, enhanced loading of a  $^7\text{Li}$  magneto-optic trap with spectrally-broadened cooling and trapping light was demonstrated. By placing the Li oven nozzle near the trap, the Li atoms could be efficiently captured from an atomic beam without using a pre-cooling stage. The trapped atoms were transferred into a three-dimensional optical lattice, formed by four intersecting and interfering beams of far-off-resonant laser light, and adiabatic cooling and velocity selection in three dimensions was demonstrated.

# Acknowledgements

I sincerely thank my advisor, Mark Kasevich, for his guidance and suggestions during the course of this work. His exceptional insight and creativity have been indispensable, and I am privileged to have had the opportunity to work closely with him for more than six years.

I also thank my colleagues for assistance with various projects and for many beneficial discussions, especially Todd Gustavson, Jeff McGuirk, Brent Young, Heun Jin Lee, and Alastair Sinclair. I owe special thanks to Masami Yasuda for help with data collection in the final stages of this work, and for keeping the research alive while I worked on this dissertation; to Ken Sherwin for help with numerous diverse tasks at Stanford; and to Randy Hulet for initially nudging me in the direction of Stanford University.

This work was made much more fulfilling by the many fantastic people that have helped cultivate my life beyond the lab. I have particularly enjoyed innumerable interesting and humorous conversations and enterprises with Todd Gustavson, as well as the company of Doug Smith during countless hikes and adventures in California's great outdoors. I am also especially appreciative of close friendships with Jennifer Breitzmann, Monica Davis, Kristin Gustavson, and Donnasue Graesser, who have provided substance to my life as a graduate student.

I am deeply grateful to my family, especially my parents, for their ceaseless and unlimited love and support. I particularly thank my aunt and uncle, Dorothy and Bill Farrell, and my cousins, Billy and Carla, Petrice, and Shannon, for helping to make my time in New Haven enjoyable, warm, and memorable.

# Contents

<b>Abstract</b>	<b>iv</b>
<b>Acknowledgements</b>	<b>v</b>
<b>1 Introduction</b>	<b>1</b>
1.1 Contemporary atomic physics . . . . .	1
1.2 Format of this dissertation . . . . .	3
<b>2 Cooling and trapping neutral atoms</b>	<b>6</b>
2.1 Background . . . . .	6
2.1.1 Atoms in external fields . . . . .	6
2.1.2 Laser cooling . . . . .	7
2.1.3 Bose-Einstein condensation . . . . .	7
2.2 Atom-photon interactions . . . . .	7
2.2.1 The two-level atom . . . . .	7
2.2.2 Doppler cooling . . . . .	11
2.2.3 Beyond the two-level atom model . . . . .	12
2.2.4 Optical pumping . . . . .	12
2.2.5 Lithium and Rubidium . . . . .	13
2.3 Magneto-optic traps . . . . .	13
2.4 Optical traps . . . . .	16
2.4.1 Dipole forces . . . . .	16
2.4.2 Optical lattices . . . . .	17
2.5 Magnetic traps . . . . .	18

2.5.1	Spherical-quadrupole trap . . . . .	19
2.5.2	Time-averaged orbiting potential trap . . . . .	20
2.6	Evaporative cooling . . . . .	22
2.7	Bose-Einstein condensation . . . . .	25
2.8	Consolidation of techniques . . . . .	28
<b>3</b>	<b>Enhanced loading of a <math>^7\text{Li}</math> magneto-optic trap</b>	<b>29</b>
3.1	Motivation . . . . .	29
3.2	Direct loading from an atomic beam . . . . .	30
3.2.1	Experimental considerations . . . . .	31
3.2.2	Trap capture velocity . . . . .	32
3.3	Experimental setup . . . . .	33
3.4	Spectrally-broadened laser light . . . . .	36
3.5	Trap images . . . . .	41
3.6	Summary . . . . .	41
<b>4</b>	<b>Trapping <math>^7\text{Li}</math> in an optical lattice</b>	<b>44</b>
4.1	Motivation . . . . .	44
4.2	A far-detuned optical lattice for Li . . . . .	45
4.3	Experiment . . . . .	46
4.3.1	Apparatus . . . . .	46
4.3.2	Experimental sequence . . . . .	51
4.3.3	Trap loss . . . . .	53
4.4	Velocity selection and adiabatic cooling . . . . .	55
4.5	Summary . . . . .	56
<b>5</b>	<b>Light-induced atom desorption</b>	<b>58</b>
5.1	Motivation: BEC . . . . .	58
5.2	Vapor cell magneto-optic traps . . . . .	59
5.3	Experiment . . . . .	61
5.3.1	Lasers . . . . .	62
5.3.2	Rb vapor cell . . . . .	62

5.3.3	Light-assisted losses . . . . .	63
5.3.4	The Rb MOT . . . . .	63
5.3.5	White light source . . . . .	64
5.3.6	Measurements . . . . .	64
5.4	Modeling the effects of the white light source . . . . .	67
5.5	Assessing the gains of LIAD . . . . .	73
5.5.1	Observations . . . . .	73
5.5.2	Extension of the technique to other atomic species . . . . .	73
5.5.3	Caution . . . . .	73
5.6	Summary . . . . .	74
<b>6</b>	<b>Bose-Einstein condensation of <math>^{87}\text{Rb}</math></b>	<b>75</b>
6.1	Motivation . . . . .	75
6.2	Experimental approach to BEC . . . . .	76
6.3	Apparatus . . . . .	76
6.3.1	Lasers . . . . .	76
6.3.2	Vacuum system . . . . .	77
6.3.3	DC magnetic-field bias coils . . . . .	79
6.3.4	Spherical-quadrupole field coils . . . . .	80
6.3.5	TOP field coils . . . . .	82
6.3.6	RF coil . . . . .	84
6.3.7	Timing system . . . . .	84
6.4	Sequence . . . . .	84
6.4.1	Dark MOT . . . . .	86
6.4.2	Transfer to magnetic trap . . . . .	86
6.4.3	TOP-induced evaporative cooling . . . . .	88
6.4.4	Magnetic trap imaging . . . . .	90
6.4.5	RF evaporative cooling: reaching the BEC threshold . . . . .	92
6.5	BEC measurements and images . . . . .	94
6.6	BEC results . . . . .	98
6.7	On-resonance dark-ground imaging . . . . .	101



6.8	Calibrations, systematic errors, and measurement uncertainties . . . .	102
6.8.1	Imaging system . . . . .	102
6.8.2	Magnetic fields . . . . .	107
6.8.3	Laser light . . . . .	108
6.8.4	Random noise and fluctuations . . . . .	109
6.8.5	Error analysis . . . . .	109
6.8.6	Limitations . . . . .	109
6.9	Apparatus improvements . . . . .	111
6.10	Summary . . . . .	113
<b>7</b>	<b>Atomic tunnel arrays</b>	<b>114</b>
7.1	Introduction . . . . .	114
7.2	Josephson effects in superconductors . . . . .	114
7.3	General approach . . . . .	116
7.4	Atomic tunnel array: theory . . . . .	117
7.4.1	Model system . . . . .	117
7.4.2	Quantum calculation . . . . .	120
7.4.3	Interband tunneling . . . . .	122
7.5	Trapping a BEC in an optical lattice . . . . .	123
7.6	Atomic tunnel array: observations . . . . .	124
7.6.1	Low Intensity lattice . . . . .	124
7.6.2	High-intensity lattice . . . . .	128
7.6.3	Hold and Release . . . . .	129
7.6.4	Dephasing and loss of coherence . . . . .	132
7.6.5	Multiple traps . . . . .	134
7.6.6	Launching pulses upwards . . . . .	136
7.6.7	Pulses in a harmonic potential . . . . .	137
7.7	Atomic tunnel array: applications . . . . .	138
7.7.1	Measurements of weak forces . . . . .	138
7.7.2	BEC optical trapping experiments . . . . .	138
7.7.3	Atom laser . . . . .	139

7.8	Future improvements . . . . .	139
7.9	Summary . . . . .	140
<b>8</b>	<b>Conclusions</b>	<b>141</b>
<b>A</b>	<b>Characteristics of <math>^7\text{Li}</math> and <math>^{87}\text{Rb}</math></b>	<b>144</b>
<b>B</b>	<b>Josephson effects and Bloch oscillations</b>	<b>147</b>
	<b>Bibliography</b>	<b>152</b>

# List of Tables

5.1	Rb loading and recovery characteristics with induced desorbtion . . .	66
6.1	Relative measurement uncertainties of magnetic trap characteristics .	110
A.1	Properties of Li and Rb. . . . .	144

# List of Figures

2.1	Atom absorption and emission of photons . . . . .	9
2.2	A typical MOT experimental setup . . . . .	15
2.3	Representation of spherical-quadrupole trap . . . . .	19
2.4	Representation of TOP trap magnetic field . . . . .	21
2.5	General evaporative cooling schematic . . . . .	24
2.6	RF evaporative cooling between hyperfine sublevels . . . . .	25
3.1	Illustration of the apparatus used to cool and trap $^7\text{Li}$ . . . . .	31
3.2	Calculated Li loading rate <i>vs.</i> laser power . . . . .	34
3.3	Acceleration <i>vs.</i> velocity for Li cooling . . . . .	35
3.4	Measured Li loading rates . . . . .	37
3.5	Li trap loss rate <i>vs.</i> intensity . . . . .	40
3.6	Images of Li atoms in a comb-loaded MOT . . . . .	42
3.7	Super-lattice type images of Li atoms in a comb-loaded MOT . . . . .	43
4.1	Structure of the red-detuned Li lattice . . . . .	47
4.2	Interference pattern for red-detuned Li lattice . . . . .	48
4.3	Interference pattern for blue-detuned Li lattice . . . . .	49
4.4	A red-detuned Li dipole trap . . . . .	52
4.5	Number of atoms remaining in Li lattice <i>vs.</i> confinement time . . . . .	53
4.6	Li lattice band structure and calculated particle motion . . . . .	54
5.1	Illustration of Rb apparatus for LIAD . . . . .	62
5.2	Rb trap loading with and without WLS . . . . .	65

5.3	Timing sequence for Rb LIAD experiments and calculations . . . . .	68
5.4	Calculated number-lifetime products with modulated partial pressure . . . . .	71
5.5	Variation of number-lifetime products in time . . . . .	72
6.1	A top view of the Rb BEC atom trapping chamber . . . . .	78
6.2	The Rb vacuum chamber . . . . .	80
6.3	Spherical-quadrupole magnetic field coils circuit diagram . . . . .	82
6.4	The TOP magnetic field coils . . . . .	83
6.5	Schematic view of the Rb experimental apparatus . . . . .	85
6.6	Characteristics of the TOP evaporative cooling ramp . . . . .	89
6.7	The BEC production sequence . . . . .	93
6.8	BEC absorption images . . . . .	94
6.9	Images showing the BEC transition with absorption imaging . . . . .	95
6.10	TOP-induced evaporative cooling compared to rf-induced cooling . . . . .	97
6.11	Condensate fraction <i>vs.</i> $T/T_C(N)$ . . . . .	99
6.12	The BEC transition, with on-resonance dark-ground imaging . . . . .	103
6.13	BEC optical density cross sections, with ODI . . . . .	104
6.14	Small-number BEC image . . . . .	105
7.1	Effective optical plus gravitational potential for the Rb optical trap . . . . .	118
7.2	Calculated atomic tunnel array output . . . . .	119
7.3	Bloch oscillations in the periodic potential . . . . .	121
7.4	The optical trapping experimental setup . . . . .	124
7.5	An illustration of the vertical periodic potential for the optical trap . . . . .	125
7.6	Images of atom pulses from the atomic tunnel array . . . . .	126
7.7	Atom pulses for trap depths of $\sim E_R$ . . . . .	127
7.8	Cross section of image of atom pulses . . . . .	128
7.9	Time development of ballistic expansion momentum components . . . . .	130
7.10	Calculated velocity distribution for various spatial configurations . . . . .	131
7.11	Time-of-flight absorption images: hold and release . . . . .	132
7.12	Loss of coherence of tunnel array output . . . . .	133
7.13	Images of multiple-traps in the optical lattice . . . . .	134

7.14	The formation of multiple-traps . . . . .	135
7.15	Atom pulses launched upwards . . . . .	136
7.16	Atom pulse train in harmonic potential well . . . . .	137
A.1	The energy level structure of $^7\text{Li}$ . . . . .	145
A.2	The energy level structure of $^{87}\text{Rb}$ . . . . .	146

# Chapter 1

## Introduction

### 1.1 Contemporary atomic physics

While atomic physics research encompasses theoretical and experimental work in many diverse areas, the sub-fields of neutral-atom cooling and trapping are specifically concerned with methods that dissipate kinetic energy from atoms in an atomic gas, techniques for confining cold atoms to small and well localized spatial volumes, and investigations into the properties of cold or trapped atoms. Atom cooling and trapping techniques have advanced considerably not only in the last 15 years, but also quite significantly in the last 5 years, contributing to many recent notable achievements in atomic physics.

Laser-cooling techniques encompass methods by which momentum can be removed from atoms and ions by interaction with photons from laser beams. Doppler cooling, one aspect of laser cooling that will be discussed in this dissertation, was theoretically described in 1975 by T. Hänsch and A. Schawlow [1] and independently by D. Wineland and H. Dehmelt [2], and was first demonstrated experimentally by a group led by S. Chu at AT&T Bell Labs in 1985 that achieved temperatures of  $\sim 240 \mu\text{K}$  for a dilute sodium vapor [3]. Subsequent experiments led by W. Phillips at NBS (now NIST)<sup>1</sup> demonstrated much lower temperatures [4], and further theoretical analysis by C. Cohen-Tannoudji [5] and independently by Chu [6] revealed the

---

<sup>1</sup>National Bureau of Standards (now National Institute of Standards and Technology)

mechanisms by which the colder temperatures could result. Building on the ideas of laser cooling, a trap that could conveniently cool as well as localize atoms was created in 1987 [7]. This magneto-optic trap, as it was called, was realized with the addition of a magnetic field gradient to the laser cooling beams.

Laser cooling and magneto-optic trapping techniques have been useful in applications such as precision measurements of fundamental constants [8], precision measurements of the earth's rotation [9] and gravity gradients [10], nano-fabrication with neutral atoms [11], precision frequency standards [12, 13], and studies of collisions between atoms [14]. The techniques have allowed atoms to be trapped in periodic structures formed by laser light [15, 16], trapped in focused beams of laser light [17], bounced off of light fields [18], guided through hollow fibers [19], and split and recombined interferometrically [20], to cite just a few examples. Because of the numerous applications and the rapid growth of the techniques, the original experimental achievements were recognized in 1997 by the awarding of the Nobel prize in Physics to Chu, Phillips, and Cohen-Tannoudji for their “development of methods to cool and trap atoms with laser light” [21].

In 1995, a major goal of experimental physics was reached by the achievement of Bose-Einstein condensation in a dilute gas, a system in which many particles occupy the quantum-mechanical ground state of an external potential well. The unique state of matter was first created in a rubidium vapor by the group led by E. Cornell at JILA [22], followed by condensate creation with lithium by the group of R. Hulet at Rice University [23], and with sodium under the direction of W. Ketterle at MIT [24]. To date, 17 groups have obtained condensation, including condensation of hydrogen by D. Kleppner's group at MIT [25]. With the exception of the hydrogen experiment, laser cooling techniques were used in each of these experiments.

Current theoretical and experimental investigations of atomic-gas Bose-Einstein condensation encompass many areas, including the pursuit of quantum many-body characteristics of dilute gas Bose-Einstein condensates similar to observed properties of superfluids, superconductors, and lasers. Research pursued in our group, first at Stanford University and continued at Yale University, has included the search for



quantum many-body effects in lithium and Bose-Einstein condensation with rubidium. We developed techniques which enabled us to efficiently pursue these goals, and in 1997 we achieved condensation of  $^{87}\text{Rb}$  at Stanford. After relocating at Yale University, we again achieved condensation of Rb in 1998. We used the condensed atoms to study effects of de Broglie-wave tunneling upon confinement of condensed atoms in a periodic potential, drawing links between the observed atom behavior and mode-locked lasers and Josephson junctions.

## 1.2 Format of this dissertation

The experiments described in this dissertation represent six years of atomic physics research. While working towards completion of these experiments, we investigated many new and different experimental techniques. The individual experiments presented here were focused on (i) increasing the loading efficiency of atoms into magneto-optic traps, (ii) studying properties of atoms in periodic optical traps, and (iii) studying characteristics and applications of atomic-gas Bose-Einstein condensation. The goals of our experimental efforts were to reach high atomic densities and cold temperatures and observe signatures of bosonic quantum many-body effects.

The first experiments described here were intended as a foundation for detection of quantum many-body effects between pairs of lithium atoms. Similar to the experiment of Hanbury Brown and Twiss [26] with photons from star light, the goal of the lithium work was to observe an enhancement in the detection probability of pairs of (bosonic)  $^7\text{Li}$  atoms within a small volume of phase-space after their initial release from a different region in phase-space. The enhancement of the pair-detection probability for thermal bosons is a purely quantum mechanical phenomenon, and originates in the facts that the atoms are indistinguishable, and the dual wavefunction describing the propagation of an atom pair must be symmetric upon interchange of the particle labels.

While the ongoing search for these effects in lithium is not described in this thesis, experiments which demonstrated either an increase in the number and density of trapped atoms or a decrease in temperature are described. Such conditions are

necessary for detecting quantum many-body effects in atomic vapors. These accomplishments were achieved with two main innovations: (i) a broadening of the frequency spectrum of the light used to load atoms into a magneto-optic trap, described in Chapter 3 (with excerpts from Ref. [27], copyright 1994 by the American Physical Society), and (ii) adiabatic cooling of Li atoms trapped in an optical lattice, described in Chapter 4 (with excerpts from Ref. [28], copyright 1996 by the American Physical Society). The frequency broadening technique proved very useful, and is currently in use as the search for Li quantum many-body effects continues in our laboratory. Although we detected adiabatic cooling in an optical lattice, the loss in number of trapped atoms outweighed the benefits of colder temperatures. However, the work was significant for the demonstrations of atom trapping in optical lattices formed with far-off-resonance laser beams. On its own, this achievement merits discussion. Yet it is made even more relevant by our subsequent work with Bose-Einstein condensed Rb atoms in an optical standing wave, and serves as an interesting complement to the Rb experiments.

The experiments with Rb were focused on achievement of Bose-Einstein condensation in a dilute atomic vapor and on trapping the condensed atoms in an optical standing wave. Chapter 5 is devoted to a method that we explored with the intent of increasing the loading efficiency of Rb atoms into a vapor cell magneto-optic trap [29]. The technique required the use of an external source of white light from a fiber optic illuminator. When light was directed into the vapor cell and onto an inner wall of the vacuum chamber, we observed an increase in the vapor pressure of Rb atoms due to Rb desorption directly from the walls of the chamber. With this method, we were able to modulate the vapor pressure such that the number of trapped atoms was increased without shortening the lifetime of atoms in a magnetic trap in the same vacuum cell.

Our successful route to condensation is described in Chapter 6 (with excerpts from Ref. [30], copyright 1999 by the American Physical Society), as are techniques used to measure the characteristics of the condensates *in situ*. A detailed account is given of the cooling and trapping techniques used to reach the condensation threshold, and a dark-ground imaging technique with light tuned to the atomic resonance is described.

Chapter 7 is focused on a set of experiments in which a Bose-Einstein condensate was loaded into a standing wave optical trap [31]. The results of the experiment revealed a connection between the behavior of the degenerate atoms in the vapor and properties of superfluidity and superconductivity.

# Chapter 2

## Cooling and trapping neutral atoms

### 2.1 Background

This chapter is an introduction to the main topics and experiments discussed in this dissertation. The focus is on physical concepts, with technical details deferred to the relevant chapters of this thesis and in Appendix A. Due to the significant advances in the fields of atom cooling and trapping that have been made in the last decade, many recent references are available for more detailed information.

#### 2.1.1 Atoms in external fields

Atoms from a thermal beam or vapor have been cooled and trapped in ultra-high vacuum environments by a variety of methods, including techniques based on elastic collisions between atoms and a cold helium buffer gas [32]. However, the most prevalent techniques involved in current atom trapping and cooling experiments rely on the interactions of atoms with external electric and magnetic fields, which can remove kinetic energy from a sample of atoms and trap atoms by perturbing and manipulating the internal energy levels of the atoms.

### 2.1.2 Laser cooling

Our primary methods to trap and cool a dilute vapor of neutral atoms relied on laser cooling [1, 3] and the magneto-optic trap (MOT) [7, 33]. With laser cooling, precisely tuned laser light decreases the velocity of atoms in a vapor or beam via momentum exchange with laser photons. The cold atoms can be captured and localized within the vacuum chamber with the addition of a magnetic field gradient. Laser cooling is discussed in section 2.2. Atom traps, including the MOT, are described in sections 2.3 through 2.5.

### 2.1.3 Bose-Einstein condensation

Bose-Einstein condensation is a quantum mechanical state of matter that occurs in trapped samples of bosons at temperatures below a density-dependent critical limit. Below this threshold, a large number of particles in the sample occupy the ground state of the system, comprising the Bose-Einstein condensate (BEC). To date, two experiments have reached the condensation threshold by directly loading atoms into a magnetic trap without using a magneto-optic trapping stage (the Li [23] and H [25] experiments). In all other successful BEC experiments with atomic gases, the BEC is created by first capturing atoms with a MOT, and transferring the atoms into a magnetic trap prior to further cooling. Other groups are pursuing condensation through various other means, such as in purely optical traps [34]. Once atoms have been confined in a magnetic trap, the route to BEC is achieved through evaporative cooling techniques [35, 36], discussed in section 2.6. The physical principles of Bose-Einstein condensation are discussed in section 2.7.

## 2.2 Atom-photon interactions

### 2.2.1 The two-level atom

A hypothetical two-level atom can exist either in an energy ground state or in an excited state [37]. With an energy difference  $\hbar\omega_0$  between the two states, transitions

between the states can be induced by radiation at a frequency  $\omega$  near  $\omega_0$ , the transition resonance frequency. If the resonance  $\omega_0$  lies near the optical range, such as for alkali atoms, the electric field of a laser can be used to stimulate a ground state atom into making a transition to the excited state. The excited atom will subsequently either spontaneously fall back to the ground state (by *spontaneous emission* of a photon), or be stimulated by the external light field to return to the ground state (by *stimulated emission* of a photon) [38]. In both processes, the atom emits a photon as it returns to the ground state, releasing the energy gained in the absorption process into either the external laser field (via stimulated emission) or an arbitrary mode (via spontaneous emission).

Because a photon carries momentum  $\hbar k$ , where  $k = 2\pi/\lambda$  and  $\lambda$  is the wavelength of the light, an atom receives a momentum kick in the direction of photon propagation upon photon absorption. A second momentum kick, or photon recoil, is imparted to the atom as it emits a photon. Conservation of momentum between an atom and the light field is illustrated in Fig. 2.1. Over many absorption and emission events, an atom receives numerous momentum kicks in a single direction due to absorption from a laser beam. If after each photon-absorption event, the atom emits photons due to stimulated emission, the recoil kicks due to emission will balance the absorption momentum kicks. In this section, we will consider the cases in which the atom emits spontaneously, where the direction of the emitted photons is arbitrary and essentially random, and the associated *emission* momentum kicks average to zero. All net momentum transfer is thus due to *absorption* of the laser light. In this case, a light beam has a net force - the *scattering force*  $\mathbf{f}_{scat}$  - that acts on the atom. The *rate* of photon absorption and emission and the strength of the laser field determine the strength of the force. The direction of the force is in the direction of laser beam propagation.

An atom can spend up to half of the time in an excited state, and therefore the probability  $p_e$  of detecting the atom in an excited state is at most  $p_e = 1/2$ . The mean total time of the atom-photon scattering process,  $\tau_{scat}$ , is then the product of

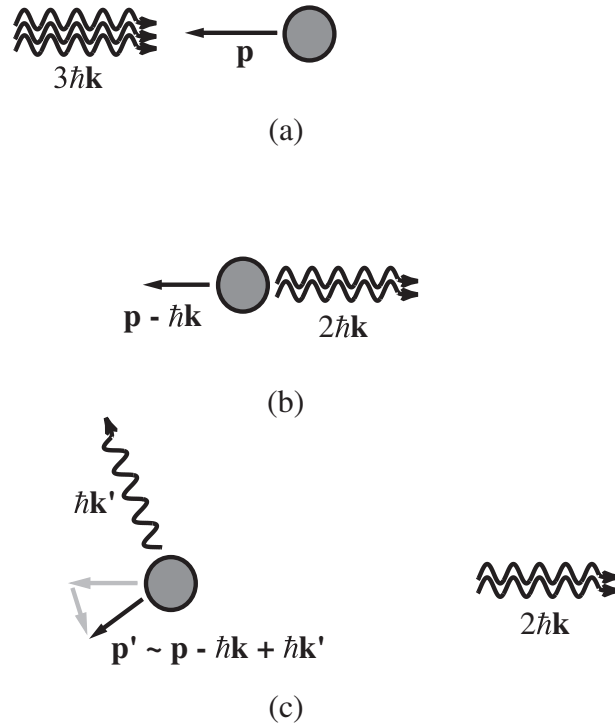


Figure 2.1: (a),(b) An atom of original momentum  $\mathbf{p}$  receives a momentum kick of momentum  $\hbar\mathbf{k}$  upon absorption of a photon. (c) Spontaneous photon emission imparts a second momentum kick of  $\hbar\mathbf{k}'$  to the atom. (Stimulated emission would induce photon emission into the laser field mode.)

$1/p_e$  and the natural lifetime  $\tau_n$  of the atom in the excited state:

$$\tau_{scat} = \frac{\tau_n}{p_e}. \quad (2.1)$$

The natural lifetime is the inverse of the Lorentzian linewidth,  $\Gamma$ , of the atomic transition:  $\Gamma = 1/\tau_n$ . The scattering rate  $1/\tau_{scat}$  is thus  $p_e\Gamma$ . In order to determine the scattering force, we must determine  $p_e$  for the given field strength.

The strength of the field is determined by the intensity,  $I$ , and the detuning,  $\Delta = \omega - \omega_0$ , of the light field from the atomic resonance. In very strong fields,  $p_e = 1/2$ , and in the absence of all fields,  $p_e = 0$ . *Saturation* is defined as the condition where  $p_e = 1/4$ . If the driving field is tuned to resonance, the saturation condition is reached at an intensity of

$$I_{sat} = \frac{\hbar\omega\Gamma k^2}{12\pi}. \quad (2.2)$$

We can write  $p_e$  as

$$p_e = \frac{S}{2(1+S)}, \quad (2.3)$$

where the unitless *saturation parameter*  $S$  is defined as

$$S = \frac{I/I_{sat}}{1 + 4\left(\frac{\Delta}{\Gamma}\right)^2}, \quad (2.4)$$

so that  $S \ll 1$  for very weak fields (well below saturation),  $S = 1$  for a saturated transition, and  $S \gg 1$  for a very strong driving field well above saturation. Note that the definition of  $S$  incorporates both detuning and intensity, since the intensity needed to saturate the atom with  $\Delta \neq 0$  is greater than  $I_{sat}$ . For  $\Delta = 0$ ,  $S$  is simply  $I/I_{sat}$ . We can rewrite  $p_e$  as

$$p_e = \frac{1}{2} \left[ \frac{I/I_{sat}}{1 + I/I_{sat} + 4(\Delta/\Gamma)^2} \right]. \quad (2.5)$$

We are now able to determine the scattering force due atom absorption of photons of



momentum  $\hbar\mathbf{k}$ :

$$\mathbf{f}_{scat} = \frac{\hbar\mathbf{k}}{\tau_{scat}} = \frac{\hbar\mathbf{k}\Gamma}{2} \left[ \frac{I/I_{sat}}{1 + I/I_{sat} + 4(\Delta/\Gamma)^2} \right], \quad (2.6)$$

where appropriate substitutions have been made in obtaining this last expression.

### 2.2.2 Doppler cooling

Doppler cooling utilizes the scattering force to remove kinetic energy from atoms via momentum transfer with the laser field. For full three-dimensional cooling, the field consists of three orthogonal pairs of counter-propagating laser beams [39] so that light is always propagating against the motion of an atom with any given velocity direction. Of course, light is also propagating *with* the atom in this configuration. In order to induce an atom to preferentially absorb light from the *opposing* beams, the lasers are tuned to the red of resonance ( $\Delta < 0$ ). In the rest frame of an atom moving with a velocity  $\mathbf{v}$ , the light is then Doppler shifted such that the *effective* detuning of a light field with wavevector  $\mathbf{k}$  becomes  $(\omega - \omega_0) - \mathbf{k} \cdot \mathbf{v}$ . This velocity dependence enters into the scattering force equation, resulting in preferential absorption from the laser beams propagating against the atom motion (where  $\mathbf{k} \cdot \mathbf{v} < 0$ , and thus  $\Delta$  becomes closer to zero). The scattering forces oppose the motion of each atom, moving in any direction, resulting in lower atomic velocities and hence lower temperatures.

This cooling method produces a cloud of cold atoms, called *optical molasses*, first observed by Chu *et al.* [3]. Atoms are not trapped, due to the absence of a restoring force that would localize them at a single point in space. However, Doppler cooling is effective at cooling atoms from room temperatures (or higher) to  $\mu\text{K}$  temperatures. Nevertheless, Doppler cooling has a limit: the balanced damping forces of the optical molasses laser beams cause each atom to undergo a random walk through the beam intersection region as the atom scatters photons from the beams, resulting in a lower temperature limit of  $T_D \sim \hbar\Gamma/2k_B$ .

### 2.2.3 Beyond the two-level atom model

Laser cooling can, however, produce temperatures well below the Doppler temperature limit, as the NIST laser cooling group originally demonstrated [4]. The lower temperatures were explained using models that went beyond the two-level atom theory [5, 6]. The cooling mechanism works via spatially varying polarization gradients obtained with either counter-propagating linearly polarized beams (*lin* $\perp$ *lin* configuration) or circularly polarized beams (the  $\sigma^+ - \sigma^-$  configuration). The details of the cooling mechanisms will not be given here. For our experiments, the  $\sigma^+ - \sigma^-$  configuration was used. With two oppositely polarized and counter-propagating circularly polarized laser beams, the total electric field consists of linearly polarized light with a direction that rotates in space. Although polarization gradient cooling is ineffective for Li, it is significant for Rb, and allowed us to reach optical molasses temperatures an order of magnitude below the Doppler limit.

### 2.2.4 Optical pumping

Atoms can be driven to a particular energy state by optical pumping techniques. In an excitation process, an atom may be excited and then decay to a state other than the initial ground state. For example, a Rb atom in the  $5S_{1/2}, F = 2$  ground state<sup>1</sup> may undergo a transition to an excited state and then decay to the  $5S_{1/2}, F = 1$  ground state, where it will no longer scatter light of the same frequency. Because of a finite probability for this transition, all of the atoms that begin in the  $F = 2$  level will eventually end up in the  $F = 1$  level after repeated scattering events. This process is an example of optical pumping into a *dark state*, in which an atom has a negligible interaction with the light field. Although this process is frequently utilized, it can destroy the efficiency of laser cooling by limiting the number of scattering events unless a second *repumping* laser beam is added. This beam is tuned to a transition between the otherwise dark ground state and an excited state which can

---

<sup>1</sup>The hyperfine level  $F$  represents the total angular momentum of the atom, composed of the electron spin and orbital angular momentum and the nuclear spin. An external magnetic field breaks these levels into the hyperfine sublevels, designated as  $m_F$ . In this thesis,  $F$  represents the ground-state hyperfine level, and  $F'$  the excited-state level.

decay to either of the two ground states. The atom then continues to scatter photons regardless of the ground state.

Atoms may instead be optically pumped into a *bright state* in which the atoms continue to scatter light from an optical pumping beam. We use this method after laser cooling Rb atoms in order to prepare the atoms in a state in which they can be magnetically trapped. A circularly polarized light beam propagates parallel to a bias magnetic field. As atom scatters a photon, the angular momentum of the photon is transferred to the atom. If the atom subsequently spontaneously emits a photon, the angular momentum of the atom may increase, decrease, or remain unchanged. For a transition between the ground energy level and an excited state with  $F' = F + 1$ , repeated photon scattering can push the atom to a *swing* or *stretch* state, where the total angular momenta of the nucleus and electron are aligned ( $m_F = \pm F$ ). The atom can then only undergo transitions between the ground state with  $m_F = \pm F$  and the excited state with  $m_{F'} = \pm F'$ .

### 2.2.5 Lithium and Rubidium

Real atoms, of course, have many more than two energy levels. Nevertheless, it is usually sufficient to just consider a small number of levels when determining the effects of an external field on an atom. When cooling alkali atoms, a ground state manifold ( $nS_{1/2}$ , where  $n$  is the principle quantum number) and an excited state manifold  $[(n + 1)P_{3/2}]$  are typically the levels considered. The fine-structure energy levels of the atom are further split into hyperfine levels due to the coupling of the nuclear magnetic moment with the electron magnetic moment. Characteristics of Li and Rb, and the hyperfine structure of the principal optical transitions, are given in Appendix A.

## 2.3 Magneto-optic traps

In order to localize cold atoms, a restoring force is needed in addition to the damping force of the laser beams. The magneto-optic trap (MOT) [7] provides such a restoring

force, and is useful in obtaining large numbers ( $\sim 10^8$  to  $10^{10}$ ) of ultra-cold atoms. A MOT is created by adding a magnetic field gradient to the laser cooling beams, with the minimum of the magnetic field at the intersection of the beams. Due to Zeeman shifts, the field gradient breaks the degeneracy of the hyperfine magnetic sublevels and imposes a shift in the energy levels proportional to the distance from the center of the field. The laser beams are polarized such that an atom in any region preferentially scatters photons from the laser beam that would provide momentum kicks towards the magnetic field minimum. Since the magnetic hyperfine sublevels will scatter photons at different rates (due to different Zeeman shifted transition frequencies), the laser polarizations are adjusted such that the atom makes transitions into the state with a resonance frequency nearest the laser frequency. Then, the scattering is preferential for the transition with the higher scattering rate.

Experimentally, this can be done with counter-propagating pairs of  $\sigma^+$  and  $\sigma^-$  polarized laser beams along each of the beam axes. The magnetic field gradient is created by two current-carrying coils with the same symmetry axis but with current traveling in opposite directions (anti-Helmholtz configuration). The symmetry axis is aligned along one of the laser beam axes. Figure 2.2 shows a typical configuration of beams and coils. The beams can have polarizations and spatial configurations other than described here, but these other methods will not be discussed.

Atoms can be loaded into a MOT using various techniques. The simplest method is to create a MOT in a vapor cell [40], in which a background thermal vapor of atoms is present. The coldest atoms in the vapor can be further cooled by the scattering force and trapped in the MOT. The remaining atoms in the vapor contribute to scattering processes with the cold, trapped atoms, and thereby limit the number of atoms that can be captured. A MOT can alternatively be loaded from an atomic beam [41]. This is most often done by slowing the longitudinal velocity of the atoms in the beam with a counter-propagating laser through the scattering force. The MOT is situated such that the pre-cooled atoms can then be captured by the laser cooling beams and loaded into the trap.

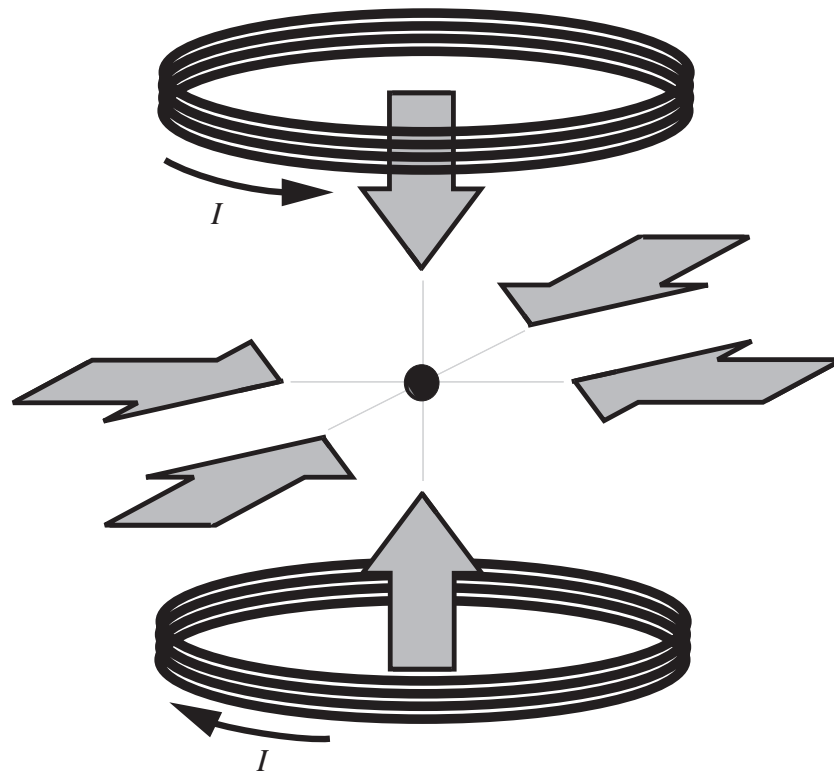


Figure 2.2: A typical MOT experimental setup. The dark ovals represent the magnetic field coils. The gray arrows represent 3 orthogonal pairs of laser beams, and the dark circle represents the trapped atoms at the laser beam intersection region. The electric current direction in the field coils is labeled.

## 2.4 Optical traps

The light forces that have been considered up to this point are *dissipative*. The atoms interact with a light field by absorption of a photon in a given mode and subsequent spontaneous emission of a photon into a continuum of vacuum-field modes. The atoms dissipate energy by irreversible coupling to modes other than the mode(s) of the incident light field(s). Although it is the dissipative scattering force which allows momentum transfer between atoms and photons to reduce the atomic kinetic energy, these forces alone can not localize atoms. As discussed above, the MOT allows atom trapping with the addition of a magnetic field to a dissipative light field. However, dissipative light forces limit reductions in atom momenta to near a photon recoil since the forces on the atom at the single-photon level are not balanced.

Alternatively, a *conservative* light field can localize atoms through light-induced internal atomic energy level shifts [42]. A single traveling wave laser beam, a standing wave, or other beam configurations can trap cold atoms. For this to occur, dissipative scattering forces must be small compared to the conservative *dipole forces*, which may be viewed as photon exchange between an atom and the laser field modes for both photon absorption and emission. As a result, light forces may be balanced enough to permit atoms to be cooled to temperatures below that of a single-photon recoil.

### 2.4.1 Dipole forces

An electric field  $\mathbf{E} = E_0 \cos(\omega t)$ , oscillating at a frequency  $\omega$  near the atomic resonance  $\omega_0$  will perturb the internal atomic energy levels. In the limit  $\Delta \gg \Gamma$ , where the ac Stark shift is  $\hbar\Omega_{AC}$ , with  $\Omega_{AC} \approx \Omega_r^2/\Delta$ , the effective dipolar potential for the atoms is  $U_{dip} \approx |\mathbf{d} \cdot \mathbf{E}|^2/\hbar\Delta$ , where  $\mathbf{d}$  is the electric dipole moment of the atom<sup>2</sup>. If the driving field is due to a laser beam with intensity  $I$  and detuning  $\Delta$ , the potential can be rewritten as

$$U_{dip} \approx \frac{\hbar\Gamma}{8} \frac{I/I_{sat}}{\Delta/\Gamma}. \quad (2.7)$$

For red detunings ( $\Delta < 0$ ), this potential is attractive, whereas blue detunings

---

<sup>2</sup> $\Omega_r$  is the Rabi frequency, defined by  $\Omega_r = \mathbf{d} \cdot \mathbf{E}/\hbar$ .

( $\Delta > 0$ ) repel atoms from high-intensity regions. In a red-detuned field, the dipole moment of the atom oscillates in phase with the light field, and the instantaneous Stark shift  $E_{Stark} = -\mathbf{d} \cdot \mathbf{E}$  is negative. At a node of the time-varying field, the atom's energy levels are unperturbed. At an anti-node, they are shifted to lower effective energy levels. On average, then, in a red-detuned beam, the potential energy of an atom is decreased. The opposite is true for blue-detuned beams, where  $\mathbf{d} \cdot \mathbf{E} < 0$  and the light increases the internal potential energy of the atom.

A red-detuned traveling-wave laser beam pushes atoms towards the center of the focus of the beam where intensity is highest and the potential energy is minimized. The force on the atoms is determined by the spatial gradient of the potential, which is determined by the spatial variation of the beam intensity. Thus, the force transverse to the beam is governed by the local beam diameter, and the longitudinal force is determined by the rate of beam divergence or convergence.

### 2.4.2 Optical lattices

Interference between multiple laser beams can create a trap with a spatially varying periodic potential, called an optical lattice [15, 16, 28]. A simple retro-reflected red-detuned laser beam can trap atoms in the standing wave anti-nodes. As in the traveling-wave case, the transverse force is determined by the beam waist. The longitudinal force, however, is determined by the periodicity of the potential — in this case, the wavelength of the trapping light. This is an example of a one-dimensional optical lattice.

Periodic potentials in multiple dimensions are created by the interference of at least 3 beams (for a 2-dimensional lattice) or 4 beams (for a 3-dimensional lattice). The periodicities in the various spatial directions are determined by the spatial configurations, detunings, and polarizations of the beams. A trap can be created by regions of red-detuned light in a 1-, 2-, or 3-dimensional lattice. To create a trap with blue-detuned light, the potential wells are formed by pockets of relative darkness surrounded by light.

The lifetime of atoms trapped in an optical lattice can be limited by photon

scattering, which adds energy to the system, although it can be limited by other processes as well. With far-off-resonant light, the scattering rate scales as  $I/\Delta^2$ , while the potential depth scales as  $|I/\Delta|$ . In order to increase lifetimes of traps without sacrificing trap depth, the intensity of the beams must be increased in proportion to the detuning increase.

## 2.5 Magnetic traps

Atoms can be trapped in a magnetic field gradient due to interactions of the field with the Zeeman shifted energies of the internal atomic hyperfine sublevels. As in a MOT, a magnetic trap relies on a minimum in the magnitude of the magnetic field. The internal states of the atom will increase or decrease in energy as the atom moves away from the magnetic field minimum. For the field strengths used in our experiments, the Zeeman energy shift of a state is given by  $E_Z \cong \mu|\mathbf{B}|$ , where  $|\mathbf{B}|$  is the magnetic field strength and  $\mu = gm_F\mu_B$  is the magnetic dipole moment of the electron (proportional to the electron spin). Here,  $g$  is the gyromagnetic (Landé) factor associated with the hyperfine level,  $m_F$  is the hyperfine sublevel, and  $\mu_B$  is the Bohr magneton ( $\mu_B = e\hbar/2m_e$ ).

Atomic potential energy increases as an atom moves away from a field minimum if  $gm_F > 0$ , and energy will decrease as an atom moves away if it is in an  $m_F$  state of the opposite sign. For example, in the  $^{87}\text{Rb } 5S_{1/2}, F = 2$  level, with  $g = 1/2$ , an atom in the  $m_F = 2$  state (with the spin polarization axis determined by the magnetic field) will experience increasing internal energy as it moves away from the field minimum. The tendency to favor minimum energy can therefore trap an atom that is in this quantum state (a *weak-field seeking* state). The  $m_F = 1$  state can also be trapped, but with a force that is half as strong. The negative  $m_F$  states of the  $F = 2$  ground level, however, will be expelled from the field minimum. The  $m_F = 0$  state is unaffected by the magnetic field in this limit (where higher order corrections to the Zeeman shift are negligible).



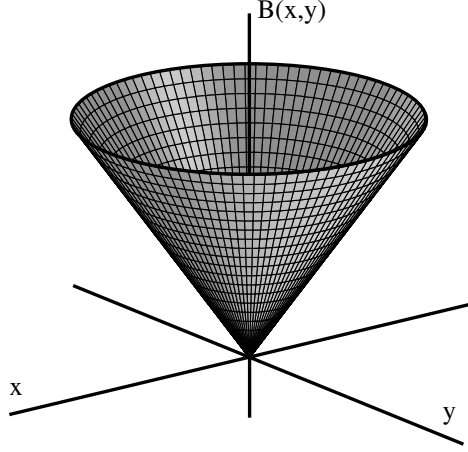


Figure 2.3: A representation of the spherical-quadrupole trap field along two orthogonal directions. The field increases linearly away from the  $B = 0$  field minimum.

### 2.5.1 Spherical-quadrupole trap

Several types of magnetic traps have been developed, with different field gradient shapes near the potential minimum. The simplest trapping configuration is the spherical-quadrupole trap [43]. The field gradient is created by two current-carrying coils aligned in an anti-Helmholtz configuration, identical to the coil configuration of a standard MOT. The minimum of the field has a magnetic field value of zero, and the gradient is linear with distance. The strength of the trapping potential increases linearly with current in the coils (Fig. 2.3).

Although this trap is simple to construct, it has a flaw which inhibits (without additional modifications) the low temperatures needed for reaching Bose-Einstein condensation: the coldest atoms in the trap have a high probability of escape from the trap. When an atom passes through a region near the center of the trap (where  $B = 0$ ), the field gradient changes too quickly for the atom to maintain the proper polarization in the spatially varying magnetic field. The atom then has a high probability of changing states (Majorana spin flips), with the result of possible ejection from the trap [44]. At other regions in the trap, the field direction changes gradually enough that the magnetic moment of the atom can follow the changing field direction

and remain polarized. As an atom becomes colder, it spends more time close to the center of the trap, so loss due to spin-flips occurs primarily for the coldest atoms.

To overcome the Majorana spin flips, other magnetic trap configurations were developed and used in cooling atoms and achieving BEC. These traps have the general feature that field gradients are *not* linear in all dimensions, and that the minimum of the magnetic field is not zero. These traps include the optical plug trap developed at MIT [24], where the “hole” in the spherical-quadrupole trap is plugged by a blue-detuned light beam which repels atoms from the center region, the permanent-magnet trap used at Rice [45], Ioffe-type traps used in many other BEC experiments [46], and the time-averaged orbiting potential (TOP) trap [47], developed at JILA and currently in use in other experiments. The TOP trap was used in the first demonstration of BEC, and was the type of trap used in our BEC experiments.

## 2.5.2 Time-averaged orbiting potential trap

The TOP trap is created by adding a rotating bias magnetic field of constant magnitude to the linear gradients of a spherical-quadrupole trap. The bias field shifts the position of the center of the linear-gradient magnetic trap, and the instantaneous gradient remains linear. However, since the bias field direction rotates, the instantaneous field minimum also rotates about a point in space [Fig. 2.4(a)].

If the bias field spins fast enough, the motion of the cold atoms can not track the position of the rotating field zero. The atoms will instead be localized to the region in space defined by the center of the original spherical-quadrupole gradient, with only the spins of the atoms tracking the motion of the bias field. In the rotation frequency ranges used, typically a few kHz, the motion of the atoms in the trap can be described with a time-average of the superimposed fields. This time-averaged orbiting potential trap is harmonic to lowest orders at the center of the trap, and the minimum value of the magnetic field is given by the strength of the rotating bias field [Fig. 2.4(b)].

If the rotating bias field is applied in the  $(x, y)$  plane, and the  $z$  axis defines the strong axis of the linear field gradient, the instantaneous TOP trap potential is given

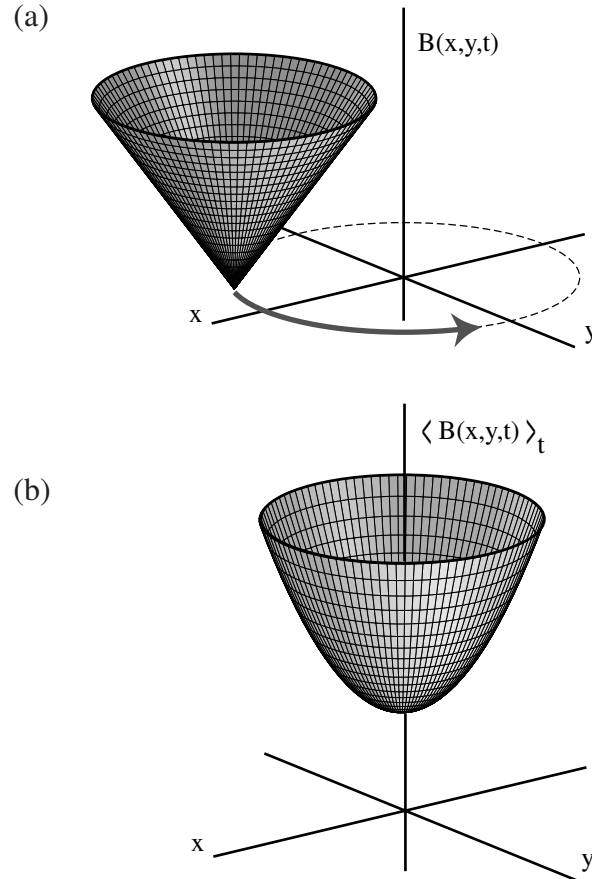


Figure 2.4: A representation of the magnetic field of the TOP trap. (a) The instantaneous magnetic field is a linear gradient rotating in a plane. (b) The time-averaged magnetic field is harmonic with a non-zero magnetic field minimum.

in Cartesian coordinates by

$$U(x, y, z, t) = \mu|[xB'_q + B_{rot} \cos(\omega_b t)]\hat{\mathbf{x}} + [yB'_q + B_{rot} \sin(\omega_b t)]\hat{\mathbf{y}} - 2zB'_q\hat{\mathbf{z}}|. \quad (2.8)$$

Here,  $B'_q$  is the radial linear field gradient (in the  $(x, y)$  plane),  $B_{rot}$  is the strength of the rotating bias field, and  $\omega_b$  is the angular rotation frequency of the bias field. To first order, a time average of the energy of an atom in the TOP trap potential is given in cylindrical coordinates by

$$U_T \simeq \mu B_{rot} + \frac{\mu B_q'^2}{4B_{rot}}(r^2 + 8z^2). \quad (2.9)$$

In these equations, the effect of gravity is neglected. (For weak potentials and weak bias fields, the effect of gravity can be significant.)

Majorana spin-flip transitions are not eliminated in the TOP trap. However, instead of occurring at the center of the trap where the cold atoms reside, they occur in a torus at the outer limits of the trap (in the radial plane) where the zero point of the spherical-quadrupole field rotates. This toroidal region at the edge of the trap has been called the “circle of death” since it limits the depth (and size) of the trap. The radial position of the field zero is given by  $R_0 = B_{rot}/B'_q$ , and the trap depth is given by  $\mu B_{rot}/4$ . Instead of removing the cold atoms from the trap, the most energetic atoms will be removed from the system.

## 2.6 Evaporative cooling

Reaching the BEC threshold with laser-cooled atoms from a MOT requires a substantial increase in the phase-space density of the trapped atoms. Phase-space incorporates the spatial coordinates and momentum-space coordinates of a particle. Phase-space can be divided into unit cells of volume  $\hbar^3$ , and the phase-space density,  $\rho$ , is defined as the number of particles per phase-space unit cell. Thus  $\rho$  is a six-dimensional measure of the spatial density and the temperature of the system, and

is defined as

$$\rho = n\lambda_{th}^3, \quad (2.10)$$

where

$$\lambda_{th} = \sqrt{2\pi\hbar^2/mk_B T} \quad (2.11)$$

is the mean thermal de Broglie wavelength of a particle in a system at temperature  $T$ . In the above expressions,  $n$  is the average spatial density of the particles,  $m$  is the particle mass, and  $k_B$  is the Boltzmann constant. Einstein first derived the degeneracy condition [48], which occurs for  $\rho = 2.612$ , where more than one particle occupies a phase-space unit cell. This condition, when  $n \sim \lambda_{th}^{-3}$ , implies that the thermal wavelengths of the particles are comparable to the spacing between particles.

Typically,  $\rho \sim 10^{-6}$  for atoms trapped in a MOT, an astounding increase from  $\rho \sim 10^{-19}$  for a thermal atomic beam or room temperature vapor. In order to reach atomic degeneracy and BEC, however,  $\rho \sim 1$  must be achieved. Adiabatic cooling methods have been shown to be successful in cooling trapped atoms [49, 50]. However, adiabatic cooling processes conserve phase-space density. A different technique was needed in order to realize the necessary gain in  $\rho$  of a factor of  $\sim 10^6$ .

All successful vapor-phase Bose-Einstein condensation experiments to date have utilized forced evaporative cooling in achieving BEC. With evaporative cooling, the hottest particles in a system are removed, as illustrated in Fig. 2.5. The remaining particles reach a new thermal equilibrium through elastic collisions. The new distribution has a lower mean temperature than the original distribution. Although some particles are lost in the process, the remaining particles are on average colder. This process occurs naturally in common events such as cooling of a hot beverage, or an evaporating puddle of water on hot pavement. In these examples, the most energetic particles leave the system in the vapor phase, and the remaining liquid is left colder than before. For a cup of coffee, this process continues until the liquid is in thermal equilibrium with the environment. For the puddle of water, heat is continually entering the system from the environment. As the water evaporates (the hottest particles leave the puddle as a vapor), the puddle cools. However, external heat added to the system from the hot pavement increases the temperature, and hot water molecules

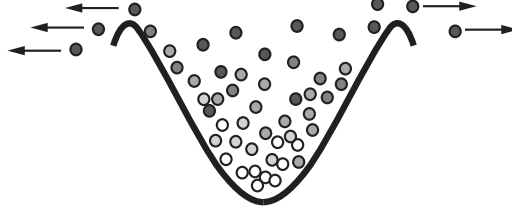


Figure 2.5: With evaporative cooling, the most energetic particles leave the system, and the remaining particles rethermalize to an energy distribution with a colder mean temperature.

continue to escape from the system as vapor. This may occur until the puddle of water has disappeared.

Forced evaporative cooling relies on identical physical processes, but the maximum allowed temperature in the thermal distribution, the energy at which the distribution is truncated, is slowly decreased. A portion of the trapped particles are removed in order for the remainder to become colder. If heat is added to the system in the process, as in the puddle example above, all particles may eventually be lost before degeneracy is achieved.

In a trap where an atom's distance from the trap center is proportional to its temperature, a colder sample of atoms may result in a denser population. With the average density proportional to  $N/r^3$ , where  $r$  is the trap radius and  $N$  is the number of trapped particles, and with temperature proportional to  $r^2$ ,  $\rho \propto N/T^3$ . Thus  $\rho$  may increase in the evaporative cooling process even though atom number decreases, provided that the temperature is lowered at a rate fast enough compared to the number lost. The rate of thermalization, which governs the speed at which forced evaporation can be achieved, increases with density as the rate of elastic collisions increases. So, once evaporative cooling becomes efficient for a given sample of atoms, it can rapidly increase in efficiency as the temperatures are forced even lower (runaway evaporative cooling). Under these conditions, BEC can be reached.

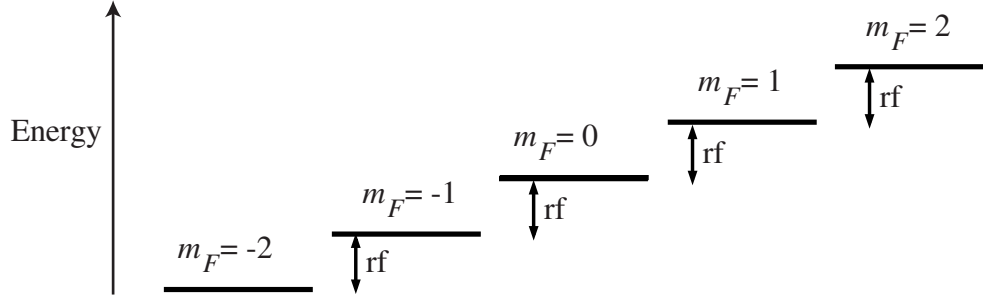


Figure 2.6: An rf field, with frequency tuned to the resonance frequency between two adjacent hyperfine sublevels, drives transitions from the trapped  $m_F = 2$  and  $m_F = 1$  states to the remaining untrapped states for  $^{87}\text{Rb}$ ,  $F = 2$  atoms.

The most common technique for implementing evaporative cooling in a magnetic trap is through the use of a radio-frequency (rf) magnetic field. The field induces a transition between hyperfine sublevels so that an atom in a trapped state makes a transition to an untrapped state, as illustrated in Fig. 2.6, and is lost from the trap. Because the energy difference between untrapped and trapped states increases with distance from the trap center, the frequency at which a hot atom (with trajectories that take it far from the trap center) makes a transition will be well above the rf resonance frequency of the colder atoms. The hot atoms are selectively ejected from the trap, the remaining atoms rethermalize, and a subsequent rf field can be applied at a slightly lower energy. Repeated rf cuts of this nature will produce a cold and dense trap [36]. In practice, the rf cuts are actually ramps that start at high frequencies and sweep to lower frequencies.

## 2.7 Bose-Einstein condensation

Bose-Einstein condensation is a macroscopic occupation of a single quantum state. The theory for condensation in an ideal gas was formulated by A. Einstein in 1925 [48], building on statistical analysis by S. Bose of the black-body radiation spectrum [51]. Einstein's theory and others that followed [52] discussed the relationship between the

temperature of a system and the number of integral-spin particles (bosons) allowed to occupy the excited-state energy levels of the system. Because temperature,  $T$ , is a measure of the distribution of particles among the excited states of the system, a given temperature corresponds to a maximum number of atoms that may occupy the excited energy levels. In a system with this maximum number, a decrease in temperature can only be accomplished by allowing some of the particles to occupy the ground state of the system, which does not contribute to the temperature of the system. In other words, for a fixed number of trapped particles, there is a critical temperature below which particles will fall into the ground state of the system. This temperature is called the Bose-Einstein condensation temperature,  $T_C$ , and occurs at  $\rho = 2.612$  for an ideal non-interacting gas.

The macroscopic occupation of the ground state is a quantum mechanical feature unique to bosons, since the Pauli exclusion principle restricts fermions to separate quantum states. The fraction of atoms in the Bose-Einstein energy distribution that occupies the ground state is called the Bose-Einstein condensate, with the remaining distribution usually called the *normal fraction*. The ratio of the number of atoms in the BEC,  $N_C$ , to the total number of particles in the system,  $N$ , is called the *condensate fraction*, which increases as the temperature of the system is lowered even further below  $T_C$ . For a trapped ideal gas below  $T_C$ , the condensate fraction follows the form

$$\frac{N_C}{N} = 1 - \left( \frac{T}{T_C} \right)^3. \quad (2.12)$$

Above  $T_C$ , the condensate fraction is zero. The value of  $T_C$  is given by

$$T_C \simeq \frac{\hbar \bar{\omega}}{k_B} \left( \frac{N}{1.2} \right)^{1/3}, \quad (2.13)$$

where  $\bar{\omega}$  is the geometrical mean of the trap oscillation frequencies.

However, atoms are not ideal, and may interact. Strong interactions between atoms occur when the density is very high, as in a liquid. This case is far from the theoretical limits of an ideal gas, and thus difficulties arise in predicting the condensation properties of superfluid He. Weaker interactions are found in dilute atomic vapors, with atomic densities many orders of magnitude below those of liquids. Thus



the goal of reaching BEC in a dilute atomic gas was heavily pursued by experimental physicists and highly anticipated by theoretical physicists in order to more readily facilitate comparisons with theory. In the ongoing discussion of BEC in this thesis, we will consider atomic-gas condensates unless otherwise stated.

Interactions can either be repulsive or attractive, depending upon the quantum states of the interacting atoms and the atomic species. The interactions are characterized by the s-wave scattering length,  $a$ , of the atomic interaction. For  $a < 0$ , interactions are attractive, for  $a > 0$ , interactions are repulsive, and for  $a = 0$ , the system is non-interacting.

Interactions between atoms in a condensate will shift the total energy of the occupied ground state. These interactions are typically quantified using a mean-field approximation in which the total energy (chemical potential) of the atoms consists of the energy of the single-particle state plus a pseudo-potential that accounts for the interaction energy [53]. For atoms with repulsive interactions such as  $^{87}\text{Rb}$ , the atomic energy is raised an amount

$$U_{MF} = 4\pi\hbar^2 an/m, \quad (2.14)$$

linearly dependent on the local density  $n$  of atoms (of mass  $m$ ) in the trap.

Most atomic species that have been condensed exhibit repulsive interactions in the quantum states used in the experiments. Lithium, however, is the only gas with attractive interactions that has been condensed so far [23]. With attractive interactions, the mean-field energy shift is negative, lowering the total energy of the condensate in proportion to the BEC density. BEC in a gas with  $a < 0$  was initially thought to be unobtainable, with atoms forming molecular states due to attractive interactions as the density increased and the total energy decreased. However, BEC was achieved with  $^7\text{Li}$ , and refined theories now predict that a finite number of atoms can exist in the condensate [54] before a collapse occurs. The results of the Li experiments at Rice agree with these predictions [55].

In the remainder of this thesis, we will consider atoms with repulsive interactions. Usually, a system above the condensation threshold is at a low enough density or a

high enough temperature that the kinetic energy dominates the mean-field energy, which can then be ignored. In the case of a BEC, this is not necessarily a good approximation, and mean-field effects must be considered. If mean-field energy is much greater than kinetic energy, the system is in the so-called Thomas-Fermi limit. In this limit, where most BEC measurements have been made, good approximations to the condensate characteristics can be obtained, and experiments have verified the predicted effects due to the mean-field interactions. The interactions tend to decrease the density of the BEC by increasing the BEC size, shift the condensation temperature  $T_C$ , and modify the dependence of the condensate fraction with temperature. Further elaboration of the mean-field interactions and effects will be given later in this thesis.

Condensate characteristics are typically measured by imaging the condensate onto a CCD camera, and digitally recording the image. The images are taken with a probe beam propagating into the chamber, onto the BEC, and then through imaging optics which image the condensate onto the camera. The images can be taken in a variety of different ways, discussed in Chapter 6, and allow measurements of condensate characteristics.

## 2.8 Consolidation of techniques

An overview of the entire BEC production sequence that we used, largely following the procedure in Ref. [22], can now be given to demonstrate the consolidation of the techniques discussed in this chapter. In our experiment, atoms in a vapor cell were first laser cooled and loaded into a magneto-optic trap. These atoms were then prepared in a weak-field seeking state by optical pumping, and trapped in a TOP trap. We evaporatively cooled the atoms below the BEC critical temperature, and used imaging methods to measure BEC characteristics. This procedure is described in detail in Chapter 6. We then loaded the condensed atoms into a one-dimensional optical lattice, and imaged the atoms to study the effect of the lattice on the atoms. This experiment is described in Chapter 7.

# Chapter 3

## Enhanced loading of a $^7\text{Li}$ magneto-optic trap

### 3.1 Motivation

Many atomic physics experiments rely on the capture of large numbers of atoms from either a thermal source or a vapor. Of these experiments, the ones which depend upon laser-cooled and trapped atomic sources also rely on efficient loading of large numbers of atoms into the trap. Bose-Einstein condensation, for example, is more readily achieved by initiating the evaporative cooling process with higher numbers of atoms, due to the lossy but extremely effective process of evaporative cooling. Other experiments and techniques depend upon large numbers of atoms in order to improve resolution in measurements and decrease the times necessary to perform measurements. Laser-cooled atomic time standards [12, 13], and precision atom interferometry experiments [56, 57] fall into this class. The techniques described in this chapter are primarily relevant to the capture and confinement of large numbers of atoms in a magneto-optic trap (MOT).

Currently employed methods for atom capture fall into two classes. In the first class, a thermal atomic beam is slowed by a counter-propagating laser beam [41] via the spontaneous light scattering force, Eq. 2.6. In order to ensure that the laser

light remains resonant with the Doppler-shifted atomic transition as the atom decelerates, either the frequency of the light is altered (with a frequency chirp [58], or a “white-light” laser source [59] having a large frequency modulation that broadens the spectrum), or an external magnetic [60] or electric [61] field gradient is applied to shift the atomic transition into resonance with the light as the atoms propagate. In the second class, the low-velocity tail of the Maxwell-Boltzmann distribution is directly captured from a thermal atomic beam or a vapor [40, 62]. Other techniques for loading atoms into a MOT rely on a pre-cooling MOT and subsequent efficient transfer of the cold atoms into a trap in another region of the vacuum chamber. While this technique is certainly very useful, the initial stage of the experiment falls into the second category described above, where atoms are loaded into the initial MOT from a vapor.

In the approach described here for  $^7\text{Li}$ , atoms in the low-velocity tail of the Maxwell-Boltzmann distribution were captured and loaded directly from an atomic beam into a MOT. We achieved high loading rates by (i) minimizing the distance between the atomic oven nozzle and the trapping region and (ii) broadening the frequency spectrum of the trapping light.

## 3.2 Direct loading from an atomic beam

High loading rates of atoms into magneto-optic traps may be achieved by locating the nozzle of an atomic beam oven close to the trapping region, giving results comparable to those obtained by other currently used methods [63]. Although traditional methods such as Zeeman-slowing techniques efficiently reduce the speed of atoms along the propagation axis of the slowing light, they do so at the expense of increasing the divergence (transverse spreading) of the atomic beam. Placing the nozzle close to the trap, on the other hand, reduces losses due to transverse spreading while diminishing the potential effectiveness of longitudinal slowing. An analysis similar to that for a vapor-cell loaded trap [40] predicts a loading rate  $R \approx C v_c^4 d^2 / l^2$ . Here,  $C$  is a constant,  $v_c$  is the maximum atomic velocity which can be captured by the trap,  $d$  is the diameter of the trapping beams, and  $l$  is the distance from the oven nozzle to the

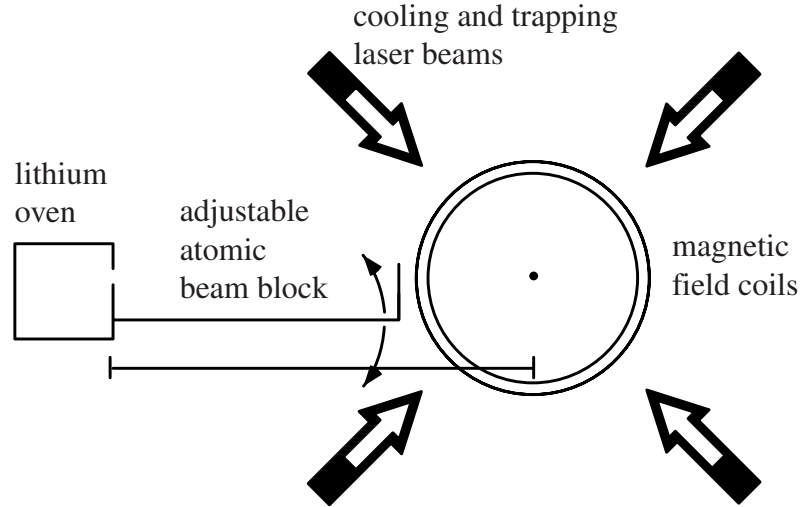


Figure 3.1: An illustration of the apparatus used to cool and trap  $^7\text{Li}$ . Atoms are loaded directly from the oven into the MOT without a precooling (slowing) stage. The cooling and trapping laser beams, shown as arrows, are taken to lie along the positive and negative  $(1,0,0)$ ,  $(0,1,0)$ , and  $(0,0,1)$  axes, and the oven is located along the  $(1,1,1)$  axis.

trap center. This expression is strictly valid when  $d \ll l$  and  $v_c \ll \sqrt{k_B T/m}$ , where  $T$  is the atomic beam temperature, and  $m$  is the atomic mass. The geometric factor of  $d^2/l^2$  accounts for the spatial localization of the atomic source. As  $l \rightarrow d$ , the loading rate becomes comparable with the optimal rates obtained using field-gradient slowing techniques.

### 3.2.1 Experimental considerations

The geometry of our experiment is shown in Fig. 3.1. The oven nozzle was set back  $l \sim 20$  cm from the trap center and  $d$  was  $\sim 1$  cm. An atomic-beam shield, shown in Fig. 3.1, was located  $\sim 6$  cm from the center of the trapping region between the oven nozzle and the trap center. The shield was mounted on a continuously adjustable stage, which allowed it to be translated from a position that completely blocked the atomic beam to one that fully transmitted the beam. This permitted the shield to

be adjusted to a mid-range position where it blocked fast atoms from direct collisions with trapped atoms (which typically accumulated in a 200 to 500- $\mu\text{m}$  diameter ball near the center of the trapping beams), while sacrificing a factor of  $\sim 2$  in loading rate.

Two important differences between the above geometry and a vapor cell-loaded trap [40] can be noted. First, the vapor cell geometry requires the entire vacuum apparatus to be heated to a temperature high enough to yield a partial vapor pressure higher than the background gas pressure. This is awkward for elements like Li, for example, where this temperature is  $\sim 200$  to  $300^\circ\text{C}$ . Second, the localization of the atomic source in the beam geometry permits the trap to be shielded from direct collisional impact from high-velocity atoms originating in the source.

### 3.2.2 Trap capture velocity

The trap capture velocity plays an important role in determining the net loading efficiency. We estimate the capture velocity with the following trap model [64], which we describe in order to provide a means to assess the *relative* gains achieved with spectrally broadened trapping lasers. In the model, an atom of initial velocity  $v$  will be captured if its velocity is reduced to  $v = 0$  by the scattering force during its flight through the trapping beams. For simplicity, the atom is treated as a two-level system in counter-propagating light fields, indicated by the two effective propagation vectors of the light field, defined below. We approximate the scattering force as

$$\mathbf{f}_s \approx \frac{\hbar \mathbf{k}_{\text{eff}} \Gamma}{2} \left\{ \frac{I(\mathbf{x})/I_{\text{sat}}}{1 + I(\mathbf{x})/I_{\text{sat}} + 4(\Delta_+/\Gamma)^2} - \frac{I(\mathbf{x})/I_{\text{sat}}}{1 + I(\mathbf{x})/I_{\text{sat}} + 4(\Delta_-/\Gamma)^2} \right\}, \quad (3.1)$$

where  $\Delta_{\pm} = \Delta_0 \pm |\mathbf{k}_{\text{eff}} \cdot \mathbf{v}|$  is the Doppler-shifted detuning ( $\Delta_0$  is the detuning of the laser frequency from the atomic resonance and  $\mathbf{k}_{\text{eff}}$  is the effective propagation vector for the light field),  $I(\mathbf{x})/I_{\text{sat}}$  is the ratio of the laser intensity at position  $\mathbf{x}$  to the saturation intensity of the atomic transition, and  $\Gamma$  is the natural linewidth of the transition (see Eq. 2.6). For Li,  $\Gamma/2\pi \sim 5.9$  MHz. In our experiment the propagation axes of the trapping beams lie along the  $\pm(1,0,0)$ ,  $\pm(0,1,0)$ , and  $\pm(0,0,1)$  axes, while

the mean atomic velocity is approximately along the (1,1,1) direction (the axis of the oven). We incorporate this geometry into a one-dimensional model by combining each beam's contribution to the net scattering force into a mean force acting parallel and another acting antiparallel to the mean atomic flight path. This amounts to taking  $|\mathbf{k}_{\text{eff}}| \sim k/\sqrt{3}$ . In making the above approximation, we neglect polarization gradient-type forces (which are negligible for Li) and stimulated forces. Furthermore, we neglect the Zeeman shifts due to the presence of the magnetic fields. To find the capture velocity we integrate the one-dimensional classical equation of motion using the force law specified in Eq. 3.1.

Two experimentally adjustable parameters significantly influence the magnitude of the capture velocity  $v_c$ : laser beam power and laser beam diameter. Using the model described above, we numerically explored these dependencies within experimentally accessible limits of laser beam power and diameter. The results are depicted in Fig. 3.2(a), where we have calculated loading rate  $R$  as a function of beam diameter and power. In obtaining  $R$  we have approximated the trapping light fields as being confined to a cube of volume  $d^3$  oriented with the entrance face perpendicular to the mean atomic velocity, and have taken a flat-top intensity distribution for the laser beams (we found the loading rates for Gaussian beam profiles to be comparable to those of flat-top profiles). Figure 3.3(a) illustrates the velocity dependence of the slowing force.

### 3.3 Experimental setup

Our magneto-optic trap was of a standard design [7]. Two anti-Helmholtz coils generated a magnetic field gradient of 6 G/cm along the symmetry axis of the coils. The base pressure of the vacuum system was typically  $2 \times 10^{-9}$  torr at an oven temperature of 380°C. The 671-nm output of a dye laser was frequency stabilized to the  $^7\text{Li } 2S_{1/2}, F = 2 \rightarrow 2P_{3/2}, F = 3$  optical resonance with a saturated absorption locking technique. A resonant electro-optic modulator, driven at 816 MHz, was used to generate a repumping sideband resonant with the  $2S_{1/2}, F = 1 \rightarrow 2P_{3/2}$  transitions. The first-order sidebands each had 30% of the power of the carrier, hence the light

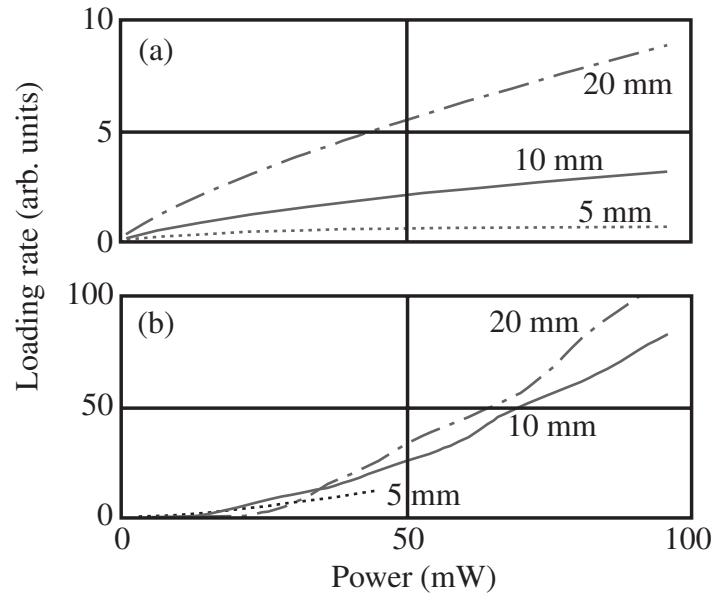


Figure 3.2: (a) Loading rate as a function of laser power and beam diameter for single laser frequency loading using the model described in the text. (b) Loading rate as a function of power and beam diameter for multiple frequency loading. In both cases, power specifies the total laser power in three trapping beams (the total available laser beam power for our retro-reflected laser beam geometry). A saturation intensity of  $I_{sat}=5.2 \text{ mW/cm}^2$  was used for these plots.



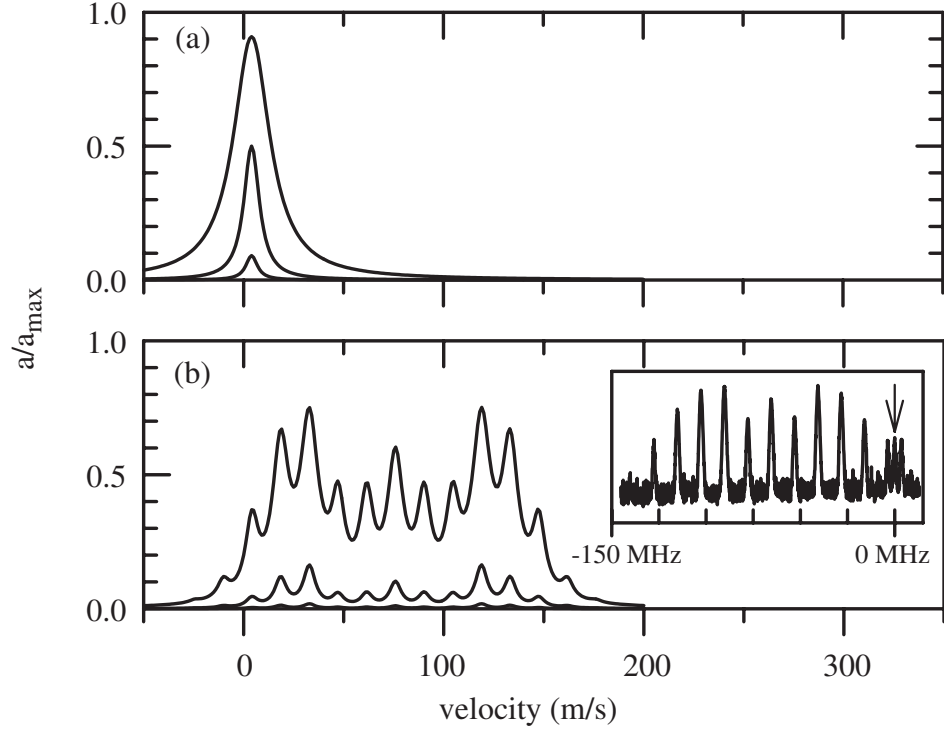


Figure 3.3: Calculation of acceleration *vs.* velocity for various laser beam intensities for (a) single frequency loading and (b) multiple frequency (comb) loading. The intensities used were  $I/I_{\text{sat}} = 0.1, 1$ , and  $10$ , where  $I$  is the combined intensity for three laser beams. For our geometry,  $a_{\text{max}} \equiv \hbar k_{\text{eff}} \Gamma / 2m$ . The inset shows the optical heterodyne between the comb beam and the 816-MHz repumping sideband of the single-frequency trapping beam. The comb parameters (modulation index and sideband separation) are those used to obtain the curves shown in Fig. 3.2(b). The arrow corresponds to the relative frequency of the -5.5-MHz detuned single-frequency trapping beams.



in the sideband that was unused was power effectively lost from the experiment. The  $1/e^2$  laser beam diameter was fixed at 1.1 cm and the laser frequency was detuned  $-5.5 \pm 0.5$  MHz from the  $2S_{1/2}, F = 2 \rightarrow 2P_{3/2}, F = 3$  resonance. To measure the number of atoms we used a ballistic expansion technique: we first simultaneously turned off the trapping beams and the magnetic field after a preset loading interval, then waited 2 ms before pulsing on the trapping beams at 40 mW/cm<sup>2</sup> intensity. (In this and subsequent references to measured intensity or power in this chapter, we refer to the intensity or power of the carrier plus *both* of the 816-MHz sidebands.) The 2-ms interval for ballistic expansion allowed simultaneous determination of the trap temperature and number by imaging the spatial profile of the expanding cloud of atoms. The magnetic field switched off in less than 1 ms. We determined the number of atoms from the integrated fluorescence imaged onto a charge-coupled-device (CCD) array during a 100- $\mu$ s exposure.

Our measurements of the loading rate as a function of beam power, shown in Fig. 3.4(a), are in good agreement with power scaling predicted by the model presented above. The loading rate was determined by taking the ratio of the number of captured atoms to the loading time, in a regime where the number loaded was linear with loading time.

### 3.4 Spectrally-broadened laser light

Further gains are possible by spectrally tailoring the laser cooling and trapping light. An increase in spectral width increases the capture velocity by allowing the laser light to efficiently couple to the Doppler-shifted resonances of faster atoms. For our experiment an electro-optic modulator was used to broaden the trapping light source. The electro-optic modulator was resonantly driven at 12.5 MHz to produce a series of frequency sidebands, ranging nominally in frequency from 134 MHz (minus fifth order) to 9 MHz (plus fifth order) below the  $2S_{1/2}, F = 2 \rightarrow 2P_{3/2}, F = 3$  transition. We refer to the spectrally broadened light as a frequency comb.

We incorporate the comb into the model for loading efficiency by modifying the expression for the scattering force to reflect the presence of the additional spectral

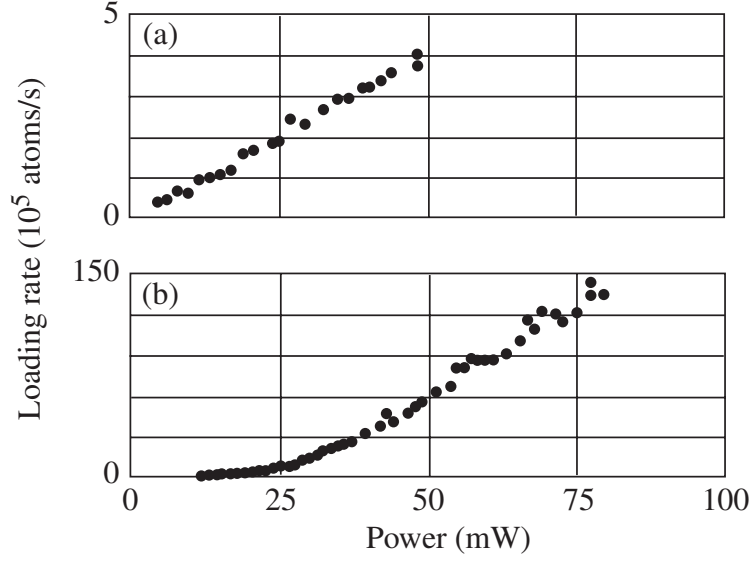


Figure 3.4: Measured loading rates for (a) single-frequency loading and (b) comb loading. Power refers to the total laser power in three trapping beams.

components in the radiation field. In the low-intensity limit each sideband contributes a force component given by Eq. 3.1, yielding a net force

$$\mathbf{f}_{comb} \approx \frac{\hbar \mathbf{k}_{eff} \Gamma}{2} \sum_i \left\{ \frac{I_i(\mathbf{x})/I_{sat}}{1 + I_i(\mathbf{x})/I_{sat} + 4(\Delta_{+,i}/\Gamma)^2} - \frac{I_i(\mathbf{x})/I_{sat}}{1 + I_i(\mathbf{x})/I_{sat} + 4(\Delta_{-,i}/\Gamma)^2} \right\}, \quad (3.2)$$

where the index  $i$  ranges over the sidebands in the comb,  $I_i(\mathbf{x})$  is the intensity in the  $i$ th sideband, and  $\Delta_{\pm,i} = \Delta_{0,i} \pm |\mathbf{k}_{eff} \cdot \mathbf{v}|$  is the Doppler-shifted detuning of the  $i$ th sideband. Figure 3.3(b) shows a plot of Eq. 3.2 for the frequency parameters used in our experiment at various laser beam powers. The resulting loading rates are shown in Fig. 3.2(b).

Experimentally we inferred as much as a factor of 22 improvement in loading rate

over the maximum rate observed with single-frequency loading<sup>1</sup>. For these observations a second beam of 1.3 cm  $1/e^2$  diameter, having the comb frequency spectrum described above, was made to co-propagate with the original single-frequency beams. The six single-frequency beams were detuned from resonance by -5.5 MHz and each had a peak intensity of  $100 \mu\text{W}/\text{cm}^2$ . The observed loading rate, shown in Fig. 3.4(b) as a function of total power in three (of the six) comb beams, was in good agreement with the simple models. These models predicted a factor of  $\sim 17$  improvement for a power of 64 mW and a 1 cm beam diameter. (For comparison with theory, the measured powers had to be scaled to account for the fraction of power in the nonresonant 816 MHz sideband. In this case 64 mW was the power in the carrier and the resonant repumping sideband corresponding to the measured 80 mW of total power.) Extrapolating our single-frequency loading data in Fig. 3.4(a) to 80 mW of power (neglecting the predicted saturation in loading rate), we inferred a factor of 22 improvement. We characterized the frequency spectrum of the comb with an optical heterodyne between the comb beam and an unmodulated reference beam [see inset of Fig. 3.3(b)].

The use of two sets of beams gave us independent control over the trap loading parameters, determined to a large extent by the comb beams, and the trap cooling parameters, which were set by the single-frequency trapping beams. With two sets of beams, for example, we were able to load the trap with both sets on, then turn the comb beams off, leaving the single-frequency beams to cool and compress the loaded atoms.

The number of atoms loaded into the trap after a fixed time depended not only on the loading rate, but also on the rate at which atoms were ejected from the trap. Three important collision-induced ejection mechanisms were background gas collisions with thermal atoms, fine-structure changing collisions, and radiative-escape collisions [65]. The net ejection rate depended on the collision rate pertinent to each

---

<sup>1</sup>The operating detuning for the single-frequency beam was that used to optimize temperature and density of trapped atoms. Our model predicts substantial improvements in the single-frequency loading rate at larger detunings. For example, the loading rate at -6.5  $\Gamma$  detuning with 64 mW power in three beams of 1 cm diameter is  $\sim 7$  times that for the parameters used to generate Fig. 3.2(a). This improved loading rate would be at the expense of trap temperature and density. We can, however, switch to smaller detunings after loading in order to optimize temperature and density.

mechanism, the kinetics of the collision mechanism, and the depth of the trap. It has been noted that the fine-structure ejection mechanism for lithium traps can be suppressed for sufficiently deep traps [66, 67]. In the fine-structure changing collision,  $\text{Li}(2S_{1/2}) + \text{Li}^*(2P_{3/2}) \rightarrow \text{Li}(2S_{1/2}) + \text{Li}^*(2P_{1/2}) + \Delta E_{\text{FS}}$ . The resulting kinetic energy  $\Delta E_{\text{FS}}$  corresponds to a final velocity of  $v_{\text{FS}} = 24 \text{ m/s}$  for each interacting atom (the atoms are nearly at rest before the collision), which can be smaller than the capture velocity of the magneto-optic trap. Thus the collision products may be recaptured. The situation is different for the heavier alkali metals such as Cs and Rb, where the fine-structure splitting is much greater than the 10 GHz interval of Li.

We experimentally characterized the collision-induced loss process by observing the decay in the number of trapped atoms as a function of trap depth. We varied trap depth by changing the intensity of the trapping beams. For these measurements, we first loaded the trap with the comb on and a fixed intensity for the single-frequency trapping beams. After loading  $\sim 6 \times 10^7$  atoms into the trap, the comb beams were turned off and the single-frequency trapping intensity was switched to the intensity needed for the decay measurement. By monitoring the decay in fluorescence, we extracted the normalized number loss rate,  $(1/N)dN/dt$  ( $N$  is the number of trapped atoms), for the time interval immediately following the extinction of the comb beams. At low intensities, the loss rate increases linearly with intensity and the number of trapped atoms in the  $2P_{3/2}$  state, as shown in Fig. 3.5.

At higher intensities the trap became sufficiently deep to recapture fine-structure-changing collision products. We made a crude estimate of trap depth using methods similar to those used above to estimate loading efficiency. In general, the threshold intensity for recapture depends on the angle of ejection relative to the propagation axes of the trapping beams. If we considered flight along the (1,1,1) axis, we estimated a recapture intensity of  $\sim 20 \text{ mW/cm}^2$  for our trap parameters, in reasonable agreement with the data.

The success of the comb-loaded Li trap may hinge on its ability to recapture decay products. In general, the presence of nearly resonant, red-detuned light produces fine-structure changing collisions by inducing transitions to excited molecular states [65]. For Li this collision rate varies only weakly with detuning for the detuning range

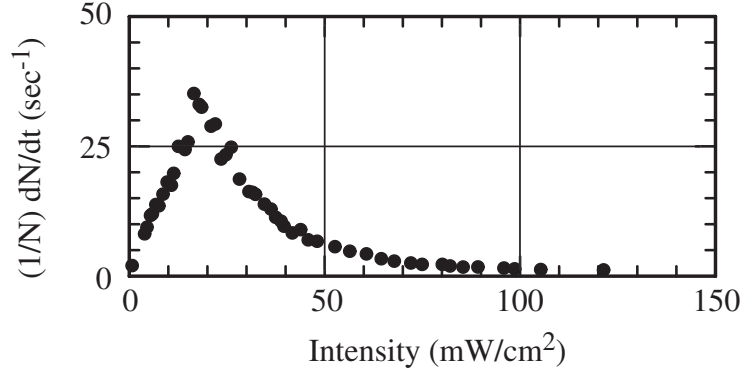


Figure 3.5: Normalized trap loss rate  $(1/N)dN/dt$  as a function of total trap intensity (i.e., the combined intensity for *six* trapping beams). The loss rate was measured in a  $\sim 10$ -ms interval just following the extinction of the comb beams.

used to generate the comb light [68]. If the trap is not deep enough to recapture fine-structure collision products, the presence of the comb light might induce a trap loss which could prevent a significant buildup of atoms. These collisions may have been responsible for the failure of earlier efforts to trap with broadband laser sources, where the work was done with heavier alkali metals [64, 69]. The comb technique might be used for other species if the central area of the comb beam profile is blocked, thus producing a region where trapped atoms can accumulate without suffering additional comb-induced losses [70, 71]. We note, however, that the excited-state hyperfine structures of the heavier alkali metals are significantly different from Li. Finally, loss rates due to background gas collisions and radiative escape should also be reduced due to the substantial increase in trap depth.

In addition to improving the trap loading rate with the comb scheme, we also observed improvements in trap density. Under the conditions described above, we observed densities as high as  $2_{-1}^{+2} \times 10^{11}$  atoms/cm<sup>3</sup>. We determined the density by measuring the absorption of a weak probe beam at several detunings from the  $2S_{1/2} \rightarrow 2P_{3/2}$  transition. We checked the density measurement with our CCD imaging system by analyzing the spatial intensity distribution of scattered light during the detection pulse.

### 3.5 Trap images

With certain unusual beam alignments and intensity balances, the multiple frequencies of the comb light could produce interference patterns in the beam intersection region. This was due to super-lattice-type interference of the various frequencies in the superimposed comb beams and single-frequency trapping beams. The interference produced interesting arrangements of atoms in the MOT. These special traps were not used in the experiment; however, images of a few of these traps are shown in Figs. 3.6 and 3.7 for the uniqueness and beauty of their configurations. The images were recorded on a CCD camera with light that was scattered by the trapped atoms from the resonant trapping beams. The image widths are  $\sim 1$  cm.

### 3.6 Summary

By locating the Li oven nozzle near the MOT and by using spectrally broadened laser trapping light, we increased the capture efficiency of a  $^7\text{Li}$  MOT. The gains obtained and the techniques developed were beneficial to subsequent and continuing Li experiments in our laboratory, particularly to the experiments described in Chapter 4.

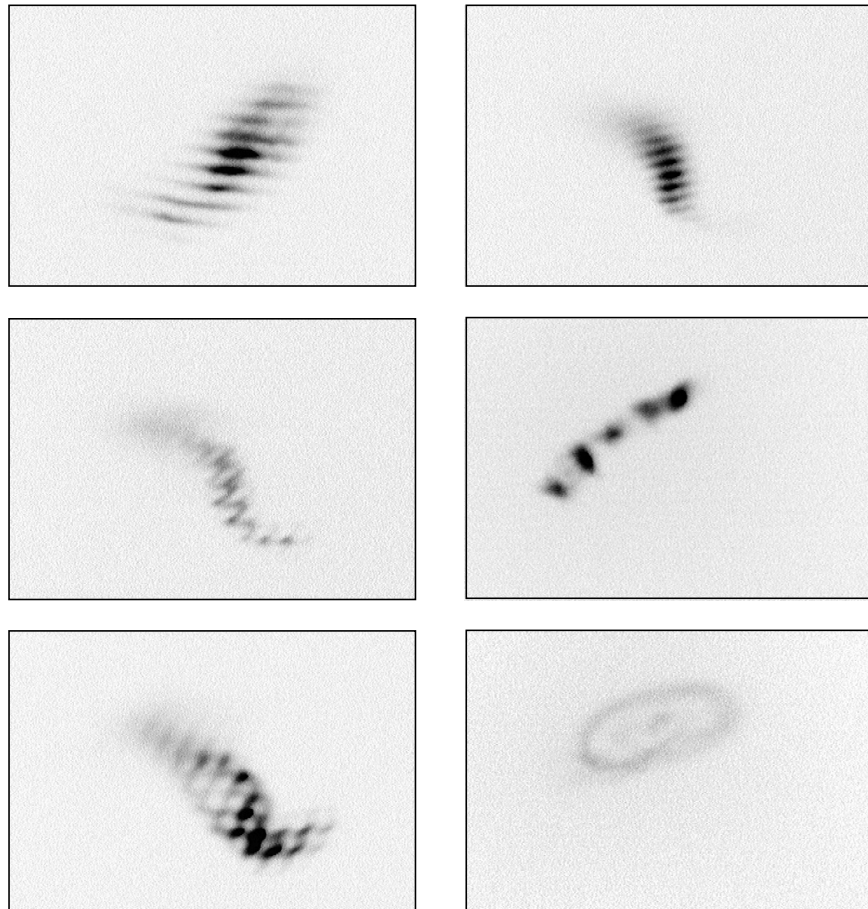


Figure 3.6: Images of trapped Li atoms (dark regions) in the comb-loaded MOT, obtained with particular beam alignments and intensity balances.



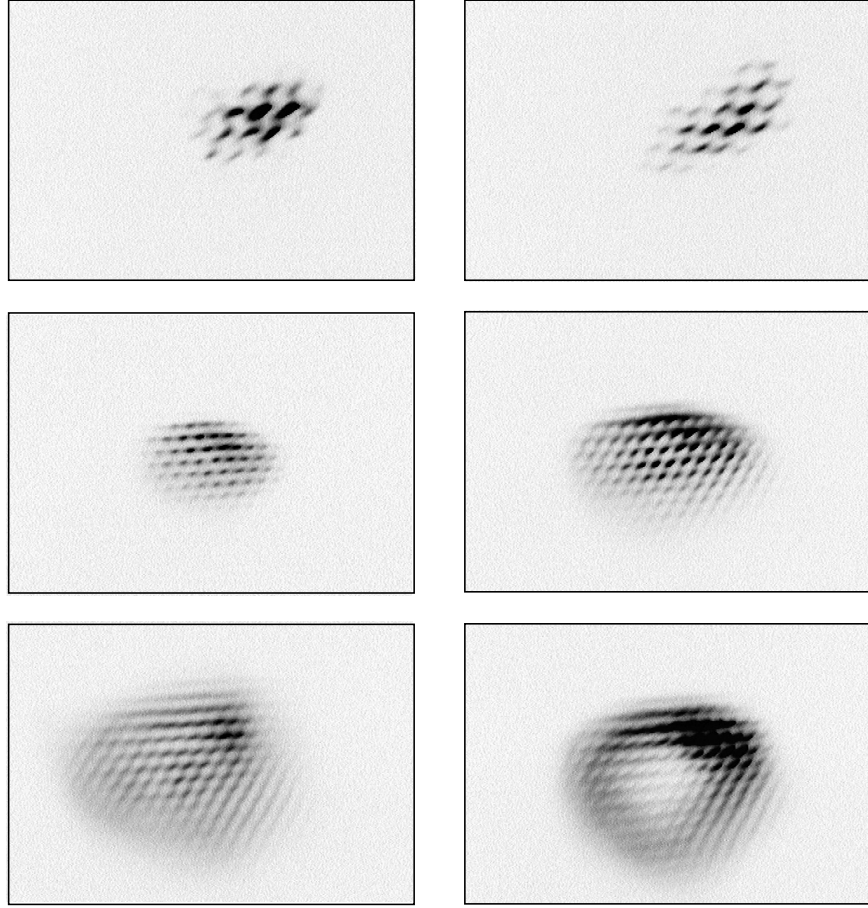


Figure 3.7: Images of trapped Li atoms (dark regions) in the comb-loaded MOT, obtained with unusual beam alignments and intensity balances. The interference patterns created atoms traps that resembled two-dimensional super-lattice arrangements. In these traps, multiple frequencies interfere to produce a net potential with a period determined by the beatnote frequency between the beams.

# Chapter 4

## Trapping $^7\text{Li}$ in an optical lattice

### 4.1 Motivation

Atom trapping in spatially periodic light-induced potentials and the study of atomic center-of-mass motion in such optical lattices has been an area of intense interest in the laser cooling and atom trapping field. Important results have included the discovery of sub-Doppler laser cooling mechanisms [4, 5, 6], observation of Lamb-Dicke confinement of atoms [72], quantization of atomic motion [15, 16, 73, 74, 75], and focusing properties of standing waves on atom trajectories. A feature common to these studies was that the atom-laser interactions were in a regime where spontaneous emission damps the atomic motion.

Since the time that the experiment described in this chapter was performed, interest in optical lattices has grown. For example, current lattice work is aimed at studying the potential use of optical lattices for applications to nano-fabrication with atoms [76] and the possibility of evaporatively cooling atoms in a lattice with the goal of reaching Bose-Einstein condensation [77].

The goal of our experiment was to reach ultra-cold temperatures of trapped lithium atoms. As mentioned previously, ultra-cold atomic sources have important applications in precision measurements [8, 9, 10, 12, 78] as well as in studies aimed at observation of quantum many-body effects in dilute vapors [79].

## 4.2 A far-detuned optical lattice for Li

In this experiment, we studied the motion of lithium atoms in an optical lattice created by laser light far-detuned from the atomic resonance [42]. In this limit, optical dipole forces dominate non-conservative scattering forces, with important consequences. First, this allows construction of lattices with potential well periodicities greater than the wavelength of the lattice trapping light. Such lattices are capable of confining ensembles of atoms with mean kinetic energy less than the photon recoil limit  $E_R = (\hbar k)^2/2m$  ( $k = \lambda/2\pi$  is the wavenumber of the lattice laser beam and  $m$  is the atomic mass). Because of the atom's greater position uncertainty, lower momentum uncertainty and thus sub-recoil energies may be achieved with large periodicity wells. Second, such lattices only weakly perturb the internal energy levels of the atom while providing strong spatial confinement. Thus, far-detuned lattices may provide an excellent environment for high-resolution spectroscopic studies. Finally, under certain conditions, the time between spontaneous emission events can be much longer than the time an atom resides in a primitive lattice cell. In that case, quantum coherence plays a significant role in wavepacket motion through the lattice, enabling studies of, for example, dynamical localization [80], and more recently, observations of Bloch oscillations in an optical lattice [81].

In our experiment, 3-dimensional lattices of laser intensity maxima and minima were formed from the interference of four mutually intersecting laser beams. The frequency of the lattice laser beams was tuned near the Li  $2S_{1/2} \rightarrow 2P_{3/2}$  transitions. The ac Stark shifts of the atomic energy levels due to the lattice laser beams were comparable to the  $140\mu\text{K}$  initial kinetic energy of the laser-cooled atoms. The detuning of these beams was far enough from the  $2S \rightarrow 2P$  transitions that weak excitation to the  $2P$  levels resulted in a spontaneous emission rate of less than 1 photon every 10 ms. Atoms were confined in lattices for times on the order of  $\sim 100$  ms using laser detunings as large as 10 nm to the red or 1 nm to the blue of the  $2S \rightarrow 2P$  atomic resonances. With red-detuned light atoms were trapped near intensity maxima, while for blue-detuned light atoms were trapped near intensity minima.

Once confined in the lattice, atoms were cooled by adiabatically reducing the

intensity of the lattice laser light. A reduction in light intensity in the lattice reduces the depths of the potential wells that comprise the lattice. For a sinusoidal lattice (or other curved potentials, such as Gaussian wells), this causes the widths of the bound states to increase and the trapping spring constants to decrease. The kinetic energy of the states thus decreases, reducing the temperature, while the density increases. Adiabatic cooling has been used to cool Cs atoms to temperatures of  $\sim 6 T_R$  ( $k_B T_R \equiv E_R$ ) in three dimensions [49], and previously to cool Li in one dimension to  $\sim 4 T_R$  [50]. In principle, cooling in lattices of periodicity greater than  $\lambda$  can produce effective temperatures below the single photon recoil limit. Final temperatures, however, are also limited by the initial energy distribution of atoms confined in the lattice. In our experiments, final effective temperatures were  $\sim 26 T_R$  ( $80 \mu\text{K}$ ), a factor of  $\sim 2$  colder than the initial temperature in our optical lattice.

We also demonstrated that large periodicity lattices can support rms momentum spreads of less than a photon recoil. This has been accomplished by reducing the initial intensity of the lattice light so that only the coldest atoms from the atomic source are confined by the lattice. Using this technique, we have prepared ensembles having an effective temperature of  $0.6 T_R$  ( $1.8 \mu\text{K}$ ).

## 4.3 Experiment

### 4.3.1 Apparatus

The experimental details are as follows. The output of a dye laser tuned near the 671-nm  $2S_{1/2} \rightarrow 2P_{3/2}$  resonance of lithium was split into four separate beams made to intersect inside a UHV vacuum chamber with a base pressure of  $5 \times 10^{-9}$  torr. The beams were focused to a  $1/e^2$  diameter of  $500 \mu\text{m}$  at the point of intersection and were aligned to propagate along the  $[1,0,0]$ ,  $[0,1,0]$ ,  $[0,0,1]$  and  $[1,1,1]$  directions. Due to the low spontaneous emission rates, lattice propagation vectors need not be chosen to balance spontaneous scattering forces. For laser detunings to the red of the  $2P$  resonances, the beams were linearly polarized in the  $[0,1,1]$ ,  $[1,0,-1]$ ,  $[1,-1,0]$  and  $[1,-1,0]$  directions, respectively. In this geometry, the corresponding primitive lattice

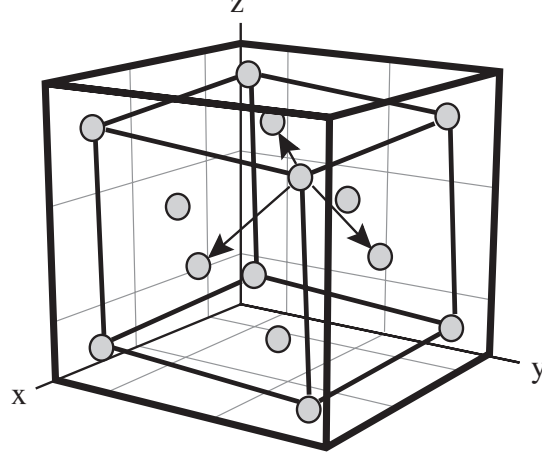


Figure 4.1: Illustration of the red-detuned optical lattice geometry. The primitive translation vectors of the periodic lattice are shown with arrows, and the high-intensity regions by filled circles.

translation vectors are  $\mathbf{a}_1 = \lambda[\sqrt{3} - 2, 1, 1]/(3 - \sqrt{3})$ ,  $\mathbf{a}_2 = \lambda[1, \sqrt{3} - 2, 1]/(3 - \sqrt{3})$ , and  $\mathbf{a}_3 = \lambda[1, 1, \sqrt{3} - 2]/(3 - \sqrt{3})$ . The corresponding nearest-neighbor spacings are  $|\mathbf{a}_i| = 1.13\lambda$  ( $i = 1, 2, 3$ ) (Fig. 4.1).

For blue detunings we used orthogonal-linear polarizations for the first three beams, and chose circular polarization for the beam along the  $[1,1,1]$  axis to create pockets of near-darkness surrounded by regions of high-intensity light. The spatial density of potential wells was  $\sim 10^{12} \text{ cm}^{-3}$ . By defining the lattice with just four beams, time-phase fluctuations in the relative phases of the interfering beams translate the lattice but do not alter the shape of the lattice potential [16]. The potentials for the red and blue detuned lattices are represented in Figs. 4.2 and 4.3.

Lattices with periodicity much larger than  $\lambda$  in 3 dimensions can be created by reducing the angles subtended by each possible pair of the four lattice beams. For example, if the beams propagate parallel to the axes defined by the vectors  $[0,1,0.1]$ ,  $[0,1,-0.1]$ ,  $[0.2,1,0]$ , and  $[-0.2,1,0]$ , the magnitudes of the corresponding primitive translation vectors are  $|\mathbf{a}_1| = 5.10\lambda$ ,  $|\mathbf{a}_2| = 5.63\lambda$ , and  $|\mathbf{a}_3| = 34.68\lambda$ .

The primitive translation vectors have been derived using the following method.

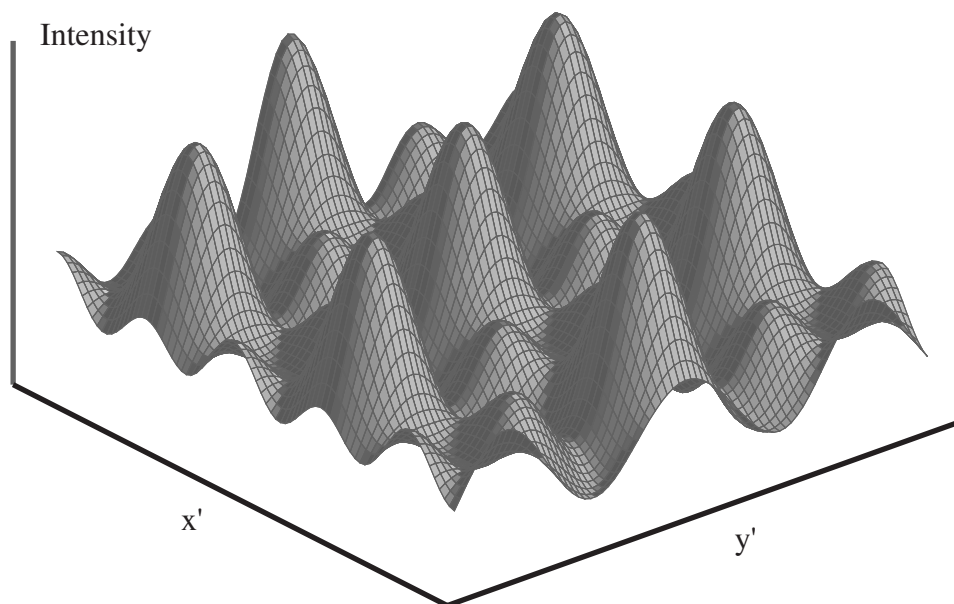


Figure 4.2: Cross-sectional view of the interference pattern for a red detuned lattice. The  $x' - y'$  cut is perpendicular to the  $[1,1,1]$  axis.

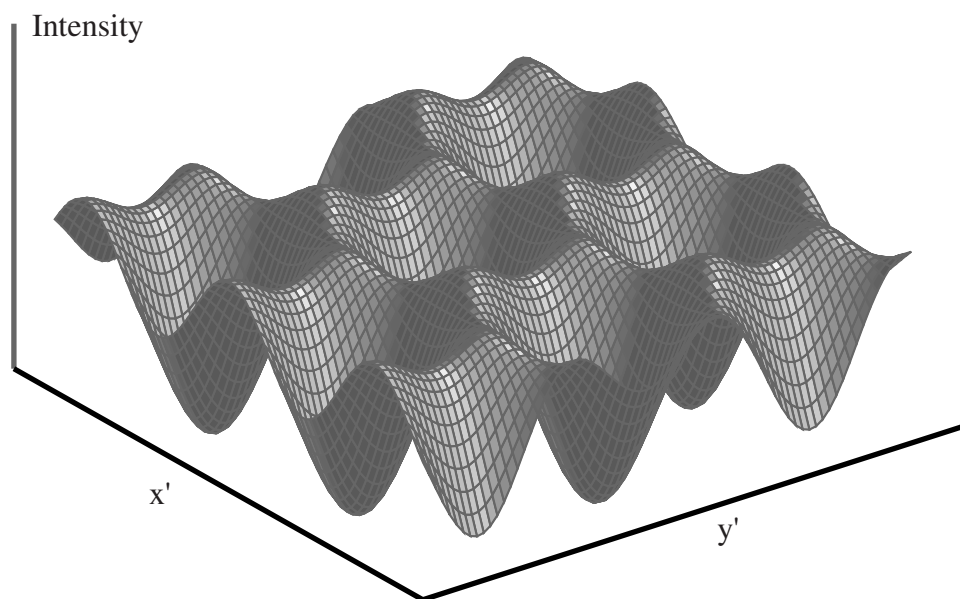


Figure 4.3: Cross-sectional view of the interference pattern for a blue detuned lattice. The  $x' - y'$  cut is perpendicular to the  $[1,1,1]$  axis.

First, we form a set of reciprocal lattice vectors

$$\mathbf{q}_1 = \mathbf{k}_1 - \mathbf{k}_2, \quad (4.1)$$

$$\mathbf{q}_2 = \mathbf{k}_1 - \mathbf{k}_3, \quad (4.2)$$

$$\mathbf{q}_3 = \mathbf{k}_1 - \mathbf{k}_4, \quad (4.3)$$

where  $\mathbf{k}_1$ ,  $\mathbf{k}_2$ ,  $\mathbf{k}_3$ , and  $\mathbf{k}_4$  are the propagation vectors for the lattice laser beams. From these we derive a set of lattice translation vectors

$$\tilde{\mathbf{a}}_1 = 2\pi(\mathbf{q}_2 \times \mathbf{q}_3)/\mathbf{q}_1 \cdot \mathbf{q}_2 \times \mathbf{q}_3, \quad (4.4)$$

$$\tilde{\mathbf{a}}_2 = 2\pi(\mathbf{q}_3 \times \mathbf{q}_1)/\mathbf{q}_1 \cdot \mathbf{q}_2 \times \mathbf{q}_3, \quad (4.5)$$

$$\tilde{\mathbf{a}}_3 = 2\pi(\mathbf{q}_1 \times \mathbf{q}_2)/\mathbf{q}_1 \cdot \mathbf{q}_2 \times \mathbf{q}_3. \quad (4.6)$$

We then form the set of translation vectors  $i\tilde{\mathbf{a}}_1 + j\tilde{\mathbf{a}}_2 + k\tilde{\mathbf{a}}_3$  ( $i, j$ , and  $k$  integers) from which we extract the three primitive translation vectors. This algorithm has been checked with numerical calculations of the interference patterns.

The periodic potential  $U_0(\mathbf{x})$  induced by the ac Stark shift of the ground-state atomic energy levels is  $U_0(\mathbf{x})/\hbar = \sum_i \Omega_{r,i}^2(\mathbf{x})/\Delta_i$ , where  $\Omega_{r,i}(\mathbf{x})$  is the Rabi frequency for the  $i$ th optical transition and  $\Delta_i$  is the detuning from this transition. This expression is strictly valid in the limit where the detunings are much larger than the natural linewidths (5.9 MHz for the Li  $2P$  resonances), and is an excellent approximation for the detunings in our experiments. In principle the potential strength also depends on the polarization of the light at position  $x$  and the ground-state Zeeman sublevel of the atom. However, in the limit where the detuning is much larger than the excited-state fine-structure splitting, these dependencies become negligible. For Li, the  $2P_{1/2}$  level is separated from the  $2P_{3/2}$  level by only 10 GHz, so this approximation holds in our experiments. The power in each of the four beams was 50 mW for the red-detuned lattice, which gave a peak intensity of 560 W/cm<sup>2</sup> at each lattice well site. At an intensity of 560 W/cm<sup>2</sup> and detuning of 1 nm, the ground state energy shift is  $23 E_R$ . The lattice potential is conservative in so far as the atom does not spontaneously scatter lattice photons. Since the scattering rate is  $\tau_{scat}^{-1} \sim \Gamma(\Omega_r^2/\Delta^2)$  in the limit



$\Delta \gg \Gamma$ , high laser intensities and large detunings are required for deep lattices and low scattering rates. For  $560 \text{ W/cm}^2$  intensity and  $1 \text{ nm}$  detuning, the scattering time is  $\sim 12 \text{ ms}$ . With a blue-detuned lattice, the linearly polarized beams each had  $33 \text{ mW}$  power, while the circularly polarized beam had  $100 \text{ mW}$  power, yielding a peak intensity of  $\sim 300 \text{ W/cm}^2$ .

### 4.3.2 Experimental sequence

We loaded atoms into the lattice from a MOT using the methods described in Chapter 3. Separate dye lasers were used to generate the laser light for the MOT and for the lattice. We routinely achieved densities of  $2 \times 10^{11} \text{ atoms/cm}^3$  at temperatures of  $140 \mu\text{K}$  after a  $300\text{-ms}$  loading time. The initial  $1/e$  diameter of the MOT was  $\sim 200 \mu\text{m}$ .

The method for loading atoms from the MOT into the dipole-force lattice (DFL) depended on the detuning of the lattice laser light. For red lattice detunings, the lattice light was turned on during the final  $6 \text{ ms}$  of the MOT loading cycle, after which the MOT trapping beams and magnetic field gradient were turned off. Figure 4.4 is an image of Li atoms (bright dot in center) held in a red-detuned dipole trap, scattering light from the resonant MOT cooling and trapping beams (visible in the image due to light scattering off of untrapped Li atoms in the chamber). For blue detunings, the DFL beams were turned on at the instant that the MOT light and magnetic field were turned off. When the blue-detuned lattice light was on concurrently with the MOT light, atoms were found to be ejected from the trapping region.

We optimized the loading parameters by maximizing the number of atoms loaded into the lattice. After confining atoms in the DFL for a fixed holding time following the turn-off of the MOT, the DFL was switched off (switching time  $\sim 10 \mu\text{s}$ ) and the optical molasses light was turned back on for  $\sim 100 \mu\text{s}$ . Light scattered from the atoms during this interval was imaged onto a calibrated CCD camera. The number of atoms was then extracted from the digital image of the atomic distribution.

To align the lattice beams, we loaded atoms into traps formed by the intersection of pairs of the four red-detuned beams. This was done at a detuning where the dipole

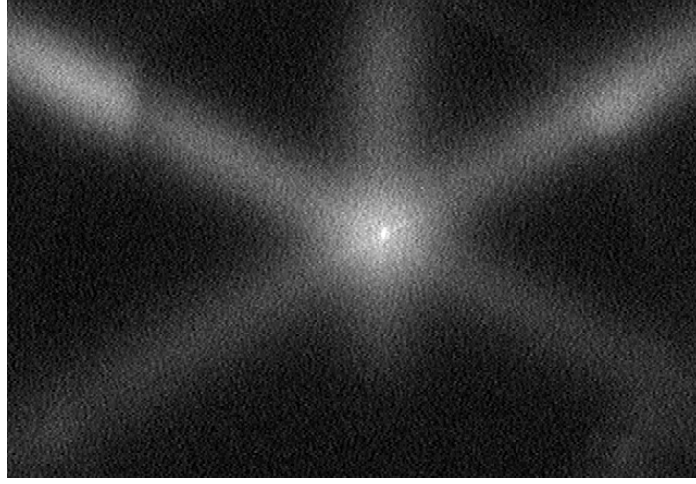


Figure 4.4: A red-detuned Li dipole trap. Li atoms (bright dot in center) are held in the dipole trapping beams. The trapped atoms, along with untrapped Li atoms, scatter light from the resonant laser cooling beams (broad light-colored areas).

forces from a single beam were not sufficient to support atoms against gravity, but where the forces from a pair of beams trapped atoms in the beam intersection region. By maximizing the number of atoms trapped for each of the 6 possible independent beam-pair combinations, we were able to optimize the mutual overlap of all four beams. The alignment was then checked by tuning the lattice laser to the blue of the atomic resonance, changing the beam polarizations to those for a blue-detuned lattice, and then verifying that atoms remained confined in the overlap region. In the blue-detuned lattice configuration, atoms were confined only when all four beams intersected.

The number of atoms remaining in the lattice as a function of holding time after the MOT was turned off is shown in Fig. 4.5. For these curves, the lattice laser beams were detuned 0.5 nm and 1 nm to the red of the  $2P$  resonance, corresponding to maximum well depths of  $46 E_R$  and  $23 E_R$  respectively. These curves were characterized by an initial fast decay followed by a longer exponential decay.

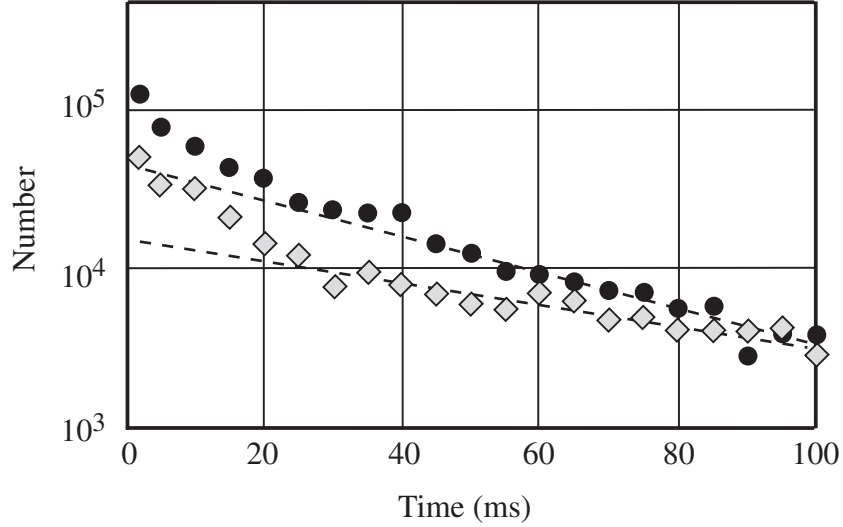


Figure 4.5: Number of atoms remaining in lattice *vs.* confinement time for detunings of 0.5 nm (circles) and 1.0 nm (diamonds).

### 4.3.3 Trap loss

Spontaneous emission heats the atoms, taking them from bound states to nearly free states where they quickly leave the lattice region. The calculated time for an atom to gain enough kinetic energy to escape agrees well with the measured long exponential decay time. We verified this interpretation by measuring the loss rate for a lattice of the same strength, but having twice the spontaneous emission rate. This was done by reducing both the intensity and detuning by a factor of two. The observed long exponential decay was twice as fast as that of the original lattice, which is consistent with the factor of two increase in the heating rate.

Another escape mechanism is diffusion of unbound atoms from the lattice region to the lattice edges. From Monte Carlo simulations of classical particle motion in the conservative lattice potential we find that, over the range of energies  $-0.4 U_{\text{max}} < E < 0.2 U_{\text{max}}$ , particle motion is classically chaotic for the red detuned lattices ( $-U_{\text{max}}$  is the lattice potential minimum), as illustrated in Fig. 4.6(a). For energies near  $-0.4 U_{\text{max}}$ , diffusion is anomalous, with atomic motion dominated by Levy flights.

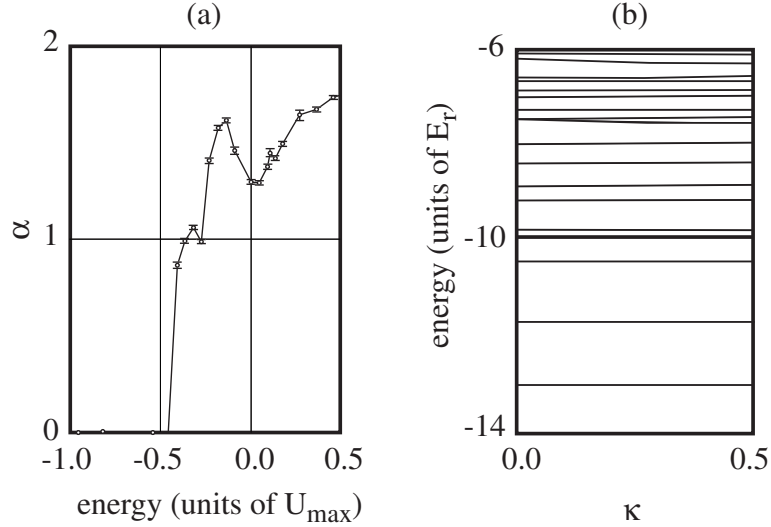


Figure 4.6: (a) Results of a Monte Carlo simulation of classical particle motion in the lattice. Particles of energy  $E$  were initially randomly positioned in a primitive lattice cell at time  $t = 0$ . The subsequent mean-squared displacement  $\langle \mathbf{x}(t)^2 \rangle$  of the distribution was parameterized as  $Ct^\alpha$ . For energies  $-U_{\max} < E < -0.4U_{\max}$ ,  $\alpha = 0$  since particles are confined in potential minima (there is a saddle point in the potential at  $-0.4U_{\max}$ ). For  $\alpha = 1$ , motion is diffusive, while for  $\alpha = 2$  motion is ballistic. (b) Energy *vs.* quasi-momentum for quasi-momentum  $\mathbf{q} = \kappa\mathbf{q}_1$ , where the reciprocal lattice vector  $\mathbf{q}_1 = (2\pi/\lambda)(1 - \sqrt{3}, 1, 1)/\sqrt{3}$  and  $0 \leq \kappa \leq 0.5$ .

Related studies of classically chaotic transport in 2-D periodic lattices were done by D. Chakovsky and G. Zaslavsky [82] and T. Geisel *et al.* [83].

From these calculations, we estimate escape times of  $\sim 10$  ms for a 1-nm red-detuned lattice, in rough agreement with the observed fast decay rate. The fast decay was too rapid to be consistent with a collisional loss mechanism. Furthermore, lattice wells are expected to shield collisions for pairs of atoms in adjacent wells, and the probability of finding two atoms in the same well is small ( $\sim 1\%$ ).

A third possible loss mechanism is tunneling to the edges of the lattice. We calculated the energy band structure for our lattice through standard application of the Bloch theorem in order to estimate the importance of this process. Fig. 4.6(b) shows band energy as a function of quasi-momentum along one of the reciprocal lattice

vectors for a red-detuned lattice  $15 E_R$  deep. For the lowest lying energy bands, a tight binding approximation produced band energies which were consistent with the exact calculation. In this limit, atoms are viewed as nearly bound by harmonic potentials near lattice potential minima, with the low-lying band structure arising from tunneling between nearest neighbor lattice sites. From the calculated dependence of the  $n$ th band energy  $E_n$  on quasimomentum  $\mathbf{q}$  we estimated the effective velocities  $v_{\text{eff}} = (1/\hbar)\nabla_{\mathbf{q}}E_n(\mathbf{q})$  in the lattice. We found that the maximum speeds range from 0.01 cm/s to 0.3 cm/s in the lowest 15 bands. In the  $\sim 100$ -ms duration of our experiment, the majority of atoms in these states travel significantly less than the spatial extent of the lattice. We also expect spontaneous emission to dephase the wavepacket coherences necessary to ensure ballistic transport. In this case, atomic motion becomes diffusive rather than ballistic, and the estimated escape times are substantially longer. Finally, other perturbations, such as temporal and spatial fluctuations in lattice strength, may also serve to localize atomic motion.

## 4.4 Velocity selection and adiabatic cooling

We measured the velocity distribution of the trapped atoms using a time-of-flight technique. By imaging the size of the cloud a fixed delay (typically 2 ms) after the DFL beams were turned off, we were able to infer the initial atomic velocity distribution from the ballistic expansion of the ensemble. The optical axis of the imaging system was in the  $[-1,-1,1]$  direction in the coordinate system used above to define the lattice propagation vectors. For strong red-detuned lattice potentials the measured velocity spreads were nearly as large as those of the atoms in the MOT. For weaker lattice potentials, only the coldest atoms in the MOT could be confined, and the measured velocity spreads were lower. For example,  $\sim 4000$  atoms were confined with an rms velocity spread corresponding to an effective temperature of  $1.8\mu\text{K}$ , nearly a factor of 2 below the single photon recoil temperature of  $3\mu\text{K}$ . These measurements were made after a 10 ms holding time in the lattice, and the lattice beams were detuned 10 nm red of the  $2P$  transition. The velocity distributions were observed to be nearly isotropic and nearly Gaussian. We checked for anisotropy in

the third dimension by viewing the cloud from the  $[-1,-1,-1]$  direction.

Atoms confined in the optical lattice were adiabatically cooled by slowly lowering the lattice potential. Atoms are cooled when the change in potential depth is slow enough that atomic population in a given energy band does not make non-adiabatic transitions to adjacent bands during the cooling period. In this limit, the atomic quasi-momentum adiabatically maps onto real momentum as the potential is extinguished. Using this adiabatic approximation and knowing the initial distribution of atomic population in the energy bands allows the final momentum distribution to be calculated. For example, in a 1-D lattice of periodicity  $a$ , atoms initially residing in the  $n$ th energy band have a final momentum  $\mathbf{p}_f$  in the range  $2\pi\hbar(n-1)/a < |\mathbf{p}_f| < 2\pi\hbar n/a$  [49]. In principle, lattices with large periodicities are capable of yielding extremely low final momentum spreads. However, attaining such low effective temperatures requires a mechanism for loading atoms into the lowest energy bands.

Optimum adiabatic cooling results were obtained in a lattice configuration of tight, deep potential wells, where atoms were efficiently loaded into the lowest energy bands. By focusing the red-detuned beams to a  $140\text{-}\mu\text{m}$   $1/e^2$  diameter we achieved a factor of 13 increase in laser intensity. The propagation direction of the  $[1,1,1]$  beam was reversed to reduce the lattice periodicity and the laser was detuned  $\sim 200$  GHz to the red of resonance, resulting in an  $\sim 20 E_R$  energy splitting between the lowest lying bands. By lowering the potential depth exponentially with a  $1/e$  time constant of  $400\text{ }\mu\text{s}$  just after turning off the MOT, the temperature of the ensemble was reduced by a factor of 2, to  $80\text{ }\mu\text{K}$ . We note that cooling performance might be significantly enhanced by using other cooling methods (sideband cooling, for example) to initially prepare atoms in the low-lying energy bands.

## 4.5 Summary

In this experiment, we demonstrated atomic confinement in far-detuned optical lattices. The decreased scattering rate from far-detuned light enabled the construction of lattices with periodicity greater than  $\lambda$  in three dimensions. Atoms were cooled

by adiabatically reducing the intensity of the lattice light, and velocity selected ensembles were prepared by trapping with weak lattices. While the lattices were not practical for quantum many-body experiments, the experiment was a significant step in optical lattice confinement research for cold atoms.

# Chapter 5

## Light-induced atom desorption

### 5.1 Motivation: BEC

The evaporative cooling techniques used to achieve Bose-Einstein condensation [22, 23, 24] rely on loading large numbers of atoms into atom traps with long trap lifetimes. The approach originally taken by Anderson *et al.* [22] was to load Rb atoms into a vapor cell [40] magneto-optic trap and to subsequently transfer atoms into a magnetic trap located in the same cell. Large numbers of atoms and long lifetimes were achieved by optimizing the Rb vapor pressure and by working with long loading times.

We found a simple way to improve such a setup by modulating the vapor pressure such that it is high for initial trap loading and then low again in order to achieve long lifetimes in a magnetic trap. Low-intensity white light was used to increase the loading rate of  $^{87}\text{Rb}$  atoms into a vapor cell MOT by inducing non-thermal desorption of Rb atoms from the stainless steel walls of the vapor cell. An increase in Rb partial pressure reached a new equilibrium value in less than 10 seconds after switching on the broadband light source. After the source was turned off, the partial pressure returned to its previous value in  $1/e$  times as short as 10 seconds.

The technique requires the use of a white light source (WLS) with radiation incident upon the inner walls of the vapor cell. When such a light source is turned on, Rb atoms that coat the inner walls of the stainless steel vacuum chamber are quickly desorbed and the Rb vapor pressure suddenly increases. The vapor pressure



soon returns to equilibrium after the WLS is turned off. This enables loading large numbers of atoms into the MOT in a relatively short amount of time, while preserving the low pressures required for long magnetic trap lifetimes. The WLS method that we describe here is a possible alternative to the double-chamber techniques [84] and Zeeman-slowing techniques [24, 23] currently used to capture atoms before evaporative cooling in a magnetic trap.

We performed this experiment before obtaining BEC, and the technique was not used in our initial BEC experiments. Our vacuum system was redesigned and rebuilt after completing this experiment. However, the results show how an interesting and little-known phenomenon can be used to increase the number of atoms loaded into a vapor cell MOT, with the main advantage of creating a more favorable situation for reaching BEC. The experiment also elucidates the main principles of concern in trying to reach BEC in a vapor cell, namely the tradeoff between atom number and trap lifetime.

Light-induced atom desorption (LIAD) has previously been used to obtain optically thick Na and Rb vapors in cells made of glass, pyrex, and sapphire [85, 86]. In most of these experiments, the inner walls of the vapor cells were coated with paraffin or silane in order to enhance the LIAD efficiency by reducing the alkali atom adsorption energy [87]. In our work, an optically thick vapor was not required. Since we did not need desorption rates characteristic of coated cells, we could desorb atoms directly from stainless steel.

## 5.2 Vapor cell magneto-optic traps

We first review the basic mechanisms involved in the operation of a vapor cell MOT, lucidly described in Ref. [40], in order to understand the gains available with the LIAD method. In a vapor cell MOT, atoms are loaded into the MOT at a rate  $R$ . This rate depends upon the size and intensity of the laser cooling and trapping beams and the Rb partial pressure. Atoms with velocities below a critical velocity will be captured by the trap. Atoms are also lost from the trap due to collisions with other atoms, limiting the number that can be loaded into the MOT. The rate equation for

the number,  $N$ , of trapped atoms is given by

$$\frac{dN}{dt} = R - N \left( \frac{1}{\tau_b} + \frac{1}{\tau_{\text{Rb}}} \right) - \beta \int n^2 dV, \quad (5.1)$$

where  $1/\tau_b$  is the trap loss rate due to collisions with background gas atoms and  $1/\tau_{\text{Rb}}$  is the loss rate determined by collisions with untrapped Rb atoms. The trap density,  $n$  in the volume integral, contributes to density-dependent losses within the trap with a loss coefficient of  $\beta$ . The loss rate  $1/\tau_b$  is proportional to the pressure of the background gas, and like  $R$ ,  $1/\tau_{\text{Rb}}$  is proportional to the Rb partial pressure. In the absence of density-dependent collisional losses ( $\beta = 0$ ) [14], and with a Rb partial pressure that is much higher than the background pressure ( $1/\tau_{\text{Rb}} \gg 1/\tau_b$ ), the rate equation becomes

$$\frac{dN}{dt} = R - \frac{N}{\tau_{\text{Rb}}}. \quad (5.2)$$

The limiting number,  $N_{\text{lim}}$ , that can be loaded into the MOT is obtained when the increase in number due to loading balances the loss due to collisions. At this point,  $N = N_{\text{lim}}$  and  $dN/dt = 0$ , yielding

$$N_{\text{lim}} = R\tau_{\text{Rb}}, \quad (5.3)$$

independent of the Rb partial pressure [40].

Frequently, the background-gas collisions can not be neglected, and the total number reached will be less than  $N_{\text{lim}}$ . The maximum number  $N_{\text{max}}$  that can be captured for a given Rb partial pressure will then be given by

$$N_{\text{max}} = N_{\text{lim}} \frac{\tau_{\text{MOT}}}{\tau_{\text{Rb}}} = R\tau_{\text{MOT}}, \quad (5.4)$$

where

$$\frac{1}{\tau_{\text{MOT}}} = \frac{1}{\tau_b} + \frac{1}{\tau_{\text{Rb}}}. \quad (5.5)$$

If the trap starts filling at time  $t = 0$ , the number of atoms in the MOT at any point in time is given by

$$N(t) = N_{\text{max}} \left[ 1 - \exp \left( -\frac{t}{\tau_{\text{MOT}}} \right) \right]. \quad (5.6)$$

Because of the appearance of  $\tau_{\text{MOT}}$  as the time constant in the exponential, we define  $\tau_{\text{MOT}}$  as the *MOT loading time constant*.

The lifetime of a *magnetic trap* in the same chamber also depends upon the collision rate of trapped atoms with background atoms. Thus the magnetic trap lifetime  $\tau$  is proportional to  $\tau_{\text{MOT}}$ . We express this proportionality as  $\tau = \tau_{\text{MOT}}/\alpha$ , where for our traps,  $\alpha \sim 4$ . For evaporative cooling experiments, where large numbers of atoms and long magnetic trap lifetimes are both necessary, the product of total number  $N_{\text{max}}$  and magnetic trap lifetime is the critical parameter to maximize [88]. Because of the relationship between  $\tau$  and  $\tau_{\text{MOT}}$ , we can alternatively view this requirement as maximizing the product of  $N_{\text{max}}$  and  $\tau_{\text{MOT}}$ , and we must then find the optimum Rb partial pressure for a given background pressure. Multiplying Eq. 5.4 by  $\tau_{\text{MOT}}$  leads us to maximization of  $\tau_{\text{MOT}}^2/\tau_{\text{b}}$  (remembering that  $N_{\text{lim}}$  is independent of vapor pressure). Under optimal conditions, with constant Rb partial pressure,  $N_{\text{max}}\tau_{\text{MOT}}$  is maximized for  $\tau_{\text{b}} = \tau_{\text{Rb}} = \tau_{\text{MOT}}/2$  and hence  $N_{\text{max}} = N_{\text{lim}}/2$  and  $N_{\text{max}}\tau_{\text{MOT}} = N_{\text{lim}}\tau_{\text{b}}/4$ .

However, we can further improve the number-lifetime product (which from now on we will generally designate as  $N\tau$ ) by permitting a modulation of the Rb vapor pressure. If the Rb partial pressure is *temporarily* increased until the trap contains the maximum possible number of atoms ( $N = N_{\text{max}} = N_{\text{lim}}$ ), at which point the Rb vapor is suddenly reduced to a negligible level ( $\tau_{\text{MOT}} \sim \tau_{\text{b}}$ ), an increase of a factor of 4 in  $N\tau$  will be realized. Furthermore, the time needed to load the MOT is significantly shortened when  $\tau_{\text{Rb}} \ll \tau_{\text{b}}$  during the loading interval, increasing the repetition rate of the experiment.

The goal of our experiment was to realize gains in  $N\tau$  by modulating the Rb vapor pressure in the described manner with the white light source, thus improving conditions for evaporative cooling and reaching the BEC threshold.

### 5.3 Experiment

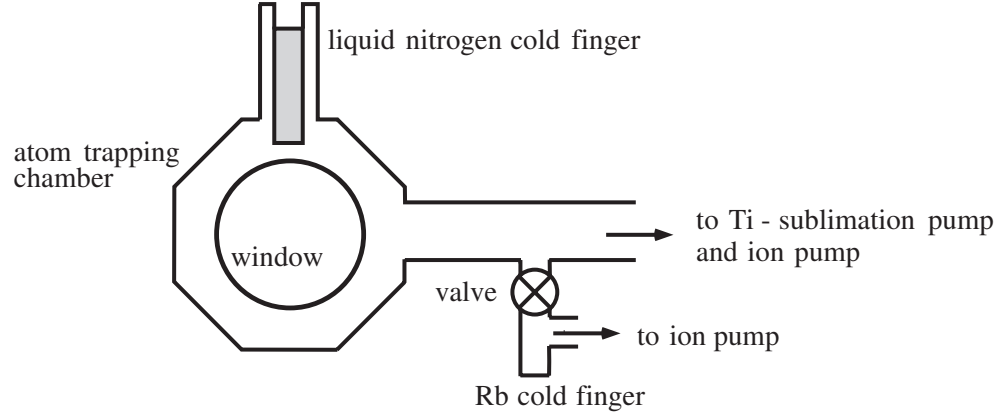


Figure 5.1: An illustration of our apparatus. The MOT was formed in the atom trapping chamber, and the WLS light entered into the chamber through a window.

### 5.3.1 Lasers

The lasers used in the experiment were Silicon Diode Labs diode lasers, with a specified output of 50 mW each. The lasers were operated in an external-cavity Littrow configuration, with a reflective grating acting as an output coupler. Two of the lasers were locked to Rb transitions using saturated absorption techniques; the third laser was injection locked with light from one of the grating-stabilized lasers. More details on the lasers and the laser lock are provided in Chapter 6.

### 5.3.2 Rb vapor cell

Our stainless steel vacuum chamber consisted of a vapor cell atom trapping chamber with indium-sealed windows, a liquid nitrogen-filled cold finger which protruded into the chamber, and a Rb cold finger at 0°C, as shown in Fig. 5.1. The vacuum in the chamber was maintained by a Ti-sublimation pump and an ion pump. We maintained a Rb vapor in the chamber by occasionally opening a valve between the chamber and a Rb cold finger. This replenished Rb that had been pumped out of the chamber.

### 5.3.3 Light-assisted losses

The analysis of section 5.2 assumed that  $\beta$  in Eq. 5.2 (the light-assisted, density-dependent loss coefficient) was zero. In practice, these light-assisted losses limit the number of atoms loaded into a bright MOT. One solution to this problem, first demonstrated by Ketterle *et al.* with sodium [71], was the dark spontaneous-force optical trap (SPOT) technique. In this scheme, resonant laser light is eliminated from the center of the MOT trapping beams, but light at the edges of the trap continues to capture and cool atoms. The atoms are pushed towards the center of the trap, where they are optically pumped into a dark ground state (for us, this was the  $F = 1$  level) and refrain from scattering light from the trapping beams. Consequently, this is referred to as a *dark* MOT, or dark SPOT.

The dark MOT is created by eliminating the central area of the repumping light, leaving the molasses beams intact. The trapping light at the center of the trap thus pumps atoms out of the bright state. This method was further modified by Anderson *et al.* at JILA for Rb [88]. In rubidium, the probability of excited state decay into the upper ground state compared to the lower ground state is much higher than for sodium. For this reason, the JILA group used an additional optical pumping beam to force the trapped atoms into the dark state.

### 5.3.4 The Rb MOT

Our MOT was constructed using a forced dark SPOT technique [71, 88]: a 4-mm opaque spot was placed in the center of the path of the repumping laser light, and was imaged onto the region in the chamber where the trap was formed. Another laser beam filled the hole in the repumping beam, and was used to optically pump trapped atoms into a dark state. This technique reduced the trap loss rate due to light assisted, density-dependent collisions between trapped atoms. The Rb trapping light was tuned 13 MHz below the  $5S_{1/2}, F = 2 \rightarrow 5P_{3/2}, F' = 3$  transition, and was provided by six 23-mW/cm<sup>2</sup>, 1.2-cm diameter laser beams (see Appendix A for the <sup>87</sup>Rb energy level structure). The 2.7-mW/cm<sup>2</sup> repumping laser beam was tuned 15 MHz below the  $F = 1 \rightarrow F' = 2$  transition, and the 9-mW/cm<sup>2</sup> forced optical

pumping light was tuned to the  $F = 2 \rightarrow F' = 2$  transition. The number of atoms in the trap was measured by detecting light scattered by the trapped atoms. This was done by turning off the  $F = 2 \rightarrow F' = 2$  light for  $\sim 50$  ms and filling the hole in the repumping beam with a separate bypass repumping beam such that the trapped atoms were made bright by scattering light from the trapping beams. A fraction of the light scattered by the trapped atoms was collected and focused onto a calibrated photomultiplier tube. Loading rates ( $R$ ) and MOT loading time constants ( $\tau_{\text{MOT}}$ ) were measured by detecting the number of atoms at sequential points in time as the trap filled.

### 5.3.5 White light source

The white light used to enhance trap loading was provided by a fiber optic illuminator, consisting of a halogen bulb with variable power and a fiber bundle which pointed the light into the vapor cell. The coupling of the light from the bulb into the fiber gave a maximum intensity onto the inner vapor cell wall of  $\sim 10$  W/cm<sup>2</sup>. The WLS was switched on and off electronically.

### 5.3.6 Measurements

To measure  $\tau_{\text{MOT}}$ , we measured the number of atoms loaded into the trap as a function of time both with and without the WLS. The loading curves were exponential in time, as expected for a trap without light-assisted losses. Typical filling curves are shown in Fig. 5.2(a) for various WLS intensities. In the figure, the curve representing the fastest filling rate, with a WLS intensity of  $\sim 10$  W/cm<sup>2</sup>, shows a loading time constant of  $\tau_{\text{MOT}} = 67$  s and a maximum number of  $\sim 1.3 \times 10^8$  atoms as determined by the exponential fit. Without the WLS, the loading time constant was  $\tau_{\text{MOT}} = 538$  s and the maximum number was  $\sim 2 \times 10^7$  atoms. Values of number loaded and loading time constants for the curves shown in Fig. 5.2(a) are given in the second and third columns of table 5.1.

A key factor to consider in optimizing  $N\tau$  using the WLS scheme is the time for the vapor pressure to return to lower equilibrium values once the WLS is switched off.

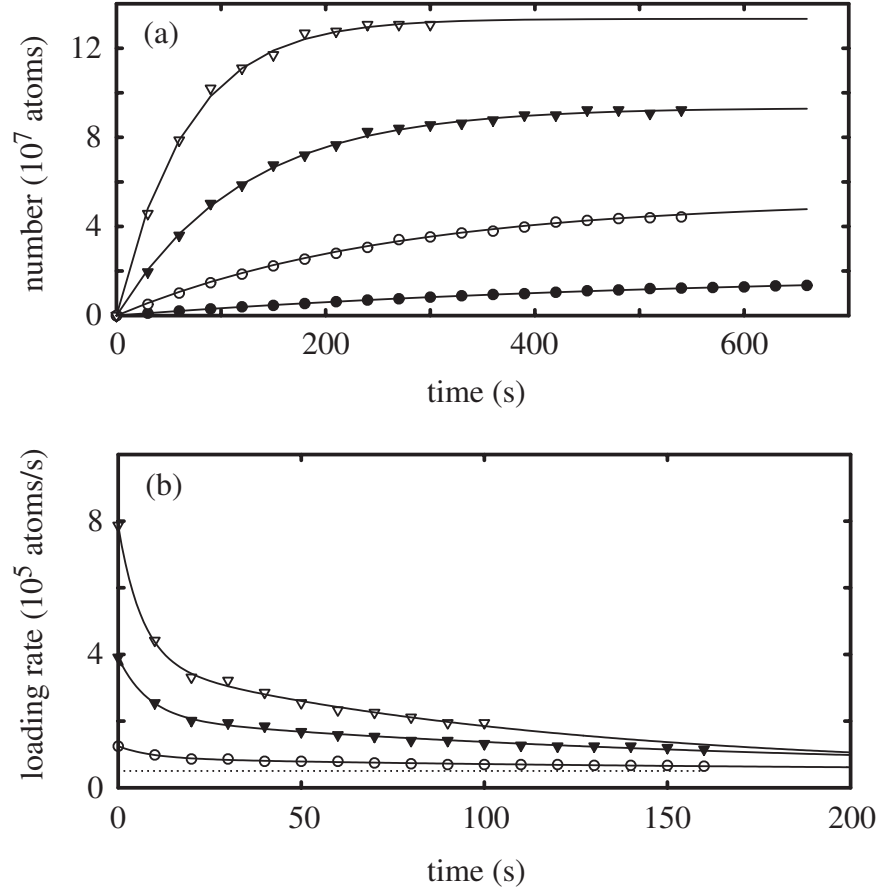


Figure 5.2: (a) Comparison of trap loading with and without the additional external white light source. (b) Trend of the loading rate as a function of time after the WLS is turned off. The lower dashed line shows the loading rate before the WLS was turned on. For both (a) and (b), open triangles represent a WLS intensity of  $\sim 10$  W/cm $^2$ , closed triangles represent a WLS intensity of  $\sim 5$  W/cm $^2$ , and the open circles represent a WLS intensity of  $\sim 2$  W/cm $^2$ . The closed circles in (a) represent loading without the WLS. See Table 5.1 for numerical results of the data shown in these plots.

WLS intensity (W/cm <sup>2</sup> )	$N_0$ (10 <sup>7</sup> atoms)	$\tau_{\text{MOT}}$ (s)	$\tau_{\text{rec},1}$ (s)	$\tau_{\text{rec},2}$ (s)
10	13.3	67	6.5	113
5	9.3	120	8.2	167
2	5.2	267	9	162
0	1.9	538	—	—

Table 5.1: Loading and recovery characteristics of the MOT for various WLS strengths.  $N_{\text{max}}$  indicates the maximum number of atoms that can be loaded into the trap for the corresponding Rb partial pressure. The MOT loading time constant is given by  $\tau_{\text{MOT}}$  and the fast recovery time constant is listed as  $\tau_{\text{rec},1}$ . The time  $\tau_{\text{rec},2}$  is the longer time constant in the exponential fits to the data shown in Fig. 5.2(b).

We define this time as the vapor pressure recovery time. A liquid nitrogen cold finger in the main chamber was used to decrease the Rb vapor pressure and shorten the recovery time after the WLS was switched off. In our cell, the cold finger had little effect on the background gas pressure, but shortened the recovery time by a factor of  $\sim 2$ . Furthermore, our experimental timing sequence consisted of a MOT loading phase with the WLS switched on, followed by a MOT holding phase, during which the atoms were held in a MOT with the WLS switched off. This enabled us to keep a large number of atoms trapped while waiting for the vapor pressure to decrease before extinguishing the trapping light.

In order to evaluate vapor pressure recovery times, we measured loading rates (proportional to the vapor pressure) as a function of time just after the WLS was switched off. For the data shown in Fig. 5.2(b), the WLS was left on until the Rb partial pressure reached a saturated level. The WLS light was then turned off, and the number of atoms loaded into a MOT in 5 seconds was repeatedly measured. After each measurement, the MOT light was kept off for 5 s, and then the MOT started filling again for the subsequent 5 s filling rate measurement. This set of measurements indicated the speed at which  $\tau_{\text{MOT}}$  and the Rb vapor pressure could recover after the WLS was turned off, and demonstrated that the recovery time was roughly independent of the WLS intensity. The fastest loading rate shown with the WLS on was  $\sim 8 \times 10^5$  atoms/s, and with the light off was  $\sim 2.7 \times 10^4$  atoms/s. Each loading



rate *vs.* time curve in Fig. 5.2(b) was fit with a sum of two decaying exponential curves. The time constants for the loading rate to return to lower equilibrium values were  $\sim 8$  s for the fast recovery time ( $\tau_{rec,1}$ ), and between 113 s and 167 s for the slower recovery time ( $\tau_{rec,2}$ ). Table 5.1 contains a list of recovery times.

To help evaluate the vapor cell performance, the values for  $N_{lim}$  and  $\tau_b$  were estimated by measuring  $N$  and  $\tau_{MOT}$  for various Rb partial pressures. Experimentally, we varied the Rb partial pressure by adjusting the intensity of the WLS. We estimated  $\tau_b \sim 700$  s and  $N_{lim} = 1.9 \times 10^8$  atoms for our operating parameters.

## 5.4 Modeling the effects of the white light source

We now describe a detailed model for determining the number and lifetime of traps loaded with the WLS to demonstrate the possibility of increasing  $N\tau$  under realistic experimental conditions. Specifically, this model includes the effects of finite vapor pressure recovery times and finite loading times. Without the use of the WLS, and with long loading times,  $N\tau$  in a magnetic trap can obtain a maximum optimal value of

$$(N\tau)_{opt} \equiv N_{lim}\tau_b/4\alpha \quad (5.7)$$

with  $\tau_{Rb} = \tau_b$ . We will compare the performance of a WLS-loaded MOT to  $(N\tau)_{opt}$  to demonstrate the effectiveness of a WLS-loaded MOT.

For a trap loaded with the WLS, calculating  $N\tau$  is more complicated. We divide the experimental cycle into three time periods. During the first period, the MOT is loaded, and the WLS remains on for the duration of this period. We call this period the *MOT loading phase*, which has a duration of time  $t_1$ . The cycle then enters the *MOT holding phase*, which has a duration of time  $t_2$ . In the holding phase, the WLS remains off, allowing the vapor pressure to recover while continuing to hold a large fraction of the trapped atoms in the MOT. In the third period of the cycle, the MOT beams are also turned off and the atoms are trapped in a magnetic trap. This period begins at time  $t_T = t_1 + t_2$ .

Variables for the number of atoms in the trap can be defined at the boundaries

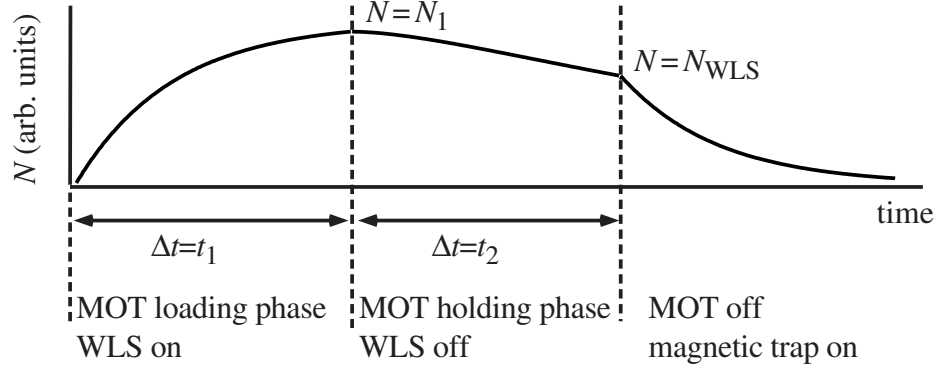


Figure 5.3: The timing sequence used in the experiment and in the calculations. The plot is a representation of the number of trapped atoms as a function of time. The dashed lines separate the different stages of trap loading and holding. The number of trapped atoms at the end of the MOT loading and holding phases is given above the  $N$  vs. time curve. The states of the MOT and the WLS are also listed for the time intervals  $t_1$  and  $t_2$ . After the MOT holding phase, at time  $t_T = t_1 + t_2$ ,  $N_{\text{WLS}}$  atoms are assumed to be loaded from the MOT into a magnetic trap.

of the time periods. At the beginning of the loading phase,  $N = 0$ . By the end of the loading phase at time  $t_1$ ,  $N_1$  atoms are in the MOT. The cycle then enters the holding phase, during which some atoms are lost from the trap due to a decreasing Rb partial pressure. We define  $N_{\text{WLS}}$  to be the number of trapped atoms remaining at the end of this period. The “WLS” subscript emphasizes that this number was obtained using the WLS. The cycle then enters the magnetic trap phase, and  $N_{\text{WLS}}$  atoms are loaded into the magnetic trap. Because of the continually decreasing vapor pressure (from having used the WLS), the number of atoms in the magnetic trap decays faster than exponentially. Since we desire to maximize the number-lifetime product for the magnetic trap, we define an *effective lifetime*  $\tau_{\text{WLS}}$  as the time at which the number of atoms in the magnetic trap has reached  $(1/e)N_{\text{WLS}}$ . The entire cycle as described is illustrated in Fig. 5.3.

Our intent in this analysis is to compare  $N_{\text{WLS}}\tau_{\text{WLS}}$  with both  $N\tau$  for unmodulated Rb pressures at varying loading times and with  $(N\tau)_{\text{opt}}$ , as defined in Eq. 5.7. First,

we calculate the number of atoms  $N_1$  in the MOT at  $t_1$ . At the beginning of the MOT loading phase, the WLS is turned on, and the loading time constant associated with the Rb partial pressure quickly drops to a value of  $\tau_1$ . We thus obtain

$$N_1 = \frac{N_{\text{lim}}}{1 + \tau_1/\tau_b} [1 - \exp(-t_1 [1/\tau_1 + 1/\tau_b])] \quad (5.8)$$

from the use of Eqs. 5.6 and 5.4.

We then enter the holding phase. The WLS is turned off, and the number of atoms in the MOT is governed by the rate equation  $dN/dt = R(t) - N/\tau_2(t) - N/\tau_b$ , where  $\tau_2$  is the loading time constant associated with the decaying Rb vapor pressure. The time dependence of  $R$  and  $\tau_2$  is made explicit, since these values depend upon the decreasing Rb vapor pressure. The loading rate  $R(t)$  and the loss rate  $1/\tau_2(t)$  are assumed to decay exponentially (with a time constant of the vapor pressure recovery time) to the steady-state values  $R(t) \rightarrow 0$  and  $1/\tau_2(t) \rightarrow 0$  (negligible Rb vapor pressures) as the vapor pressure recovers. The rate equation is numerically integrated to determine the number of atoms,  $N_{\text{WLS}}$ , left in the MOT at time  $t_T$ , the point at which the MOT is turned off.

We finally enter the magnetic trap phase of the cycle, where we must determine the effective magnetic trap lifetime  $\tau_{\text{WLS}}$  by numerically solving the rate equation  $dN/dt = -\alpha \cdot (N/\tau_3(t) - N/\tau_b)$ . Here,  $1/\tau_3(t)$  has an initial value of  $1/\tau_2(t_2)$  and decays exponentially in time to 0 as the vapor pressure continues to recover. Finally, we can write the number-lifetime product of the WLS-loaded MOT, designated by  $(N\tau)_{\text{WLS}}$ , as  $(N\tau)_{\text{WLS}} = N_{\text{WLS}}\tau_{\text{WLS}}$ .

We numerically investigated the performance of the MOT loaded with the WLS by comparing  $(N\tau)_{\text{WLS}}$  with  $N\tau$  for unmodulated pressures (Fig. 5.4). Figure 5.4(a) shows the number-lifetime product due to trapping atoms in a MOT for a time  $t_T = \tau_b$  as a function of the fraction of the loading cycle that the WLS is used. We assume that  $N_{\text{max}} = N_{\text{lim}}/2$  for unmodulated partial pressures, and an arbitrary value of  $N_{\text{max}} = N_{\text{lim}}/(1 + \tau_1/\tau_b) = (0.9)N_{\text{lim}}$  (see Eq. 5.8), or equivalently  $\tau_1 = (0.1)\tau_b$ , for the modulated partial pressures. Here, the chosen value of  $N_{\text{max}}$  can not be set to  $N_{\text{lim}}$  due to limitations in the numerical calculations. Fig. 5.4(b) shows the same

conditions as Fig. 5.4(a), but here we have plotted the ratio of  $(N\tau)_{\text{WLS}}$  to  $N\tau$  with unmodulated pressures after a total MOT trapping time of  $t_{\text{T}} = \tau_{\text{b}}$ . Figures 5.4(c,d) illustrate the enhancements due to WLS-loading for a total loading time of  $t_{\text{T}} = 2\tau_{\text{b}}$ .

The optimum time to leave on the WLS is determined by the maximum point of a given curve. In the calculations, the gain in  $N\tau$  after using the WLS is less than the maximum possible value of 4 due to the need to allow the vapor pressure to recover before loading into a magnetic trap. The highest values that can be achieved for  $N\tau$  with and without the WLS are plotted against total loading time  $t_{\text{T}}$  in Fig. 5.5 for the same conditions as in Fig. 5.4. The gain in using the WLS is again less than the ideal maximum factor of 4 for long loading times. However, for short loading times,  $N\tau$  for unmodulated pressures is much lower than  $(N\tau)_{\text{opt}}$  as demonstrated by the gray curve in Fig. 5.5(a), so modulated vapor pressures can give substantial benefits in this regime. This is shown by the larger  $N\tau$  ratios in Fig. 5.5(b).

As a concrete example of interpreting the plots given here, we assume that we have a system that has a vapor pressure recovery time of  $0.10\tau_{\text{b}}$ . Thus we are concerned with the top curves in Figs. 5.4(a-d) and 5.5(a,b). If we load the vapor cell MOT without modulating the Rb partial pressure, we can achieve a value of  $N\tau \sim 1$  (in units of  $(N\tau)_{\text{opt}} \equiv N_{\text{lim}}\tau_{\text{b}}/4\alpha$ ) after loading the trap for a total time of  $t_{\text{T}} = 2\tau_{\text{b}}$ , as shown in the lower curve of Fig. 5.5(a). However, if we modulate the Rb pressure with the WLS, we can triple the value of  $N\tau$  for the same total MOT trapping time. To determine the proper time to remove the WLS light, Fig. 5.4(c) indicates beginning the MOT holding phase at an optimum time of  $\sim 0.3\tau_{\text{b}}$  before loading the magnetic trap. Alternatively, we can shorten the loading time to  $\sim 0.5\tau_{\text{b}}$ , as demonstrated in Fig. 5.5(a), and maintain the same gain in  $N\tau$ . In doing so, we would not only gain a factor of 3 in  $N\tau$ , but we would also increase the repetition rate of the experiment by as much as a factor of 4. If instead we load the experiment for a fixed amount of time in either case (with or without the WLS), we should look at Fig. 5.5(b) to compare the  $N\tau$  products. For a total MOT trapping time of  $t_{\text{T}} = 0.4\tau_{\text{b}}$ , we would achieve over a five-fold gain in  $N\tau$  by modulating the WLS.

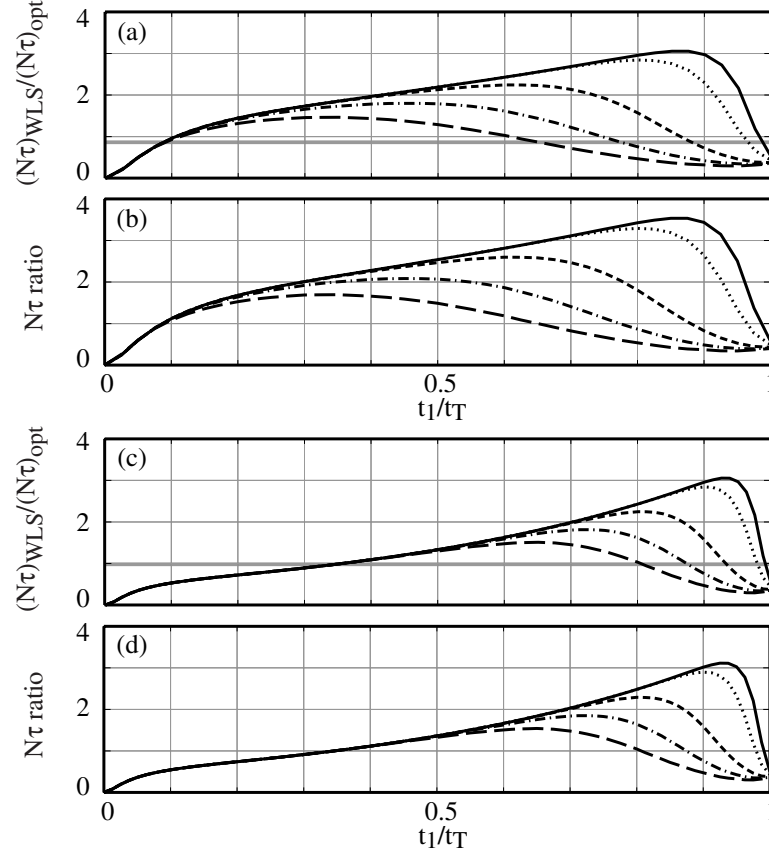


Figure 5.4: (a) The calculated products  $(N\tau)_{\text{WLS}}/(N\tau)_{\text{opt}}$ , after a total MOT trapping time of  $t_T = \tau_b$ . The Rb-limited lifetime is assumed to quickly decrease to  $\tau_1 = \tau_b/10$  when the WLS is turned on. The curves show  $(N\tau)_{\text{WLS}}$  at varying times  $t_1$  (as a fraction of  $t_T$ ), the point in the MOT loading cycle at which the WLS is turned off, with the remaining time in the cycle ( $t_T - t_1$ ) permitting recovery of the Rb partial pressure with a time constant of  $0.035\tau_b$  (black line),  $0.05\tau_b$  (dotted),  $0.1\tau_b$  (short dashed),  $0.15\tau_b$  (dashed-dotted), and  $0.2\tau_b$  (long dashed).  $N\tau$  for unmodulated vapor pressure is shown as a solid gray line, after a loading time of  $\tau_T = \tau_b$ . (b) The ratios of the upper curves in (a) to the value of  $N\tau$  for unmodulated vapor pressure after a MOT trapping time of  $\tau_T = \tau_b$ . (c,d) Same as for (a) and (b), with a total loading time of  $t_T = 2\tau_b$ . These plots demonstrate that for a given recovery time and MOT trapping time ( $t_T$ ), there is an optimal WLS duration ( $t_1$ ) the maximum point on the plotted curves.

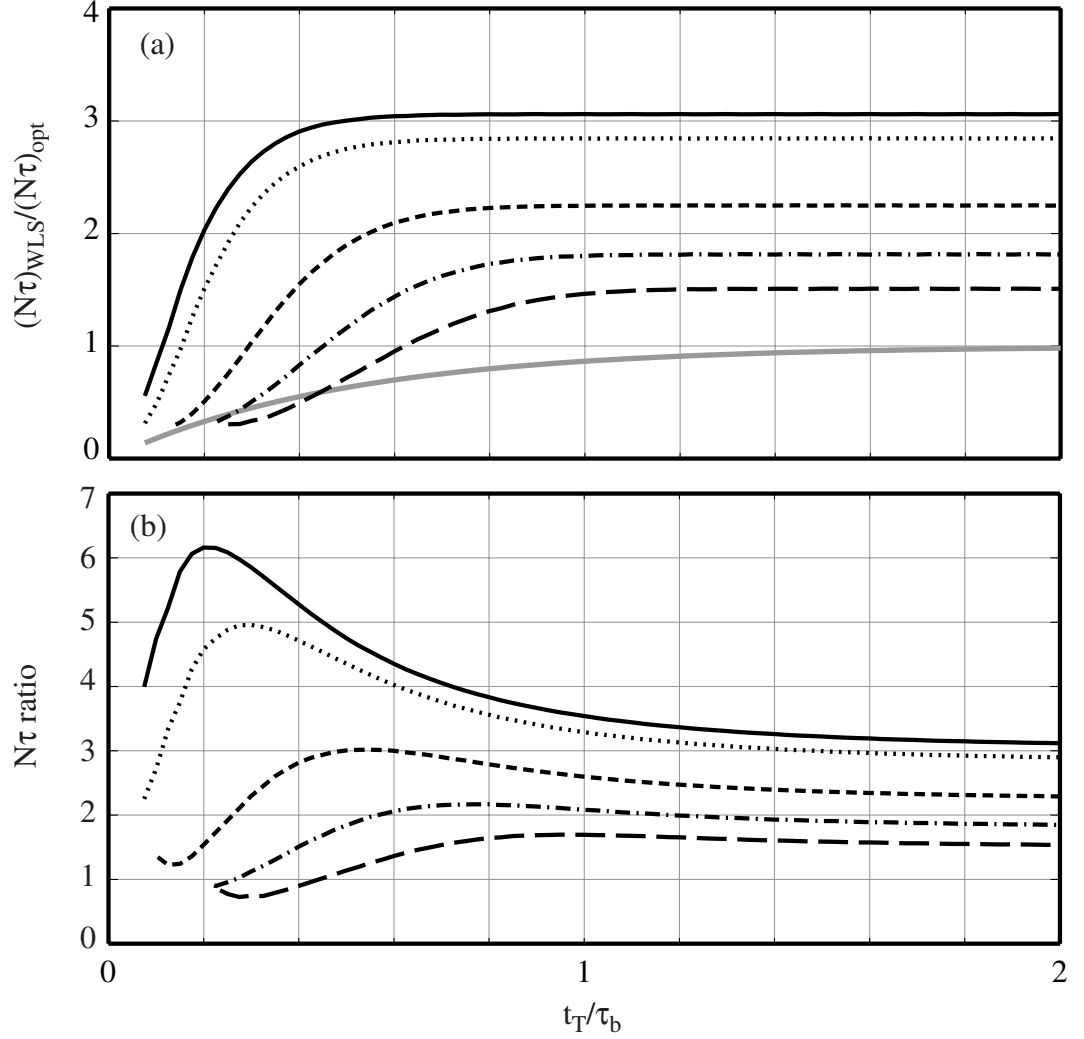


Figure 5.5: (a) Values of  $(N\tau)_{\text{WLS}}$  for WLS loading as a function of  $t_T$  (as a fraction of  $\tau_b$ ). The limiting number of atoms that can possibly be loaded into the WLS trap is assumed to be  $(0.9)N_{\text{lim}}$  (top curves), or equivalently  $\tau_1 = \tau_b/10$  when the WLS is turned on. The curves represent recovery times  $0.035\tau_b$  (black line),  $0.05\tau_b$  (dotted),  $0.1\tau_b$  (short dashed),  $0.15\tau_b$  (dashed-dotted), and  $0.2\tau_b$  (long dashed). The variation of the non-WLS-loaded number-lifetime product with time (solid gray line) is shown. The calculations assume that for any particular value of  $t_T$ , the WLS is turned off at the optimal  $t_1$  (see Fig. 5.4). The vertical axis is scaled to  $(N\tau)_{\text{opt}}$ . (b) The ratios of the upper curves in (a) to the value of  $N\tau$  for unmodulated vapor pressure at any given total MOT trapping time  $t_T$ .

## 5.5 Assessing the gains of LIAD

### 5.5.1 Observations

Experimentally, we were able to obtain an increase in  $N\tau$  of a factor of  $\sim 2.2$  using the WLS technique. This was achieved with a MOT loading phase of duration  $t_1 = 100$  s and a MOT holding phase of duration  $t_2 = 50$  s compared to a total loading time of 470 s without the WLS. Note that in addition to the gain in  $N\tau$ , the total MOT loading time with the WLS was 3.1 times faster than without the WLS, tripling the repetition rate of experiments. The WLS experimental technique would be even more beneficial by shortening the recovery time of the vapor pressure. This might be accomplished by keeping a larger fraction of the inner surface of the vapor cell at cryogenic temperatures or through optimization of the surface adsorption chemistry.

### 5.5.2 Extension of the technique to other atomic species

The use of LIAD to enhance loading of vapor cell MOTs may be applicable to other atomic species. Lithium vapor cells, for instance, are difficult to work with due to the high temperatures needed to create a substantial Li vapor. Yet if LIAD were to work well with Li adsorbed on stainless steel, or between co-adsorbed Li atoms on a surface, a Li vapor cell MOT would be practical. Although the effect has not yet been quantitatively explored as it has been for Rb, we observed a LIAD induced increase in the loading rate into a cesium MOT in a Cs vapor cell with aluminum walls.

### 5.5.3 Caution

Caution is necessary when using this technique with light intensities that are substantially higher (more than an order of magnitude) than the levels given here. In exploring the effects of white light on the loading rates, we tried using a high-intensity arc lamp for atom desorption. The light from the lamp was directed into the chamber for  $\sim 5$  seconds. The light did not thermally heat up the chamber in this amount of time. However, the LIAD effect was extremely quick, producing a partial pressure so high that we had the unfortunate experience of finding visible clusters of atoms

re-adsorbed onto the inner surfaces of the windows of our vacuum chamber. This drastically reduced the quality of our windows to the point where they were no longer usable.

To recover from this problem, we built a new vacuum chamber. The new system did not reveal LIAD effects for many months, during which time a Rb layer very slowly built up on the inner chamber walls. This aspect is discussed at the end of Chapter 6 in section 6.9. After two years of working with the newer system, however, enough Rb had accumulated on the walls that the LIAD effect was very strong and beneficial in enhancing our BEC creation technique.

## 5.6 Summary

In summary, we demonstrated that non-thermal light-induced atom desorption can be used to effectively increase the number of atoms that can be loaded into a vapor cell MOT. This technique benefits atom trapping experiments where large numbers of atoms and long trap lifetimes are crucial.



# Chapter 6

## Bose-Einstein condensation of $^{87}\text{Rb}$

### 6.1 Motivation

The original ground-breaking achievements of Bose-Einstein condensation (BEC) in dilute atomic vapors have enabled new tests of theory for weakly interacting degenerate Bose gases [22, 23, 24]. Since these achievements were announced, many theoretical studies have been published regarding various aspects of BEC offering complementary support to experimental efforts and providing motivation for further research. Most experimental studies such as measurements of condensate fraction and the mean-field interaction energy [89, 90] have been based on momentum distribution measurements extracted from images of initially condensed samples following an interval of free-space ballistic expansion.

In this chapter, we discuss complementary measurements of BEC characteristics based on quantitative analysis of direct images of a  $^{87}\text{Rb}$  condensate. Our measurements were made in a regime where the number of condensed atoms was small enough that the kinetic energy of the trapped atoms could not be ignored in comparison with the mean-field interaction energy. We have also explored various *in situ* imaging techniques at the resolution limits of our imaging system in order to image low-number condensates.

## 6.2 Experimental approach to BEC

Our experimental approach to BEC production paralleled that of the first JILA experiment [22]. In our experiment, atoms were initially captured from a dilute Rb vapor into a MOT [7] operating in a modified dark-spot configuration [71, 88]. Atoms were subsequently compressed [91] and cooled, optically pumped into the  $F = 2, m_F = 2$  state, then loaded into a purely magnetic TOP trap [47]. Atoms were further compressed by changing the TOP field parameters, and then evaporatively cooled [35] to condensation. The condensates and thermal clouds were imaged using absorptive and dark-ground [92] techniques.

Our approach deviated from prior work in the following respects. First, we achieved a performance enhancement during the MOT loading period by capturing atoms into a hybrid trap consisting of a MOT plus a weak rotating magnetic bias field. Second, the bulk of the evaporation was done by reducing the strength of the rotating component of the TOP magnetic field, while maintaining a fixed quadrupole field gradient, rather than by rf-induced evaporation. Third, we carefully tailored the TOP-induced evaporation sequence through a piecewise optimization of evaporation parameters. This allowed us to obtain efficient evaporation with relatively small numbers of atoms. Finally, we directly imaged the trap with an  $f/2.5$  optical system through high quality optical viewports, allowing comparison of characteristics of low-number condensates in the TOP trap with theory.

## 6.3 Apparatus

### 6.3.1 Lasers

To cool, trap, and image the Rb atoms, we used three 780-nm Silicon Diode Labs diode lasers which could operate at continuous power levels up to  $\sim 80$  mW. The lasers were mounted in homemade temperature-stabilized aluminum housings, with a window in each housing to permit the laser light to escape. Two of the diodes were installed in an external-cavity Littrow configuration: the highly divergent light emitted from the laser was first collimated, and a reflective grating was used as an

output coupler to reflect a portion of the light back onto the diode, inducing gain in the cavity at the frequency of the reflected light. Because this frequency was determined by the angle of incidence of the light on the grating, the laser frequency was coarsely tuned by adjusting the grating angle.

The lasers were further temperature-stabilized by mounting each laser in direct thermal contact with a thermo-electric cooler maintained at temperatures close to room temperature. In order to operate the lasers in a single mode and lock the frequency to a Rb optical transition, we used a standard saturated absorption technique for the two grating-stabilized lasers. By frequency modulating the laser light and detecting the modulated levels of laser absorption after passing through a Rb vapor cell, we locked the frequencies of the lasers with a lock-in detection method.

The third laser in our setup was injection locked. Instead of using light reflected from a grating to induce laser amplification, a small portion of seed light (typically less than 1 mW) from one of the grating-stabilized lasers was directed into the trapping laser, inducing amplification at the frequency of the injected light.

In order to adjust the laser frequencies and enable active control of the frequencies while operating the experiment, we used the frequency shifts available with standard acousto-optic modulators (AOMs). The AOMs were also useful in quickly modulating the amplitude of the light for the experiment. However, because of the sensitivity of evaporative cooling to stray light (which can cause heating), we also used mechanical shutters in the beam paths to completely extinguish the light during the magnetic trapping phase of the experiment.

### 6.3.2 Vacuum system

The vacuum chamber consisted of the atom trapping chamber, the vacuum pumps, and a Rb source. The atom trapping chamber was a 2.5-cm thick stainless steel octagon, electropolished to reduce the surface area within the chamber. The chamber had viewport holes in six of the eight  $\sim 4.2$ -cm long sides, and on the top and bottom. One-inch diameter anti-reflection coated optical viewports were attached over the holes in the sides, with 2-inch diameter viewports on the top and bottom. A seventh

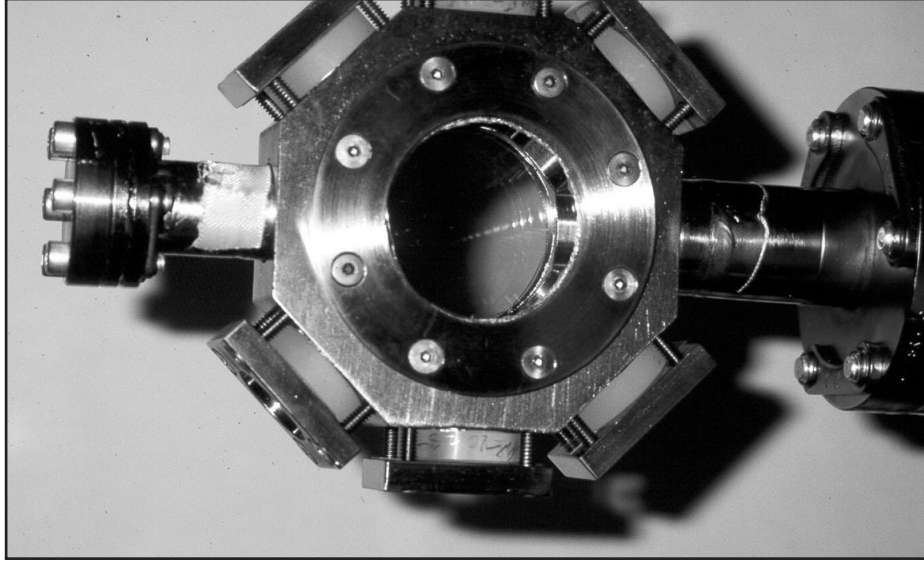


Figure 6.1: A top view of the Rb atom trapping chamber

side was sealed with a blank stainless steel flange, and the eighth side was attached to the vacuum pump section of the chamber.

The viewports, used to admit the laser light for imaging the condensate and for the laser cooling and trapping, were vacuum-sealed to the chamber with indium, a soft metal with a low vapor pressure. To seal a window to the chamber, a clean loop of  $\sim 1$  or  $2$  mm diameter indium wire was placed between the chamber and the window. A flange, which screwed directly into the chamber around the window, was then placed on top of each window (separated from the window by a thin piece of mylar to relieve window stress). When the flange was slowly tightened, the pressure of the flange on the window caused the indium to flatten and seal the gap between the window and the chamber. A top view of the chamber with windows attached is shown in Fig. 6.1.

Indium seals have many benefits. First, the seals are inexpensive and convenient to use for simple custom-built vacuum chambers and for small systems with small windows. One major advantage of the seals is the ability to attach high quality optics to the chamber, without relying on commercially available vacuum viewports,

typically of much lower quality than other available optics. Indium seals can also be used reliably for very low pressures. Our system has obtained pressures in the  $10^{-12}$  torr range, inferred from MOT loading time measurements.

Indium seals also have drawbacks. For large windows, the probability of cracking a window while increasing the flange pressure to form the seal can be a problem (this was not the case with our 1 and 2-inch diameter, 1/4 and 3/8-inch thick windows). The main drawback, however, is a low melting point of  $157^\circ\text{C}$  for indium. When our vacuum system was initially baked out, the trapping chamber had to remain at temperatures lower than desired. The vacuum chamber thus could not often be opened since long times were needed to reach low background pressures. For these reasons, it was helpful to have a small chamber with low surface area.

The system was pumped with a Varian 20-l/s ion pump and a Ti-sublimation pump. The pumps were attached to the main trapping chamber with a 6-way cross. A Rb partial pressure was maintained in the main chamber with a Rb coated cold finger, also attached to the 6-way cross on the port opposite the main chamber. A valve between the cross and the cold finger regulated the Rb flux into the chamber. The cold finger was typically operated at room temperature, where the ratio of Rb to background gas was highest (without additional heating). The picture of the vacuum chamber shown in Fig. 6.2, taken during the move from Stanford to Yale, shows the sections of the chamber.

### 6.3.3 DC magnetic-field bias coils

The magnets used on the ion pump created a bias magnetic field of  $\sim 1.5$  G at the center of the trapping chamber. The field due to the earth was  $\sim 0.5$  G. In order to eliminate these and other weaker stray magnetic fields, we used three pairs of Helmholtz-configured coils to zero the magnetic field at the chamber center. Unwanted magnetic fields were cancelled by adjusting the currents in each bias coil.

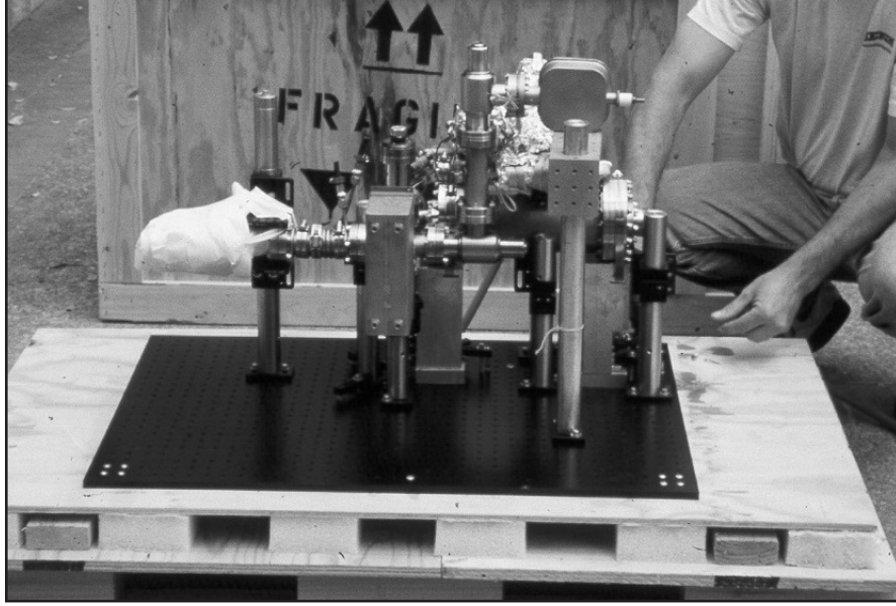


Figure 6.2: The vacuum chamber, before being loaded into a crate for transportation. The atom trapping chamber is shown here covered in protective padding.

#### 6.3.4 Spherical-quadrupole field coils

The two spherical-quadrupole magnetic field coils that produced the field gradient for the MOT and the magnetic trap were created from insulated copper tubing with a  $0.25 \text{ inch} \times 0.25 \text{ inch}$  square cross section. To dissipate the heat produced by the coils while they were in operation, we cooled the coils by pumping water through the tubing. Each cylindrically symmetric coil was wound with a radial depth of 8 turns and a cylindrical height of 20 layers. The inner diameters of the coils were 4.5 cm. High temperature epoxy was applied in order to maintain the shape of each of the coils.

The coils were mounted with their symmetry axis parallel to gravity, one above the trapping chamber and one below, with  $\sim 3 \text{ cm}$  between the center of the chamber and the inner layer of each coil. We were able to achieve linear magnetic field gradients of  $750 \text{ G/cm}$  in the axial (vertical) direction by running  $350 \text{ A}$  through the coils, supplied by a  $40 \text{ V}$ ,  $350 \text{ A}$  EMI power supply.

We used a high-current MOSFET circuit to switch off the current in the magnets. Two MOSFETs were connected in parallel, and inserted in series with the coils. In order to quench damaging voltage spikes ( $> 100$  V) across the MOSFETs when turning off the current, we placed an 80 V Zener diode array across the MOSFET terminals, providing protection by conducting at voltage levels higher than 80 V. The time to switch off the circuit at 30 A was  $\sim 0.5$  ms.

In order to efficiently load atoms into a magnetic trap, the magnets also had to be turned on quickly. The inductance,  $L$ , of the coils limited the turn-on time to  $\sim 20$  ms when the MOSFET circuit was simply closed. We built an additional circuit to circumvent this limitation. This second circuit consisted of a 1000 V capacitor, with a capacitance of  $C = 15 \mu\text{F}$ , connected across the magnetic field coils. A silicon-controlled rectifier (SCR) was inserted into the loop formed by the capacitor and the coils, and was normally non-conducting. A separate high-voltage, low-current power supply and resistor were used to slowly charge up the capacitor to  $\sim 740$  V in 30 s during the MOT loading period. Just before transferring the atoms into the magnetic trap, the magnetic field was switched off (see below for the experimental sequence), and the MOSFETs were non-conducting. To turn on the spherical-quadrupole coils quickly, a TTL signal (4 V or 0 V, representing on or off logic states) was sent to an opto-isolator which turned on the SCR, closing the coil-capacitor loop. Simultaneously, the MOSFETs were returned to the conducting state. The capacitance  $C$  was chosen so that the  $LC$  time constant of the capacitor and coils had an oscillation period of  $\sim 1$  ms. When the switch was opened, the energy stored in the capacitor was resonantly transferred into the coils in times of  $\sim 0.5$  ms, as expected from the time constant. The SCR then returned to its non-conducting state and the conducting MOSFETs enabled the main power supply to drive the desired current through the coils (the maximum current in the coils supplied by the capacitor matched the driving current from the power supply). With this configuration, we achieved a switch-on time for the magnets of  $\sim 0.5$  ms at currents of  $\sim 65$  A. A circuit diagram for the coils and switching circuits is shown in Fig. 6.3.



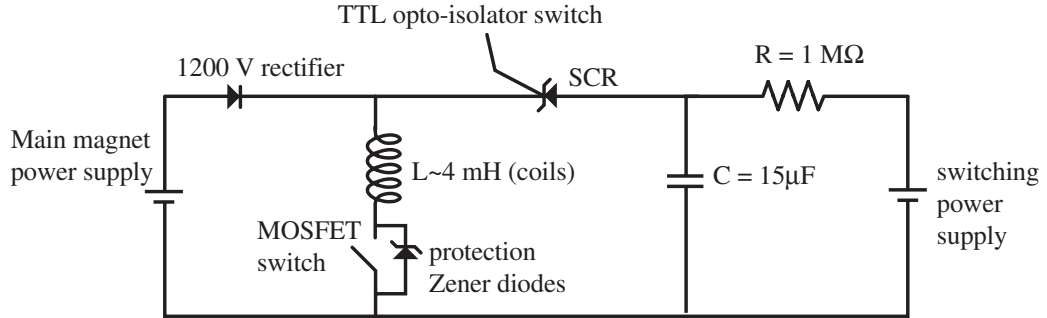


Figure 6.3: The circuit diagram for the spherical-quadrupole magnetic field coils and associated switching components

### 6.3.5 TOP field coils

We used a TOP magnetic trap to confine atoms during the evaporative cooling process. The trap was created by adding a horizontal rotating bias field to the linear magnetic field gradient produced by the spherical-quadrupole magnetic field coils. The rotating bias field was produced by two orthogonal pairs of Helmholtz coils encircling the atom trapping chamber, as shown in Fig. 6.4. Each coil was made from  $\sim 20$  turns of 1-mm thick insulated magnet wire, and wound in a  $\sim 5\text{-cm} \times 12\text{-cm}$  rectangular shape.

Each coil pair was driven with a 10.5-kHz ac current, with a  $\pi/2$ -rad phase shift between the currents in the two pairs to produce the bias field rotation. The phase-shifted ac currents were generated by a single function generator with output divided into two channels and then given the  $\pi/2$ -rad phase difference. Each signal was routed through a differential amplifier, then through a channel in a 500-W audio amplifier. The coils were capacitively coupled to the amplifier output, with the capacitances chosen to match the inductance of the TOP coils at the 10.5-kHz resonance.

The coils produced peak rotating magnetic fields of 80 G at the center of the chamber. The strength of the field was controlled with the output from a triggerable arbitrary waveform generator (AWG) that modulated the amplitude of the 10.5-kHz function generator output. When the TOP field was near its maximum values, it induced inductive heating in the stainless steel chamber. This had the detrimental



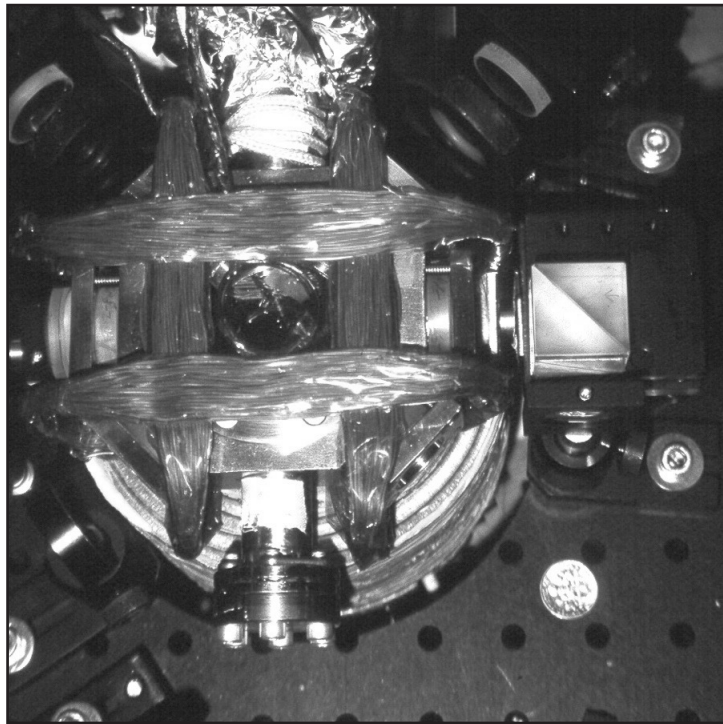


Figure 6.4: The top coils, shown wrapped around the atom trapping chamber.

effect of increasing the pressure in the chamber and shortening the magnetic trap lifetime. In order to maintain long lifetimes and efficient evaporative cooling, we actively water cooled the chamber with copper tubing wound around sections of the chamber.

### 6.3.6 RF coil

The rf magnetic field was produced by two identical 2.5-cm diameter coils with 3 turns on each coil. The coils were wound from magnet wire, and rested against the two 2-inch chamber windows, one above the chamber and one below. The light for the vertically oriented trapping laser beams passed through the center of the coils. The coils were driven at frequencies of  $\sim 0.5$  MHz up to  $\sim 5$  MHz. These frequencies were produced by a triggerable HP frequency synthesizer, whose output was amplified before driving the two coils connected in parallel. The variation of the rf frequency with time was controlled by a linear frequency sweep produced by the synthesizer. An illustration of our apparatus in Fig. 6.5 shows the positions of the field coils.

### 6.3.7 Timing system

The timing sequence of the experiment was controlled with a computer program written by Todd Gustavson. The program controlled digital-to-analog boards with outputs that could be varied independently between -10 and 10 V at times specified by the user. The program provided convenient control of the timing of most of the electronics used in the experiment, whether through TTL triggers or through analog voltage levels.

## 6.4 Sequence

The BEC production sequence can be divided into two separate stages: the laser cooling stage and the evaporative cooling stage. The inherent goal of each stage was to constantly increase phase-space density,  $\rho$ . The  $\sim 150$ -s laser cooling stage of the experiment was oriented towards beginning evaporation with the highest phase-space

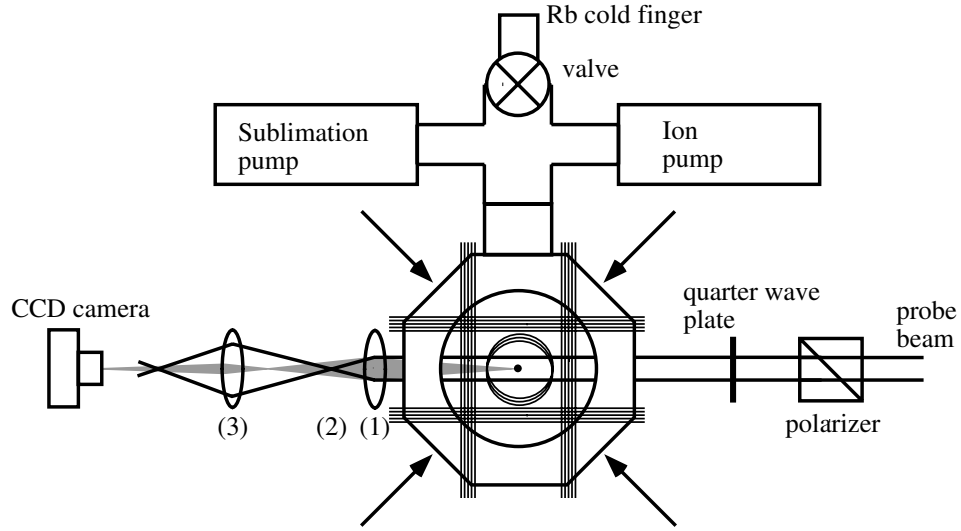


Figure 6.5: Schematic view of the experimental apparatus, showing the vacuum chamber (octagon) and imaging optics (not to scale). The straight lines overlapping the octagon represent the TOP coils that surround the chamber, and the overlapping circles within the TOP coils represent the rf evaporation coils. The four dark arrows represent the four MOT beams that lie in the horizontal plane. The beam paths of the probe beam (dark lines) and the light diffracted/refracted by the atoms (gray filled area) are also shown. The lens at position (1) collected the diffracted/refracted light, which was imaged onto the CCD by the lens at position (3). Position (2) indicates the focus of the unscattered probe light, which was the position of the dark-ground imaging beam block.

density possible, obtained by increasing the number of trapped atoms by first loading the MOT. The evaporative cooling stage was designed to constantly increase  $\rho$  and reach BEC while minimizing the number of atoms lost from the trap.

### 6.4.1 Dark MOT

The most effective method of increasing initial phase-space density was to cool and collect atoms from the background vapor and load them into a MOT. Each of the MOT laser beams had a  $1/e^2$  diameter of  $\sim 1.2$  cm, an intensity of  $\sim 10 I_{sat}$  and was tuned 9 MHz to the red of the  $^{87}\text{Rb}$   $5S_{1/2}, F = 2 \rightarrow 5P_{3/2}, F' = 3$  transition ( $I_{sat}$  is the saturation intensity for the  $F = 2, m_F = 2 \rightarrow F' = 3, m_F = 3$  transition, as given in Appendix A). Another laser beam of intensity  $I_{sat}$  tuned  $\sim 5$  MHz below the  $F = 1$  to  $F' = 2$  transition was used to repump atoms as they decayed into the  $F = 1$  ground state. A 4-mm diameter dark spot in the center of this beam, filled with a second beam tuned to the  $F = 2 \rightarrow F' = 2$  transition, was used to mitigate light-assisted, density-dependent collisional losses, as described in Chapter 5. These losses were further reduced by loading the MOT with a weak ( $\sim 5$  G) rotating magnetic field component, created with the TOP coils, in addition to a quadrupole field gradient of 5 G/cm. We found that this rotating bias field lowered the atomic density in the central region of the trap. This was most likely due to a weaker curvature of the magnetic potential at the bottom of the potential well. Operating with a vapor pressure-limited  $1/e$  loading time constant of  $\sim 90$  s, we typically loaded  $\sim 10^8$  atoms into the MOT in a  $\sim 150$ -s time interval.

### 6.4.2 Transfer to magnetic trap

The next crucial pre-evaporation step was the transfer of atoms from the MOT into the magnetic trap. Following the MOT loading stage, the atoms were compressed in the MOT, then further cooled, before being transferred into the TOP trap. To compress the atoms, the rotating bias field was turned off, the hole in the center of the repumping beam was filled with repumping light tuned to the  $F = 1 \rightarrow F' = 2$  transition, the trapping frequency was detuned to 42 MHz below resonance and the

strength of the spherical-quadrupole field was ramped to  $\sim 8$  G/cm. The MOT compression stage [91], originally used at JILA, was designed to increase the density of the trapped atoms, and thereby increase efficiency in loading into a magnetic trap. The quadrupole field was turned off after the 100-ms compression stage so that the atoms could be cooled in the  $\sigma^+ - \sigma^-$  optical molasses. We found that we were unable to load atoms efficiently into the magnetic trap if the residual bias magnetic fields during this stage were not cancelled properly with the fields from the dc Helmholtz bias coils.

Following the 1-ms cooling interval the molasses beams were extinguished and the atoms were optically pumped into the  $F = 2, m_F = 2$  Zeeman sub-level. The optical pumping was accomplished by turning on a  $\sim 7$ -G rotating bias field and subjecting the atoms to 5 resonant, circularly polarized, optical pulses of intensity  $I = 0.1 I_{sat}$ , each pulse having a  $16\text{-}\mu\text{s}$  duration. The pulses were synchronized with the rotation rate of the field, and occurred when the bias field direction was co-linear with the propagation direction of the pumping beam. We found that using this optical pumping technique was comparable to using a single 0.4-ms pulse of light with a dc magnetic bias field concurrently pulsed on. Either case produced transfer efficiencies of  $\sim 25\%$  into the magnetic trap. Higher percentages could easily be achieved, but at the expense of temperature and an overall decrease in phase-space density of the magnetically trapped atoms.

The efficiency of the transfer into the TOP trap was also sensitive to the parameters of the magnetic field during the transfer, and to the timing of the events during this short period. Slight changes in parameters resulted in initial phase-space densities that were too low to create a BEC. The optically pumped atoms were transferred into the TOP trap using the following sequence. At the end of the optical pumping cycle, the spherical-quadrupole field was snapped on to a radial gradient of  $B'_q = 55$  G/cm while the TOP field was simultaneously established at a strength of  $B_{rot} = 10$  G (500- $\mu\text{s}$  switching time for each field). The field strengths were then linearly ramped over a 900-ms interval to  $B'_q = 275$  G/cm and  $B_{rot} = 36$  G. The number of atoms in the magnetic trap at this point was  $\sim 10^7$  and the phase-space density of the cloud was  $\sim 2 \times 10^{-6}$ . Again, phase-space density is  $n\lambda_{th}^3$ , where  $\lambda_{th} = \sqrt{2\pi\hbar^2/mk_B T}$  is the

thermal de Broglie wavelength, and  $n$  is the atomic density. The parameters used for the transfer were optimized to maximize the phase-space density of the magnetically trapped atoms.

The 900-ms period used to ramp up the field strengths provided adiabatic compression. Although adiabatic changes do not increase the phase-space density, this ramp was designed to increase the spatial density while sacrificing cold temperatures. This was beneficial in initiating forced evaporation, which depends on the re-thermalization rate after an evaporation cut. This rate is proportional to the collision rate, which is inversely proportional to the density. The benefit of increasing temperature and density adiabatically by compressing the trap was thus a decrease in the total evaporation time needed to reach BEC.

### 6.4.3 TOP-induced evaporative cooling

Atoms were further compressed and evaporatively cooled after the initial TOP trap compression stage by reducing the strength of the rotating field. For a TOP trap, the trap curvature is  $B_q'^2/B_{rot}$ . Reduction in  $B_{rot}$  increases the curvature, and hence compresses atoms. The trap depth, on the other hand, scales with  $B_{rot}$ , and thus decreases with decreasing  $B_{rot}$ . The combination of these two effects enables efficient evaporative cooling by reducing  $B_{rot}$ . The compression not only enhances the two-particle collision rate and speeds up the ensemble thermalization time, but simultaneously ejects the most energetic atoms from the trap.

Following Ketterle *et al.* [36], we define efficiency of evaporation as

$$\gamma = \frac{\ln(\rho_{final}/\rho_{initial})}{\ln(N_{final}/N_{initial})}, \quad (6.1)$$

where  $\rho$  is the phase-space density. In order to tune the efficiency of the evaporation sequence, the rotating TOP field strength was ramped down in multiple stages [93]. To maximize  $\gamma$  throughout the evaporation process, the duration and change in magnetic field strength of each segment of the TOP ramp were optimized for maximum phase-space density increase, with the smallest possible loss in number of atoms. The result of our optimization procedure is illustrated in Fig. 6.6. We measured phase-

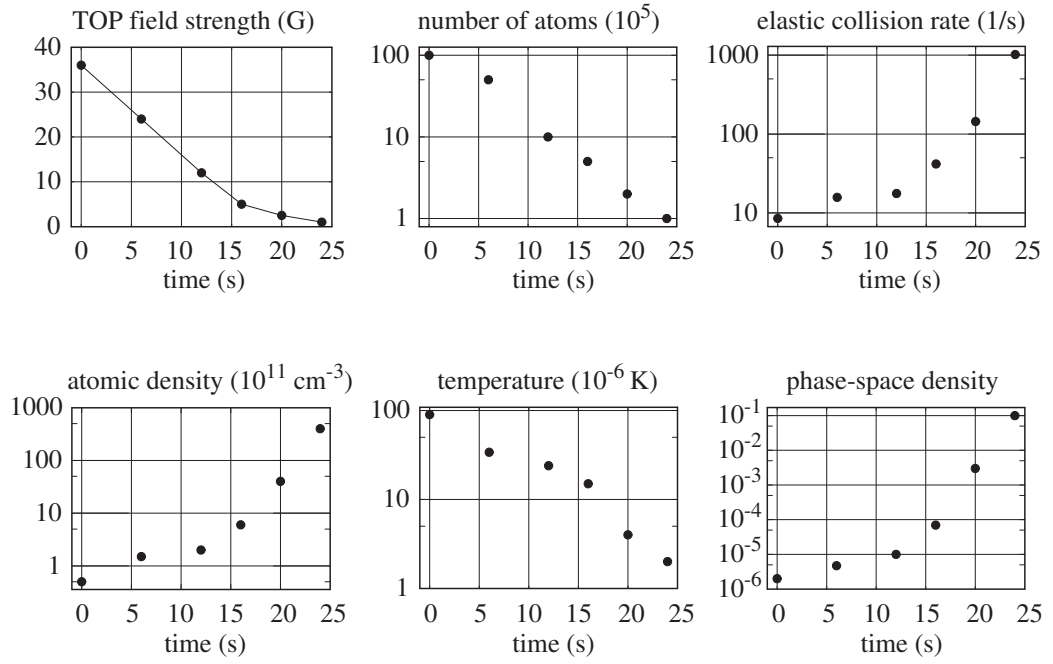


Figure 6.6: Evaporation characteristics *vs.* time for the TOP evaporative cooling ramp. The horizontal axes indicate the time of a measurement, referenced to the beginning of the TOP field evaporation ramp.

space density using standard absorptive imaging techniques, as described below. Over the course of the 24-s TOP-induced evaporation sequence, the loss in number of atoms was a factor of  $\sim 100$ , while the phase-space density increased nearly six orders of magnitude to  $\sim 10^{-1}$ . Our overall efficiency was  $\sim 2.8$ .

#### 6.4.4 Magnetic trap imaging

To image an atom cloud, a collimated probe laser beam with electric field  $\mathbf{E}_{probe}(x, y)$  is sent through the cloud. The transmitted field is given by

$$\mathbf{E}_{trans}(x, y) = \mathbf{E}_{probe}(x, y) \exp[i\beta(x, y)], \quad (6.2)$$

where  $\beta(x, y) = \phi(x, y) + i\alpha(x, y)/2$  is the phase of the transmitted light. Here,

$$\alpha(x, y) = \int n(\mathbf{r})\sigma dz \quad (6.3)$$

is the optical depth of the atom cloud, where  $n(\mathbf{r})$  is the cloud density at position  $\mathbf{r}$ , and  $\sigma$  is the optical scattering cross-section. The dispersive phase shift  $\phi(x, y)$  is determined through the relation  $\phi = -(\Delta/\Gamma)\alpha$ . The object plane, where the atoms and the incident probe laser interact, is imaged onto a camera that records the intensity distribution of the transmitted intensity distribution as a digital image.

Neglecting aberrations of the field in the imaging process, an absorptive image has an intensity distribution at the image plane of

$$I(x', y') = I_0(x', y') \exp[-\alpha'(x', y')], \quad (6.4)$$

where  $I_0$  is the intensity of the unperturbed probe beam at the image plane, and the variables  $(x', y')$  represent image plane coordinates. The function  $\alpha'(x', y')$  is equal to  $\alpha(x \cdot M, y \cdot M)$ , where  $M$  is the magnification of the imaging system. In the image plane, areas with high relative intensity correspond to weak or no absorption. The area of the image that corresponds to the atomic cloud will display a shadow, a dark region where the cloud has absorbed light from the incident beam. After absorption,



the atoms re-radiate photons, whereupon the induced momentum kicks add kinetic energy to the system. The absorptive image is independent of the dispersive phase shift of the light.

We determined the density and temperature of the trapped atoms through absorption imaging. Our imaging geometry is illustrated in Fig. 6.5. To make an absorptive image, trapped atoms were irradiated with low-intensity ( $\sim 10^{-3} I_{\text{sat}}$ ) pulses of light resonant (or nearly resonant) with the optical transition. Each 16- $\mu\text{s}$  circularly polarized pulse was flashed on synchronously with the TOP field when the rotating bias field direction was parallel with the probe propagation axis. The shadow cast by absorption from the atomic cloud was imaged onto a cooled CCD camera. The magnification of our imaging system was  $7.0 \pm 0.3$ . The calculated diffraction-limited resolution was  $\sim 2.6 \mu\text{m}$  ( $1/e$  radius), while the measured resolution was  $3.9 \pm 0.3 \mu\text{m}$ . This measurement was made by imaging small ensembles of atoms in tight trapping potentials, and independently by imaging test targets.

We analyzed the images by first extracting  $\alpha'(x', y')$  from the images, scaling the coordinates to obtain  $\alpha(x, y)$ , then fitting  $\alpha(x, y)$  to a Gaussian distribution. In the harmonic trap, the  $1/e$  size of the trap ( $r_{\perp}$  in the radial direction and  $r_z$  in the axial direction) were directly related to the temperature,  $T$ , of the thermal atoms. Assuming a 3-dimensional Gaussian atom distribution,

$$T = \frac{\mu_B}{4k_B} \frac{B_q'^2 r_{\perp}^2}{B_{\text{rot}}}. \quad (6.5)$$

Cloud temperatures were thus extracted from the fitted widths of  $\alpha(x, y)$ . Densities were inferred from optical depths and widths through Eq. 6.3. Total atom number was obtained from the density and size measurements via

$$N = n_0 (\sqrt{\pi} r_{\perp}^2 r_z)^3, \quad (6.6)$$

where  $n_0$  is the peak number density, and independently from a calibrated photomultiplier tube using light scattered from a separate laser beam. This beam was pulsed on just after each absorption measurement had been completed.

One of the main drawbacks to absorptive imaging was the limited dynamic range in measuring optical depth (the other problem, already mentioned, being the heat added to the system due to photon scattering). As  $\alpha$  increases, the absorption exponentially approaches values near 100%. Small changes in the absorption in this range (above  $\alpha \sim 2$ ) were not detectable, and quantitative information about  $\alpha$  was difficult to determine. For the highest phase-space densities in our experiment, the trapping potential was thus adiabatically relaxed before taking an image, ensuring that the peak optical depth was on the order of unity. The phase-space density in the unrelaxed potential was inferred by scaling from those obtained in the relaxed potentials (adiabatic changes in the trap potential by a factor  $\kappa$  change the trap density by  $\kappa^{3/4}$  and temperature by  $\kappa^{1/2}$ , for a harmonic 3-dimensional trapping potential [36]). The densities were low enough that collective optical excitation effects (such as superradiance) could be ignored.

#### 6.4.5 RF evaporative cooling: reaching the BEC threshold

The final stage of evaporative cooling was accomplished with rf magnetic fields, enabling precise control of the energy of the evaporative cut. The rf field was established using the rf coils described in section 6.3.6. As the rotating bias field magnitude was held at a constant value, the rf frequency was linearly ramped down in a 2 to 4-s cooling interval. The final temperature depended on the rf frequency at the end of the ramp. The threshold rf frequency for condensate formation depended on the magnitude of the rotating field and the number of atoms in the trap, and was measured by changing the final frequency of the sweep.

In order to obtain reliable images of the condensate, the magnetic trapping potential was adiabatically relaxed following the rf sweep, as described in section 6.4.4. This reduced the optical depth of the cloud and increased its size. We typically reduced the trap spring constants by a factor of  $10^3$  over a 0.4-s interval. The elastic collision rates were high enough that the condensate was expected to maintain thermodynamic equilibrium with the normal fraction over the duration of this expansion.

The entire BEC production and measurement sequence is illustrated in Fig. 6.7.

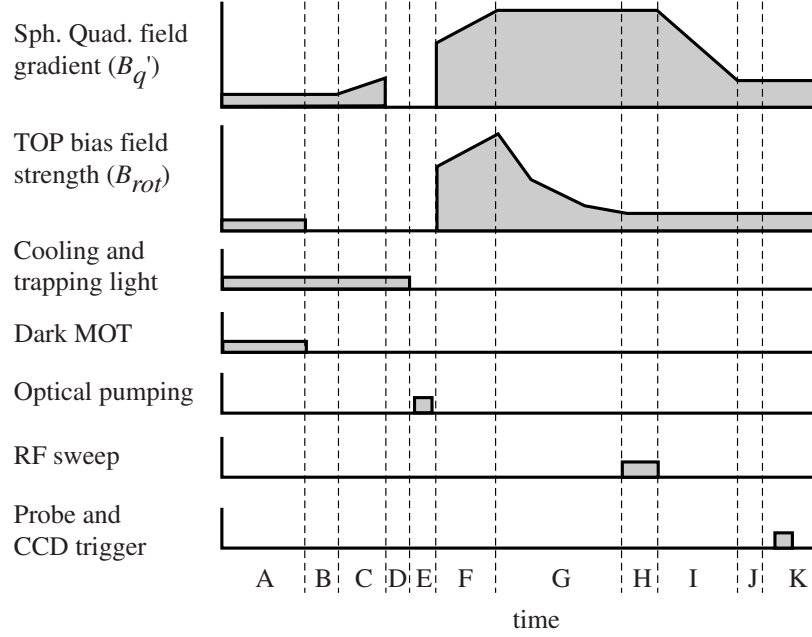


Figure 6.7: The BEC production sequence. Amplitudes of various parameters (not to scale) are shown to the left of the diagrams that they represent. The dashed lines separate the production sequence into time intervals (not to scale), labeled with capital letters at the bottom of the figure. The main events occurring during each time interval are listed in the following table.

interval	event
A	dark MOT loading
B	bright MOT
C	MOT compression
D	cooling in molasses
E	optical pumping
F	adiabatic compression in TOP trap
G	TOP-induced evaporative cooling
H	rf-induced evaporative cooling
I	adiabatic relaxation
J	hold in weak trap
K	BEC imaging

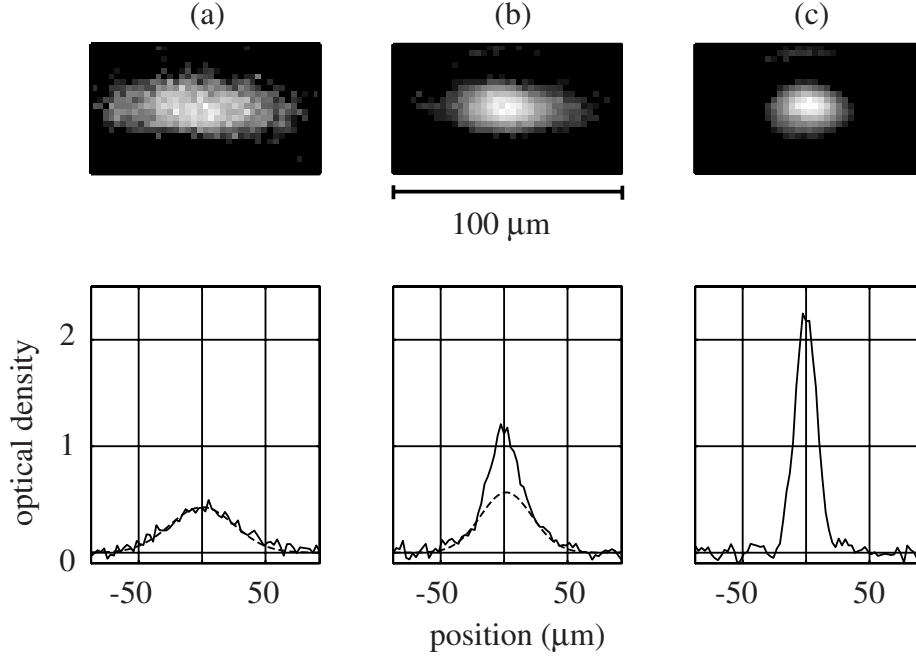


Figure 6.8: Absorption images and corresponding optical density cross sections showing the BEC phase transition for final rf frequencies of (a) 1.80 MHz, (b) 1.75 MHz, and (c) 1.68 MHz. In (a), a single Gaussian distribution fits the data well. For (b), the fit of a Gaussian distribution to the normal fraction is shown.

## 6.5 BEC measurements and images

Figures 6.8 and 6.9 show images of trapped atoms above and below the condensation threshold. Three different final rf values of the rf evaporative cooling ramp are represented in Fig. 6.8: a frequency of 1.80 MHz, which was just above the condensation threshold; 1.75 MHz, which was just below the threshold; and 1.68 MHz, which was far enough below the threshold to produce a nearly pure condensate (the normal fraction was not resolvable). Images were acquired with up to four pulses of light. We observed no change in the condensate images with an increasing number of detection pulses, indicating negligible heating during the measurement. The images were analyzed by fitting two 2-dimensional Gaussian distributions to  $\alpha(x, y)$ . These Gaussians fit a wide distribution, corresponding to the normal (uncondensed) fraction at

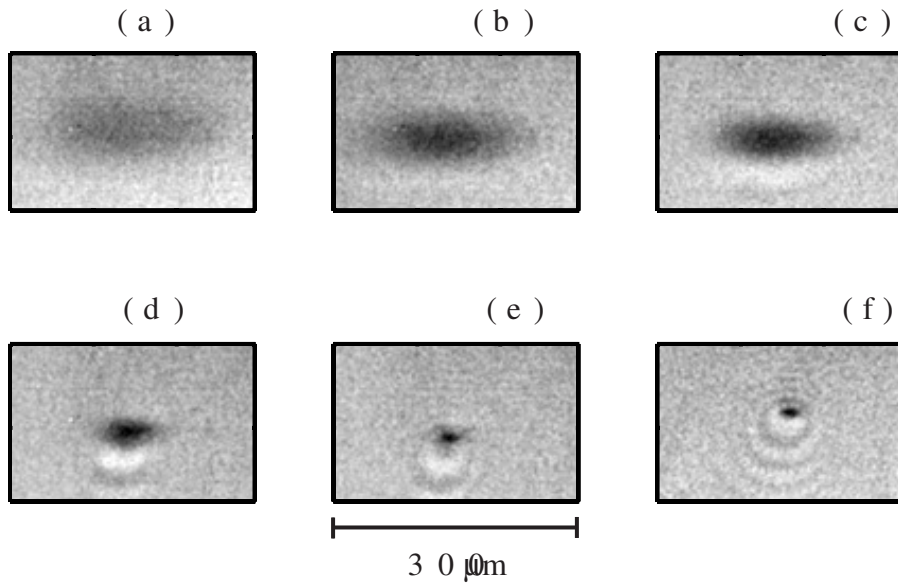


Figure 6.9: Images of the BEC transition for final rf sweep frequencies of (a) No rf applied, (b) 2.10 MHz, (c) 1.90 MHz, (d) 1.65 MHz, and (e) 1.60 MHz. The condensate transition for this sequence occurred near 1.75 MHz. (f) An image of a condensate in a strong magnetic trap, with low numbers of atoms. This image was used as a test of the resolution of the imaging system.

the wings of the observed atom cloud, and a narrow distribution, corresponding to condensed atoms at the center of the atom cloud. We extracted the optical depth and size for both the normal and condensed fractions of the cloud from these fits. We then corrected the measured widths for the finite resolution of our imaging system. The temperature ( $T$ ) was determined from the size of the normal cloud. The number of atoms in the condensate ( $N_C$ ) and in the normal fraction were inferred from the optical depth and size of each component. The total number of atoms ( $N$ ) was determined by summing the number in each component.

We were also able to achieve condensation solely through manipulation of the TOP field strength, without the use of an rf cooling ramp. Figure 6.10 illustrates evaporative cooling with a final TOP ramp compared to a final stage of rf cooling. The rotating bias field of the TOP was first ramped down to  $\sim 1.1$  G. An image of the trapped atoms at this point is represented in Fig. 6.10(a). The sequence of images shown in Fig. 6.10(b-e) demonstrates the effects of an additional 4-s TOP evaporation ramp to various lower field strengths. In Fig. 6.10(e), for example, the TOP field is ramped to  $\sim 0.25$  G, creating a nearly-pure BEC with  $\sim 4000$  atoms. As a comparison, the rotating bias field strength was left at  $\sim 1.1$  G, and a 4 s rf ramp from 2.4 MHz down to various lower frequencies was applied. The images in Fig. 6.10(f-i) demonstrate this rf cooling method. Figure 6.10(i), for example, was obtained after ramping the rf field down to 1.50 MHz, producing a nearly-pure BEC containing  $\sim 1.2 \times 10^4$  atoms. Our results indicated that evaporative cooling solely with TOP-induced evaporation was not as efficient as the hybrid sequence described previously, and resulted in condensates with fewer atoms than could be obtained through the use of rf evaporative cooling.

As an independent check on our imaging we also observed the transition using the dispersive dark-ground imaging technique [92]. In this case, the image forms as a result of the lensing of the light as it refracts on passage through the atomic cloud. The image is observed by blocking the non-refracted beam at its focus in the imaging system, as described in Refs. [94] and [92]. The intensity of the probe beam at the

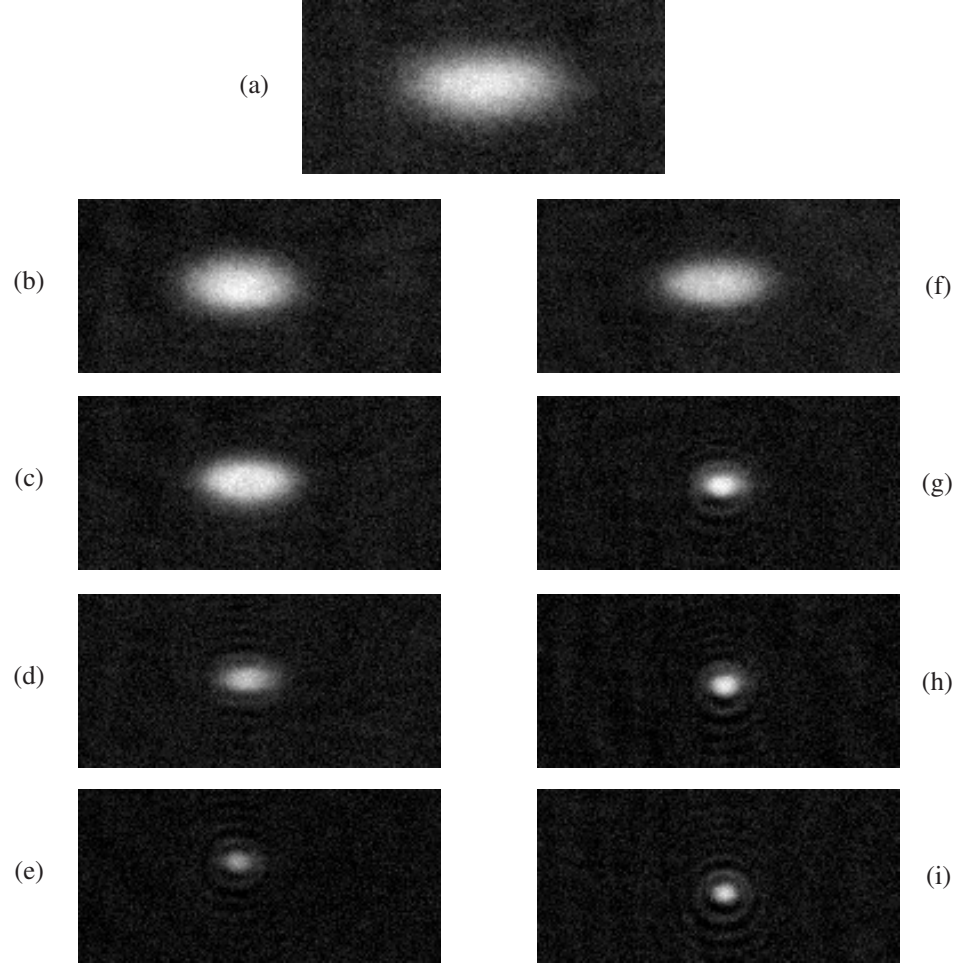


Figure 6.10: Images of trapped atoms after TOP-induced evaporative cooling compared to rf-induced cooling. Background subtraction of absorptive images in a weak trap was used to obtain these images. (a) The TOP field is initially ramped to  $\sim 1.1$  G before RF-induced cooling or further TOP-induced cooling. This condition is the starting point for all further images in this figure. Images (b)-(e) represent TOP-induced cooling to the BEC threshold. Images (f)-(i) represent rf-induced cooling to the BEC threshold. Top ramps: a final TOP ramp from 1.1 G to (b) 0.60 G, (c) 0.45 G, (c) 0.30 G, (e) 0.25 G. RF-induced cooling: a final rf ramp from 2.40 MHz to (f) 1.80 MHz, (g) 1.55 MHz, (h) 1.50 MHz, (i) 1.45 MHz. All images have identical intensity scales, and represent an area of  $370 \times 180 \mu\text{m}$ .

image plane in this case is given by

$$I(x', y') = I_0(x', y') |\exp[i\beta(x', y')] - 1|^2. \quad (6.7)$$

For the conditions  $\alpha \ll \phi \ll 1$ , the image intensity scales as  $I(x', y') \propto \phi^2(x', y')$ .

For dark-ground imaging, we blocked the non-refracted probe light by inserting a 180- $\mu\text{m}$  diameter wire in the focus of the probe beam (position 2 in Fig. 6.5) after the beam exited the chamber. For the conditions of our images, the maximum values for  $\phi$  approach 1 rad. We analyzed these images by fitting Gaussians to  $\phi(x, y)$ , then extracted temperature, number, and condensate fraction as described above.

## 6.6 BEC results

As described in Chapter 2, for a non-interacting trapped Bose gas in the thermodynamic limit ( $N \rightarrow \infty$ ), the condensate fraction is  $N_C/N = 1 - (T/T_C)^3$  with a transition temperature of  $k_B T_C = \hbar \bar{\omega} (N/\zeta(3))^{1/3}$ , where  $\bar{\omega}$  is the geometric mean of the trap oscillation frequencies [52]. Figure 6.11 shows  $N_C/N$  vs.  $T/T_C$  for three data sets. The first and second sets were taken using absorptive imaging, while the third set was taken using the dispersive dark-ground technique. The trap strength (as characterized by the radial oscillation frequency  $\omega_\perp$ ) was  $\omega_\perp = 2\pi \cdot 8$  rad/s for the first set, and  $\omega_\perp = 2\pi \cdot 13$  rad/s for the second and third sets (these frequencies were inferred from the measured magnetic field strengths). In this analysis,  $N_C/N$ ,  $T_C$ , and  $T$  were extracted from the images. To determine the dependence of  $N$  (and thus  $T_C$ ) on  $T$  for the data of Fig. 6.11, we first fit a line to  $N$  vs.  $T$  data extracted directly from our images and then use the fitted functional form to compute the normalized condensate temperature  $T/T_C$ . In order to avoid potential systematic biases in the absorption data, we captured these images at several probe detunings (ranging from -50 MHz to -10 MHz).

Although the data were in good agreement with ideal gas theory, we expect corrections in the transition temperature due to finite number and interaction effects. For our parameters, the interaction correction is  $\sim 1\%$  [96] and the finite number



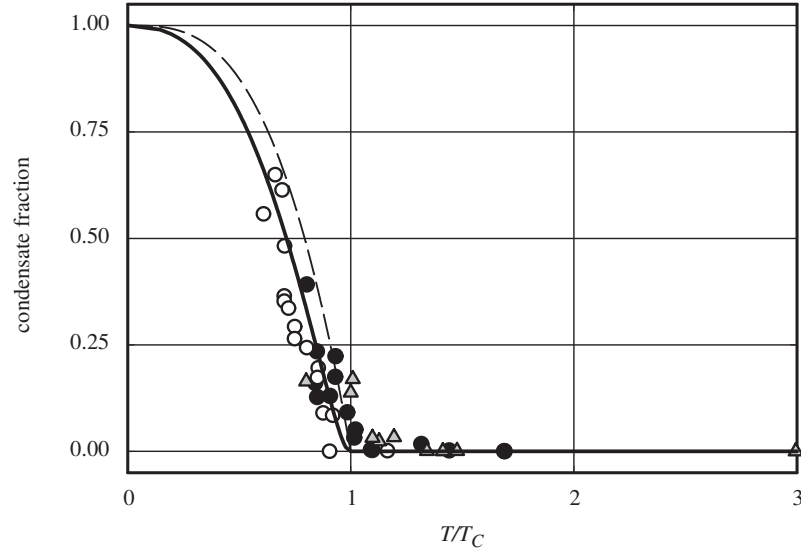


Figure 6.11: Condensate fraction as a function of  $T/T_C(N)$ . The filled circles represent data taken with absorption imaging at a trap strength of  $\omega_{\perp} = 2\pi \cdot 8$  rad/s, the open circles represent data taken with absorption imaging at a trap strength of  $\omega_{\perp} = 2\pi \cdot 13$  rad/s, and the triangles represent data taken with dispersive dark-ground imaging at a trap strength of  $\omega_{\perp} = 2\pi \cdot 13$  rad/s. Each data point represents a single image. The shot-to-shot variance of the total number  $N$  was approximately 30%. The solid curve is the expected behavior of the condensate fraction with temperature in the semi-ideal gas limit (see Ref. [95]), and is not a fit to the data. The dashed curve illustrates the expected behavior of a non-interacting gas.

shift is  $\sim 2\%$  [97, 98], well below the resolution of our measurements. The solid line shown in the figure is the theoretical curve for our trap parameters (not a fit to the data), and shows the expected behavior of the condensate fraction with temperature for a semi-ideal gas.

Mean-field effects arise due to the interactions between atoms in the condensate. For atoms with repulsive interactions, such as  $^{87}\text{Rb}$ , a dense condensate will raise the energy (chemical potential) of each atom in the BEC by an amount that is proportional to the local density. The interactions tend to increase the size of the condensate over that expected for a non-interacting gas. The resulting atomic density distribution in the condensate is parabolic for a system in the Thomas-Fermi limit, where the condensate kinetic energy is small compared with the mean-field energy. The aspect ratio of the BEC also changes as a result of the interactions.

By varying the strength of the trapping potential, the density can be varied, and the role of the mean-field interactions on condensate characteristics can be studied. In our system, the BEC in the stronger trapping potentials was well into the Thomas-Fermi limit. The trap was optically thick, and the trap radius was below the resolution of our imaging system. We were thus unable to study the BEC characteristics in the tight traps.

We characterized the effects of the mean-field interaction in the weak traps, where the condensates were not well into the Thomas-Fermi limit [53], through direct observation of the size and shape of the condensate. In the Thomas-Fermi limit, the condensate aspect ratio is  $8^{1/2}$  and the density profile is parabolic. For smaller numbers of atoms, where kinetic energy is no longer negligible, a variational solution of the non-linear Schrödinger equation, which includes the mean-field potential energy term, can be used to predict the size and shape of the condensed cloud. A simple variational ansatz for the ground state is a Gaussian wavefunction [53]. With this assumption, the aspect ratio varies continuously between that of a harmonic oscillator ground state,  $8^{1/4}$ , and the Thomas-Fermi value of  $8^{1/2}$  as the number of atoms increases. For the data shown in Fig. 6.8(c), the observed condensate aspect ratio is  $2.3 \pm 0.3$ , significantly less than the Thomas-Fermi prediction of 2.82. The error is dominated by uncertainty in the resolution of the imaging system. With a measured

value of  $N_C = 3 \pm 1 \times 10^4$  atoms and  $\omega_{\perp} = 2\pi \cdot 13$  rad/s, the aspect ratio predicted by a variational calculation using a Gaussian trial function is 2.7, 17% larger than the observed value. The predicted radial size of  $7.8 \mu\text{m}$  is slightly less than our observed radial size of  $9.2 \pm 0.6 \mu\text{m}$ . Note that the observed shift in aspect ratio between the condensed and normal cloud is an independent signature of condensation, analogous to the anisotropic momentum distributions observed in the initial BEC studies. For comparison, the normal fraction aspect ratios of the images shown in Figs. 6.8(a) and 6.8(b) are  $\sim 2.8$ . (The expected normal fraction aspect ratio, determined by the trap equipotential surfaces, is  $8^{1/2}$ ).

## 6.7 On-resonance dark-ground imaging

For imaging the condensates, we found higher signal-to-noise and more flexibility with an on-resonance dark-ground imaging (ODI) technique than with either of the two previously mentioned imaging methods. With ODI, we used the same experimental setup and procedure for imaging a condensate as for dispersive dark-ground imaging, but we tuned the probe frequency to the atomic resonance. In this case, Eq. 6.7 is reduced to

$$I(x', y') = I_0(x', y') [\exp[-\alpha(x', y')/2] - 1]^2, \quad (6.8)$$

since the phase shift  $\phi$  is zero for resonant light. An analysis of the transmitted intensity *vs.*  $\alpha$  for the absorptive imaging and ODI cases reveals a wider dynamic range for ODI, indicating that the technique is more flexible than absorptive imaging. However, as with absorptive imaging, ODI adds energy to the system, destroying the BEC.

This new technique enabled us to achieve higher signal-to-noise ratios (SNR) than with the other imaging techniques. Although the images appeared similar to the dark-ground dispersive images, the ODI method provided a more intense signal for relatively low-number condensates such as ours. Also, the ODI technique was free of the background subtractions necessary with absorptive imaging, which we found to increase the noise level of our images.

We observed the BEC transition with the ODI technique by imaging the trapped atoms after rf ramps of steadily decreasing final frequencies. For each image, a new BEC was created. We began imaging the atoms well above the BEC threshold, and continued producing condensates and acquiring images for steadily fewer and fewer atoms. This sequence of images is shown in Fig. 6.12. Optical density cross sections for these images are shown in Fig. 6.13.

The increased SNR allowed us to image condensates with very small numbers. Figure 6.14 is an image and optical depth cross section of a condensate measured to consist of  $\sim 100$  atoms. The cross section, an integration of the spatial density over three rows of pixels, shows the SNR, and indicates that the ability to resolve condensates with even lower numbers of atoms is likely without further modifications to the system. In other work with small-number condensates, phase-contrast imaging has been shown to be very sensitive to atom number in  $^7\text{Li}$  BEC experiments at Rice University [55, 99, 100].

## 6.8 Calibrations, systematic errors, and measurement uncertainties

We estimated our measurement errors and uncertainties using standard error analysis techniques. Because the results of many of our measurements originated in the absorption images of the condensates, the source of much of our measurement uncertainty was in the image analysis.

### 6.8.1 Imaging system

The inferred temperature, phase-space density, number, and number density distribution all relied on the measured size of the condensate (or thermal cloud). The inferred size of the condensate depended upon the measured size of the image, the magnification of the imaging system, and the resolution of the imaging system.

We calibrated the magnification of the imaging system *in situ*, without removing the lenses in the beam path. We added a lens of focal length  $f$  to the probe-beam

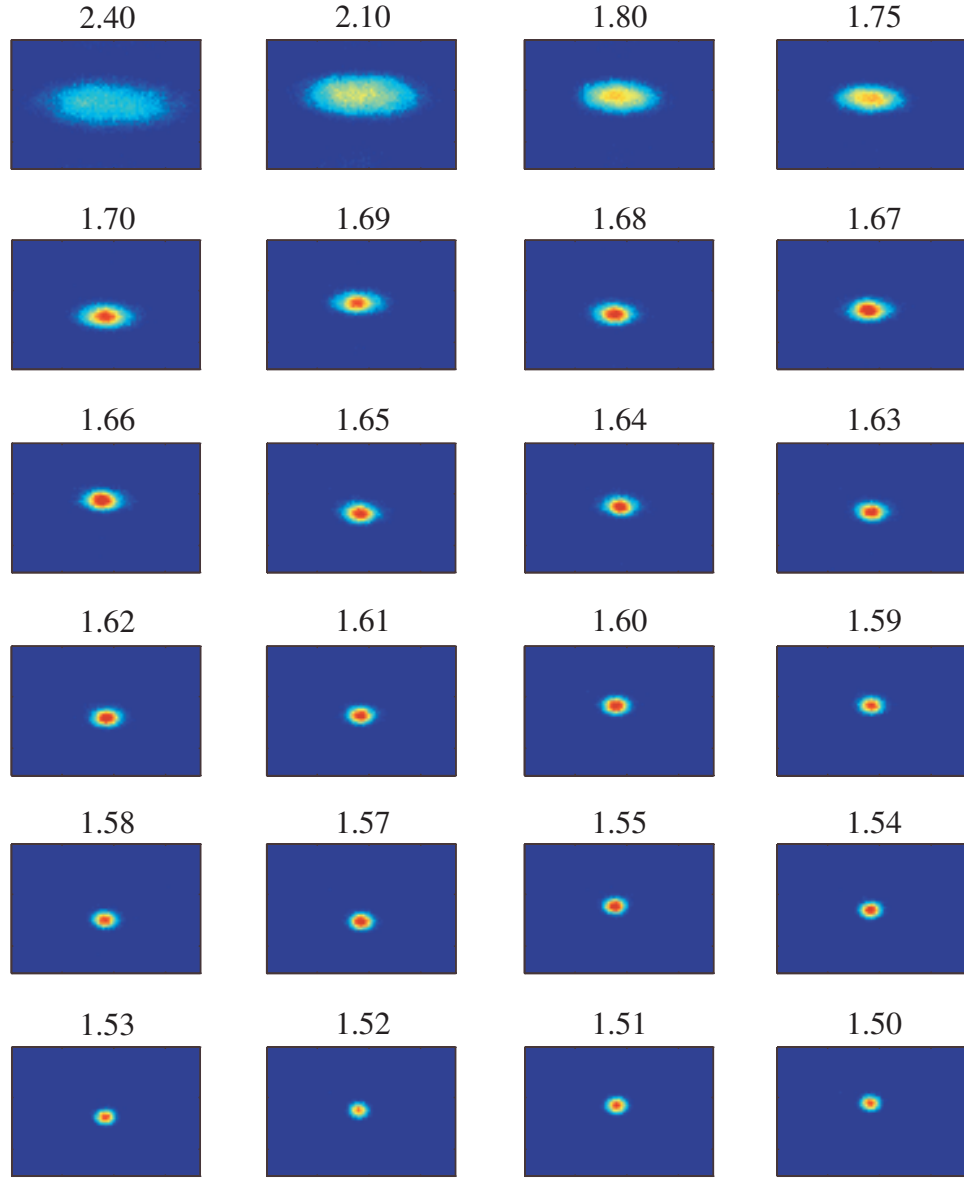


Figure 6.12: The BEC transition, using on-resonance dark-ground imaging. The final value of the rf ramp (in MHz) is listed above each image. Each image represents a width of  $171\ \mu\text{m}$ .

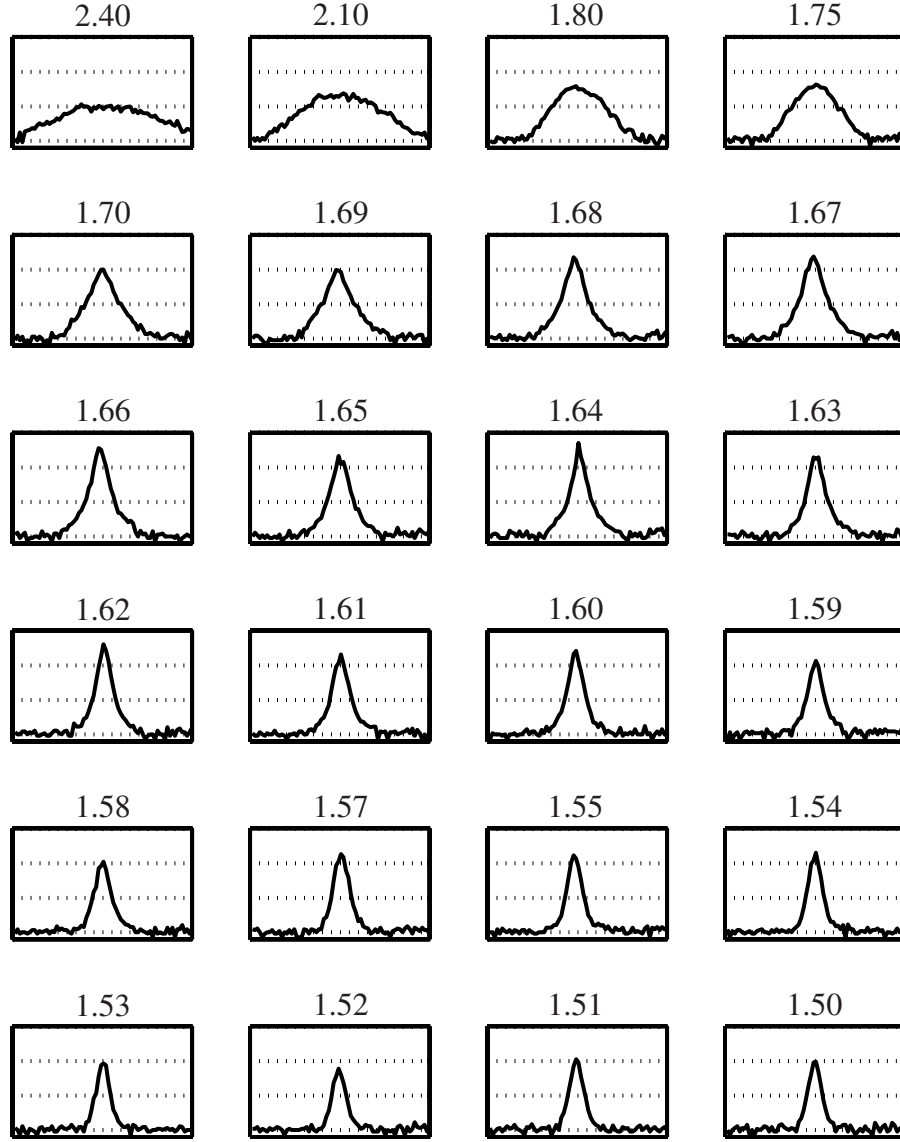


Figure 6.13: Optical density cross sections of the images of Fig. 6.12, showing the BEC transition with on-resonance dark-ground imaging. The final value of the rf ramp (in MHz) is listed above each plot. Each plot represents a width of  $171 \mu\text{m}$ .

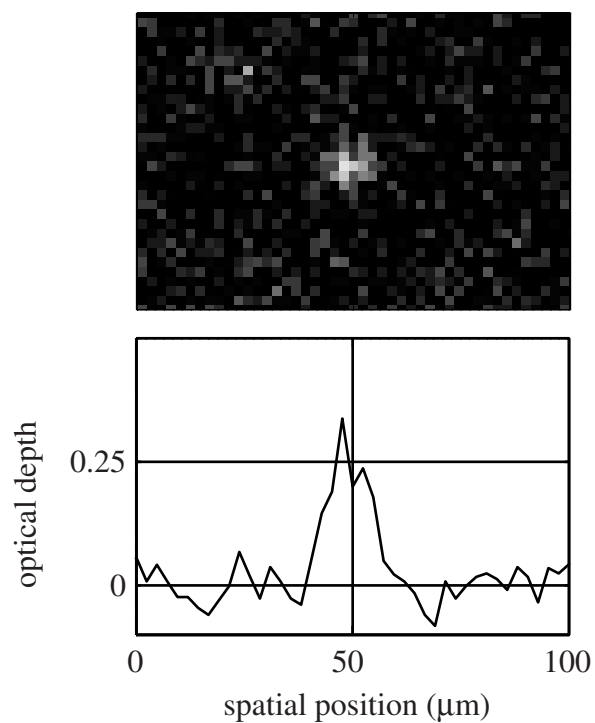


Figure 6.14: (a) An image of a BEC with  $\sim 100$  atoms, taken with on-resonance dark-ground imaging. (b) A horizontal cross section of the optical depth of the image in (a).

input side of the chamber at a distance of  $\sim 2f$  from the center of the chamber. On the input side of the lens, we installed a slit directly in the probe beam path on a translation stage that could move in a direction transverse to the beam. The slit was placed  $\sim 2f$  from the lens, precisely where its image was projected at the center of the chamber and then onto the camera. The thin lens approximation was used to help judge the accuracy of the distances measured. As the slit was scanned through the beam, we recorded the positions of the images with the CCD. The magnification of the modified imaging system was then the ratio of the separation of the images on the camera to the steps of the translation stage. The magnification calibration was further modified by taking into account the shifts produced by the input window of the optical system (the polarizing cube was removed) and the initial magnification produced by the temporary lens. The result was a magnification calibration of the imaging system with 5% uncertainty.

The resolution of the system was tested in two independent ways, also *in situ*. The first method used the same optical path as the magnification calibration. We imaged the slit and various sized pinholes onto the CCD. From the images and the magnification of the system, we were able to estimate a resolution limit. In an independent resolution check, we imaged a nearly-pure small-number condensate in a tight magnetic trap. We assumed that the actual size of the condensate was smaller than the measured size indicated (we were in a regime where this assumption was justified). These two resolution measurements gave an  $\sim 8\%$  resolution uncertainty to our measurements.

In order to extract a  $1/e$  radius from the images, we used a data analysis routine which fit Gaussian distributions to the data cross sections, after extracting the optical depth from the image intensity distribution. The appropriateness of Gaussian fits can be justified by realizing that our data were taken in a regime far from the strong Thomas-Fermi limit. We further analyzed the image of a test target with sharp edges of a size near the diffraction limit. The resulting distribution was largely Gaussian. Thus, at our resolution, we would not be able to distinguish between a trap with a Gaussian distribution and one with a parabolic distribution, as predicted for the Thomas-Fermi limit. We thus estimated a random error of  $\sim 5\%$  in extracting the



size of the distributions of the images, taking into account the finite size of the pixels of the camera.

For highly optically dense images, we observed fringes around the condensates (in off-resonant absorption imaging) due to the limiting apertures in the system and light scattered at wide angles from the condensate. Also under these severe conditions, the lensing of the light upon passing through the condensate could potentially shift the focus of the imaging system, ruining the calibrations for the image. Thus the uncertainties quoted above are for the cases of images of atoms in adiabatically relaxed traps, or for images that were not optically thick.

Lens aberrations in the system were not problematic, due to using only the central portion of the lenses. The limiting aperture in the system was the wall of the vacuum chamber, and the emerging light passed through the center of the lenses.

Our measured maximum absorption of the probe light upon passing through a trap depended upon a background image with probe light and without atoms. We subtracted the atom image from the background image. Thus, fluctuations of the light levels in the time between taking the two images would effect the measurement of the trap absorption. We estimated this fluctuation level to be  $\sim 10\%$ .

### 6.8.2 Magnetic fields

The strengths of the rotating magnetic field,  $B_{rot}$ , and the linear field gradient,  $B'_q$ , also entered into the calculations used to infer condensate characteristics.

The gradient was calibrated against current in the field coils in multiple ways. First, the coil geometry was well defined, and because we trapped atoms along the axis of the coils,  $B'_q$  was easily calculated from the known geometry of the coils and their distances from the trap center. We also measured the trap position as current in the coils (trap potential strength) was varied. Because of the changing relative strengths of the field and the gravitational potential, the position of the trap shifted along the axis of the coils. We determined the strength of the magnetic field from various trap positions and measured spatial shifts. Finally, we checked the field calibration with a magnetometer. The results of these calibrations led to an uncertainty of the field

gradient of  $\sim 10\%$ .

We also calibrated the strength of the rotating field using various methods. First, as we did for  $B'_q$ , we calculated the expected field. Second, with the coils removed from the chamber, we measured the field strength for each coil pair with a magnetometer and a dc driving current. Then we placed the coils around a second chamber identical to the one used in the experiment. With an ac current driving the coils, we used a magnetic field pick-up loop placed inside this chamber to measure the attenuation of the field due to inductive losses in the metal walls. We chose a field rotation frequency (10.5 kHz) where these losses ( $\sim 30\%$ ) appeared minimal for our chamber. With an ac current probe, we were easily able to monitor the current in the coils at our rotation frequencies. We could then infer the strength of the field from the measured current and the measured attenuation and field strength calibration. As an independent measurement of  $B_{rot}$ , we trapped atoms in the TOP trap at large  $B_{rot}$ . The trap was thus shallow and large. With the coils used for rf evaporative cooling, we swept through the rf frequencies corresponding to the Zeeman shifts of the magnetic sublevels. In a manner identical to rf-induced evaporative cooling, we ejected a certain percentage of atoms from the trap as a function of frequency. By measuring the number of atoms lost (with resonant laser light and a PMT), we determined the depth of the potential. The frequency at which all of the atoms had been ejected from the trap corresponded to the bottom of the trap, and the Zeeman shift corresponding to that frequency was induced by the magnitude of the rotating field. These calibration methods gave an uncertainty of  $\sim 10\%$  to our determination of  $B_{rot}$ .

### 6.8.3 Laser light

In our absorption imaging measurements, the value of the detuning of the low-intensity probe light contributed uncertainty to the determination of the atom-photon scattering cross section,  $\sigma$ . We could determine relative frequencies with high accuracy and resolution with frequency counters attached to the modulators which shifted the laser's frequency. Absolute frequencies were calibrated by observations of trapped

atoms. Maximum light scattering of trapped atoms occurred near the resonance of the Rb optical transition for very weak magnetic fields. With absorption imaging, the frequency determined the observed size and absorption of atoms trapped in the TOP trap and in a spherical-quadrupole trap. By observing traps over a wide frequency range, we could calibrate our detunings to  $\sim 3$  MHz.

#### 6.8.4 Random noise and fluctuations

The random noise and shot-to-shot fluctuations of the experiment were difficult to assess, due to variations in the fluctuations depending upon the measurement technique used, the stability of the apparatus, environmental variables, and many other factors. For example, a fluctuating room temperature would vary the pressure within the chamber and the stability of the lasers (even with the temperature feedback loops). Occasionally a loud noise would affect the laser stability, though other vibrations were also troublesome (such as a door quickly closing or a falling object from a nearby room). Some of these problems were eliminated by working with a table which rested on a cushion of air between the table and the table legs. This certainly improved the stability of our lasers. Typical shot-to-shot variations were  $\sim 30\%$ . Some data runs had more fluctuations for various reasons, which could sometimes be tracked down and corrected, while scatter in other data runs was minimal throughout the run.

#### 6.8.5 Error analysis

With the calibrations and uncertainties described above, we used simple propagation of errors to estimate the systematic uncertainties in our measurement of trap and condensate characteristics. Table 6.1 lists relative uncertainties for various quantities.

#### 6.8.6 Limitations

The numbers of atoms in our condensates were limited by the number transferred into the magnetic trap from the MOT. We do not perceive this as a drawback, as there are

Property		Relative uncertainty (approximate)
$M$	(magnification)	5%
	resolution	10%
$r$	(trap radius)	10%
$B'_q$	(linear field gradient)	10%
$B_{rot}$	(rotating field strength)	10%
$\Delta/2\pi$	(laser detuning)	3 MHz
$\sigma$	(photon scattering cross section)	10 to 25%
$\omega$	(trap frequencies)	10%
$\alpha$	(optical depth)	8 to 25%
$n_0$	(peak density)	15 to 40%
$T$	(temperature)	30%
$\rho$	(phase-space density)	50%
$N$	(number)	30%
$T_C$	(condensation temperature)	15%
$N_C/N$	(condensate fraction)	40%
	aspect ratio	12%

Table 6.1: Relative uncertainties of trap characteristics. In some cases, a range is given when the parameter's uncertainty is highly variable.

many interesting potential experiments associated with small condensates. However, in order to increase the number of atoms in the condensate, we must increase the number of atoms loaded into our MOT, and possibly improve transfer efficiency.

The lifetimes of our condensates in the weak trap were probably limited by background gas collisions instead of heating or collisions between trapped condensate atoms. In the stronger traps, as mentioned, the lifetimes were very short, and our estimated densities suggested that 3-body losses were a likely limiting factor for these condensate lifetimes. In the weaker traps, this did not seem to be a problem. We measured lifetimes of condensates of at least 15 s.

## 6.9 Apparatus improvements

One of the main drawbacks of using a single-chamber vapor cell system such as ours was the long cycle times needed to load atoms into the MOT before evaporative cooling in the TOP trap. The repetition rate could probably be increased by using the LIAD techniques described in the previous chapter. While we currently use the LIAD loading method in the BEC production cycle, it initially offered relatively little gain. This was probably due a low adsorption rate on the walls of the chamber. When the valve between the Rb source and the trapping chamber was closed, the Rb in the system was pumped out of the chamber in a short amount of time (about 2 days), indicating that the Rb vapor in the vapor cell needed continuous replenishment from the source. Over time, this condition has become less noticeable. Enough Rb now adheres to the walls of the chamber so that LIAD is effectively used and our current BEC production cycle includes a WLS-loaded MOT phase.

Other modifications to the existing apparatus could be made to decrease the loading time, without constructing a system with a Zeeman slower or a double-MOT system. An atomic-beam Rb source, with a nozzle near the trap, would substantially decrease the loading time. As described earlier in this thesis with lithium, pre-cooling an atomic beam is not a necessary requirement for effective loading into a MOT. Such an atomic beam could be relatively easily installed in our system. One additional requirement with this technique would be the ability to shutter the atomic beam or

turn it off completely for the magnetic trap portion of the cycle (where long loading times and low background collision rates are crucial).

A similar limitation is the low number of atoms loaded into the MOT. While low-number condensates have properties of interest and will continue to be studied, a higher number of initial atoms would make evaporation easier. And of course, it would allow for larger numbers of atoms in the condensate if that is desired. The solutions presented above for decreasing the loading time would also increase the number. Yet another way of increasing the number would be to increase the intensity of the laser cooling and trapping beams. We are currently in the process of such an upgrade. A final technique that could potentially improve the MOT capture rate would be a spectrally broadened source similar to the one described for Li earlier in this thesis. In this case, the center region of the beams should be blocked so that the atoms would not suffer comb induced losses as described earlier. However, due to loading a dark MOT, this problem might already be solved by trapping atoms in a dark state, and we would only need to add the spectrally broadened light to try to increase the number of atoms loaded.

A different limitation in the apparatus is the inductive heating of the stainless-steel chamber when the TOP is run at its maximum strength. We water cool the chamber to combat this heating, but an increase in background pressure after running the TOP is still noticeable. This shortens the lifetime of the magnetic trap. The problem could be addressed by more efficient cooling of the chamber. Alternatively, with modifications to the system as described above, the TOP would not need to remain at full power levels as long, since the evaporation rate could be increased.

The final major improvement to the apparatus that is currently planned is to enhance the quality of our imaging system. The main improvements planned are the purchase of higher quality imaging lenses and a camera with higher signal-to-noise than the one that we currently use. This upgrade would allow us to image smaller-number condensates with better resolution. Implementing a phase-contrast imaging technique may also improve our atom-number resolution. Another improvement gained with the purchase of a better imaging camera would be the ability to re-trigger the camera during a single cycle, taking multiple images of the same BEC.

This process would require the implementation of non-destructive imaging, a technique that is currently in use in other experimental groups studying condensates.

## 6.10 Summary

First, we demonstrated efficient evaporative cooling by ramping the magnetic fields of the confining potential. We produced Bose-Einstein condensation of  $^{87}\text{Rb}$  and used direct imaging techniques to obtain quantitative comparisons with theory for relatively small numbers of atoms. Finally, we showed that on-resonance probe light can be used with dark-ground imaging to obtain high signal-to-noise images of trapped atoms.

# Chapter 7

## Atomic tunnel arrays

### 7.1 Introduction

The demonstration of Bose-Einstein condensation in atomic gases [22, 23, 24] has raised the possibility of exploring relationships between coherence properties of atom vapor Bose-Einstein condensation [101, 102, 103, 104], superfluid He [105], and superconductivity [106]. These quantum systems share common theoretical framework and exhibit similar observable characteristics. In this chapter, we discuss observed behavior [31] of an optically trapped Bose-Einstein condensate analogous to the Josephson effect of superconducting systems.

### 7.2 Josephson effects in superconductors

Josephson effects [106] are a range of phenomena exhibited by two superconductors separated by a thin insulating barrier (a Josephson junction). For thin enough barriers, electron tunneling through the barrier couples the dynamics of the two macroscopically occupied quantum states. Under appropriate conditions [107], the wavefunction of each superconductor can be approximated as

$$\Psi_q = n_q^{1/2} e^{i\phi_q(t)}, \quad (7.1)$$



where  $q$  represents either superconductor 1 or 2,  $n$  is the electron number density of the ground state system, and  $\phi$  is the relative macroscopic phase. In the absence of coupling, the electron number density of each superconductor remains constant with time, and the phase evolves at a rate of  $\mu/\hbar$ , where  $\mu$  is the chemical potential.

For weakly coupled superconductors, the equations of motion are [108]:

$$i\hbar \frac{\partial \Psi_1}{\partial t} = \mu_1 \Psi_1 + K \Psi_2, \quad (7.2)$$

$$i\hbar \frac{\partial \Psi_2}{\partial t} = \mu_2 \Psi_2 + K \Psi_1, \quad (7.3)$$

where  $K$  represents the strength of the coupling. By inserting Eq. 7.1 for  $\Psi_1$  and  $\Psi_2$  into Eqs. 7.2 and 7.3, one obtains

$$\frac{\partial n_1}{\partial t} = 2(K/\hbar) n_1^{1/2} n_2^{1/2} \sin(\phi_2 - \phi_1), \quad (7.4)$$

$$\frac{\partial n_2}{\partial t} = -\frac{\partial n_1}{\partial t}, \quad (7.5)$$

$$\frac{\partial(\phi_2 - \phi_1)}{\partial t} = -(\mu_2 - \mu_1)/\hbar. \quad (7.6)$$

The first two of these equations describe the rate of change of electron densities, while the third describes the evolution of the phase difference between the two wavefunctions, valid for large  $n_1$  and  $n_2$ , with  $n_1 \simeq n_2$ .

When a dc voltage  $V$  is applied across the tunnel junction, the chemical potential difference is given by  $\mu_2 - \mu_1 = 2eV$ , resulting in linear evolution of the phase difference (phase slip). The flux of particles through the barrier can be written as an oscillating current:

$$I = I_0 \sin(\phi_2(t) - \phi_1(t)) = I_0 \sin(2eVt/\hbar + \Delta\phi(0)), \quad (7.7)$$

where the amplitude  $I_0$  is proportional to the strength of the coupling, and  $\Delta\phi(0)$  is the initial relative phase difference. This ac current modulation, resulting from the application of a dc voltage, is the basic ac Josephson effect. The modulation frequency,  $\omega_J = 2eV/\hbar$ , is determined only by the chemical potential difference.

The voltage-frequency relation has enabled the Josephson effect to contribute to

the determination of  $2e/\hbar$  and the volt [109]. High accuracy is achieved through the conversion of voltages into frequency measurements. The Josephson effect has also played a role in the understanding of BCS transitions, phases of macroscopic quantum systems, and the dynamics of vortex states [110].

Josephson effects may have impact in other quantum systems as well. For example, by measuring a mass current oscillating at a mass-dependent frequency, Josephson effects in atomic gases may aid in efforts aimed at detecting a BCS transition in Fermi systems [111]. The measured frequency might be observed to change at the transition point due to a doubling of the effective particle mass through atom pairing.

### 7.3 General approach

Our experiment involved the creation of a  $^{87}\text{Rb}$  BEC in a TOP trap [47] and the subsequent transfer of the BEC to a one-dimensional periodic potential formed by a vertically oriented standing wave of far-detuned laser light [28, 77, 112]. To create the standing wave, we used a retro-reflected laser beam, hence the potential had a periodicity of half of the laser wavelength  $\lambda$ .

The depths of the potential wells were determined by the intensity in the laser beam. We loaded a subset of the potential wells with atoms from the BEC, forming an array of atom traps with initially identical relative macroscopic phases. Because the standing wave had a vertical orientation, the gravitational potential energy difference between adjacent potential wells created a difference in chemical potentials. In our experiments, the depths of the wells had maximum values of  $\sim 2.1E_R$ , where  $E_R = \hbar^2 k^2 / 2m$  is the photon recoil energy, with  $k = 2\pi/\lambda$ . For potential depths of this magnitude, only one bound state existed in each potential well.

Our configuration was similar to a superconducting Josephson junction. The main differences were that we used macroscopic quantum states composed of neutral atoms instead of Cooper pairs of electrons, and that we had an array of such states separated by potential barriers, instead of just two states. The goal of our experiment was to observe a periodic atom current due to the temporal interference of the macroscopically filled states in the trap array. Additional discussion of the relationship between

our experiment and the Josephson effect is given in Appendix B.

## 7.4 Atomic tunnel array: theory

As was the case for superconductors, we begin our theoretical analysis by writing the macroscopic wavefunction for a BEC as  $\Psi = n^{1/2}e^{i\phi(t)}$ . In this case,  $n$  is the number density of atoms in the condensate. With a vertically oriented array of such quantum states, the wavefunction that describes the  $q^{th}$  lattice state is given by  $\Psi_q = n_q^{1/2}e^{i\phi_q(t)}$ . Again,  $n_q$  is determined by the single particle wavefunction and the number of atoms in the  $q^{th}$  lattice state. Now, however, the macroscopic phase  $\phi_q(t)$  depends upon the initial relative phase at time  $t = 0$  and the gravitational potential energy at the  $q^{th}$  lattice site.

### 7.4.1 Model system

The array of atom traps can be modeled as an array of emitters of de Broglie waves when tunneling is considered. The traps at positions  $z_q^0$  emit waves which then travel in a continuum, accelerating with the pull of gravity (the effect of the lattice is neglected after tunneling) out of trapped states. The rate of emission is proportional to the tunneling probability of atoms out of the lattice array potential wells, and depends upon the potential depths of the traps. The energy  $\hbar\omega_q$  of each wave depends upon the lattice site from which it was emitted, with a chemical potential difference of  $\hbar\omega_J = mg\lambda/2$  between adjacent wells ( $m$  is the mass of an atom). The momentum gained by each wave depends upon the distance over which it has traveled, and is given by  $\hbar k_q = m\sqrt{2g|z - z_q^0|}$ , where  $z$  is the spatial coordinate. The relative phase of each wave depends upon the initial phase  $\phi_q^0$  of the emitter at time  $t = 0$ .

The wavefunction of the total array output can then be written as a sum of the output of  $N$  emitters:

$$\Psi(z, t) = \sum_{q=1}^N A_q(t) \exp[i \int (k_q dz - \omega_q dt + \phi_q^0)]. \quad (7.8)$$

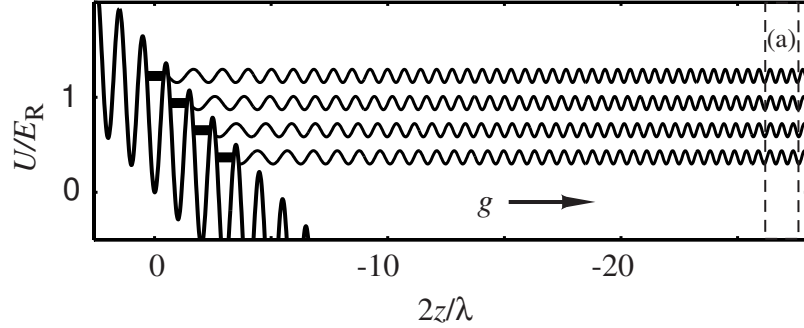


Figure 7.1: The effective optical plus gravitational potential  $U/E_R$  for our experimental parameters, where  $E_R$  is the photon recoil energy. De Broglie-wave output is represented by horizontal waves. The output constructively interferes in region (a). Bound states of the potential are represented by heavy lines. Excerpted with permission from B. Anderson and M. Kasevich, *Science* **282**, 1686 (1998). Copyright 1998 American Association for the Advancement of Science.

Here,  $A_q(t)$  parameterizes both the initial wavefunction amplitude (number of atoms) and depletion of the  $q^{th}$  lattice state due to tunneling. Because the chemical potential differences of the lattice states in this model are discretized in units of  $\hbar\omega_J$ , the probability of atom detection at a point below the array will be periodic in time. In other words, this model predicts the periodic detection of groups of atoms due to periodic constructive interference of the emitted de Broglie waves. Figure 7.1 depicts a sloping periodic potential with de Broglie wave emission from a set of the emitters in the lattice array. At points where the waves are in phase, a pulse is formed.

In this respect, the output of the atomic tunnel array is analogous to the output of a mode-locked laser [113], in which a set of frequencies spaced at regular frequency intervals is generated within a laser cavity. The emitted frequency modes have a definite linear phase relationship. At points where the emitted waves are in phase, constructive interference causes the formation of a pulse of light, similar to the model presented above for the atomic tunnel array. However, if a random phase relationship exists between the modes, pulses will not form. Rather, a semi-continuous output is obtained due to the inability of the modes to properly add coherently. Similarly, in the atomic tunnel array model, random initial phases for  $\phi_q^0$  prohibit the formation

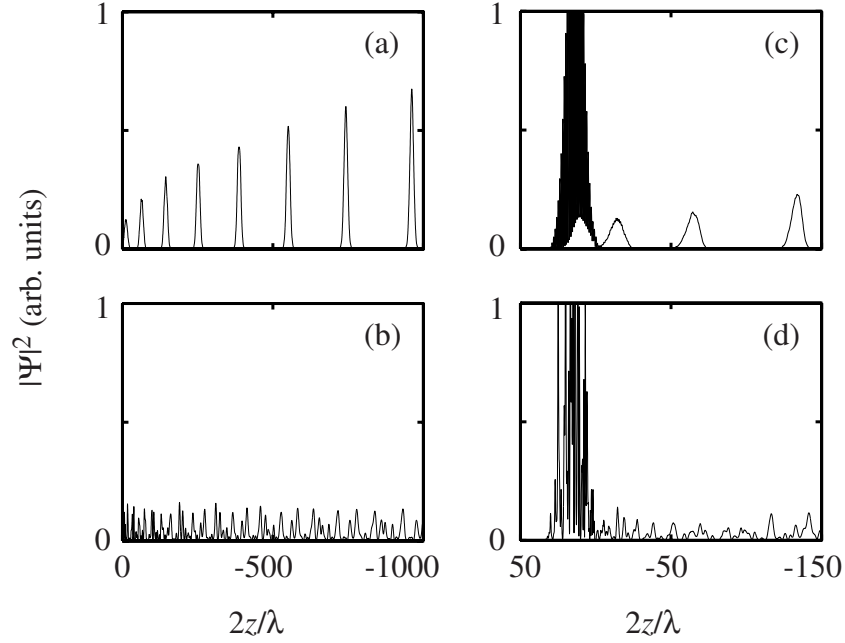


Figure 7.2: (a) Output from the tunnel array model (Eq. 7.8), evaluated at 10 ms. Initial phases are identical. The tunnel array source, not shown in the plot, is located immediately to the left of the  $z = 0$  point. (b) Model output for random initial phases. (c) Numerical solution to the Schrödinger equation showing the confined wavefunction and three output pulses. (d) Numerical solution for random initial phases. Excerpted from Ref. [31].

of periodic atom pulses at the expected frequency.

Sample computed output from the tunnel array model is shown in Fig. 7.2(a), calculated for a set of 30 traps, or emitters. Although depletion of the traps is neglected in the calculation, the initial amplitudes of the wells are given a Gaussian envelope distribution. The amplitude of each pulse increases with time as the spatial pulse width narrows. The widths of the pulses depend upon the number of wells used in the calculation — more lattice sites produce narrower pulses. If random initial phases are used in the calculation, pulses no longer form, as shown in Fig. 7.2(b).

### 7.4.2 Quantum calculation

A quantum-mechanical calculation to determine the tunnel array behavior at temperatures close to zero would involve finding the solutions to the Gross-Pitaevskii equation [114]. However, in a periodic potential of the geometry described above, and for low enough atomic densities ( $\sim 10^{13} \text{ cm}^{-3}$ ), mean-field interaction energies are much smaller than the bound state energies of atoms in the potential wells. To a good approximation, the behavior of the atomic tunnel array can then be calculated with the time-dependent Schrödinger equation (TDSE), neglecting mean-field effects. We solve the TDSE using standard numerical methods [115]. We take the initial wavefunction to be the sum of individual wavefunctions, each with a Gaussian density distribution and a specified initial relative phase. The individual wavefunctions are initially centered at the lattice sites. The width of each state is determined by the ground state energy of a harmonic oscillator which best approximates the shape of an individual potential well in the array. The depths of the wells are  $\sim 1.4E_R$ . At this potential depth, only a single bound state exists in each well, as depicted by the heavy lines in Fig. 7.1.

The total probability distribution from a sample calculation is shown in Fig. 7.2(c) for 30 populated wells. The initial phases of the lattice states are identical, and the initial amplitudes correspond to a Gaussian envelope distribution. Three pulses are shown falling from the oscillating source. Figure 7.2(d) shows the result of a similar calculation with random initial phases. The calculations confirm the validity of the tunnel array model, displaying the same behavior that the model predicts. With these calculations, we verified the accuracy of the assumption that the lattice has a negligible effect on the pulses in the continuum.

The calculations also graphically show a link between the Bloch oscillations [116, 117] of the confined wavefunctions and the formation of pulses, shown in detail in Fig. 7.3. Upon numerically solving the Schrödinger equation, the center of mass of the total wavefunction is observed to undergo longitudinal spatial oscillations with a frequency of  $\omega_J$ . At the turning point of each oscillation, a fraction of the wavefunction continues to propagate in the direction of gravity, forming a pulse.

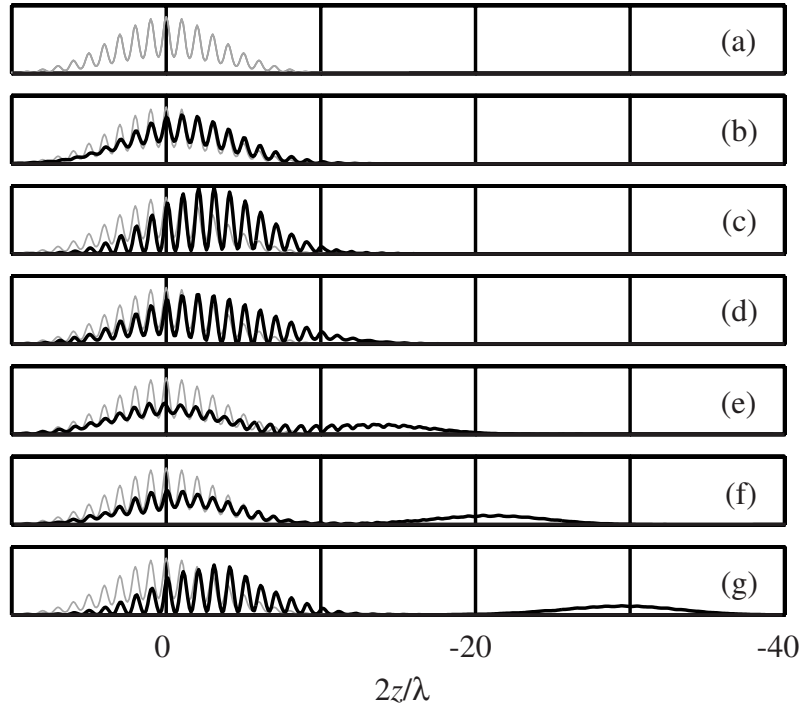


Figure 7.3: Time development of the wavefunction in the periodic potential. (a) The initial wavefunction is shown in gray. The oscillating wavefunction, in black, is shown at times (b)  $T_J/4$ , (c)  $T_J/2$ , (d)  $3T_J/4$ , (e)  $T_J$ , (f)  $5T_J/4$ , and (g)  $3T_J/2$ .  $T_J$  is the Josephson oscillation period,  $T_J = 2\pi/\omega_J$ . For reference, the position of the initial wavefunction is shown in gray in all plots. The plots show the oscillations and depletion of the total wavefunction and pulse formation.

### 7.4.3 Interband tunneling

The formation of pulses can be viewed as interband tunneling at the turning point of a Bloch oscillation, as described by Zener for dielectric breakdown in metals [117]. Zener considered a multiple energy band lattice with a linear potential gradient created by an external field. The field induces oscillations of the confined energy states of the periodic potential, and the highest probability of tunneling to the next higher lying energy band occurs at the diffraction point of a Bloch cycle. In our case, atoms confined to the lowest energy band (the trapped atoms) will oscillate at the Bloch frequency  $mg\lambda/2\hbar$ , identical to the Josephson frequency  $\omega_J$ . The gravitational field induces tunneling into the next higher lying state (the unbound continuum). Analogous to the calculations of Zener, the tunneling probability per oscillation for our lattice is given by

$$P = \exp\left(-\frac{\lambda\epsilon^2}{8\hbar^2g}\right), \quad (7.9)$$

where  $\epsilon$  is the energy gap between the ground state energy band and the continuum states. Not only is this picture consistent with the solution of the Schrödinger equation as described above, but it suggests that atom pulses are a direct indication of an oscillating atom current flowing between the lattice sites, and thus that pulses are a signature of a type of Josephson effect.

For the parameters used in our experiment, the assumption that atoms are confined to single wells is not entirely accurate. In a periodic potential without an external force, the energy eigenstates of the system are the Bloch states. When a potential gradient is applied, the Bloch states undergo coherent oscillations, with wavepackets remaining confined to a single energy band. Such oscillations have been previously observed for non-degenerate atoms trapped in an optical standing wave [81]. The Wannier-Stark states  $\psi_p$  [118, 119] form an alternative but equivalent basis to the Bloch states. Each state is a superposition of localized Wannier (tight-binding) states  $w_q$ :  $\psi_p = \sum_q J_{q-p}(4T/mg\lambda)w_q$ , where  $J_n$  is the  $n^{\text{th}}$  order Bessel function and  $T$  is the tunneling matrix element between lattice sites. For our parameters, each lattice state has a spatial extent that covers a small cluster of potential wells, with most of the atoms of each state concentrated at the central lattice site. Pulsed atom output is still



expected; however, for simplicity in our calculations and in the physical descriptions, states were assumed to localize to single lattice sites.

## 7.5 Trapping a BEC in an optical lattice

To create a BEC, we used the methods described in Chapter 6. After loading  $\sim 10^8$  atoms into a magneto-optic trap, the trapped atoms were optically pumped into the  $F = 2, m_F = 2$  Rb ground state, loaded into a TOP trap, and evaporatively cooled to create a condensate using ramping rf and confining magnetic fields. We typically created nearly pure condensates of  $\sim 10^4$  atoms with radial sizes of  $\sim 8\mu\text{m}$  [30].

To create the 1-D optical potential, we retro-reflected a vertically oriented  $\lambda = 850\text{-nm}$  laser beam, as depicted in Fig. 7.4. The beam created a series of potential wells centered at the anti-nodes of the standing wave with a spacing of  $\lambda/2$ , as illustrated in Fig. 7.5. The beam was focused to a  $1/e^2$  beam waist of  $\sim 80\mu\text{m}$  (radius), with maximum intensities of  $\sim 80\text{ W/cm}^2$ . The maximum depths of the wells were  $\sim 2.1 E_R$ , only enough to support a single bound state. The large detuning of the beam (70 nm red-detuned from the 780-nm Rb transitions) gave a photon scattering rate of less than  $0.01\text{ s}^{-1}$ .

To load the condensed atoms into the potential wells, the spring constants of the magnetic trap first had to be relaxed, as they were before imaging a BEC. The control of density and size of the BEC allowed for adjustment of the number of wells loaded and the densities (and hence mean-field interactions) of the atoms in the wells. After the adiabatic relaxation, the standing wave potential was ramped on (using an acousto-optic modulator) in  $\sim 20\text{ ms}$ . At this point, the standing wave overlapped the magnetically trapped BEC. The dc component of the TOP trap was then turned off, while the rotating component remained on to maintain the spin polarization of the atoms, completing the transfer of atoms into the optical lattice.

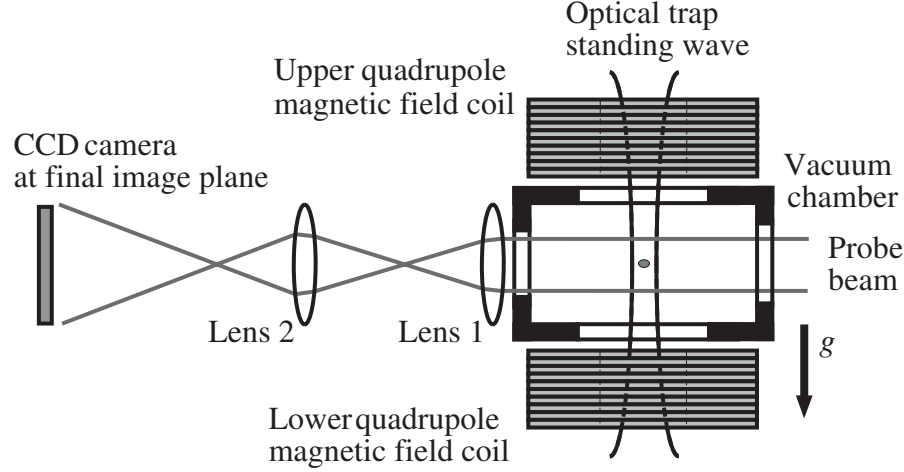


Figure 7.4: The experimental setup, showing the retro-reflected trapping laser propagating through the vacuum chamber. Excerpted from Ref. [31].

## 7.6 Atomic tunnel array: observations

In this section, we describe observations of the dynamics of the atomic tunnel arrays. The distributions of atoms were observed with absorption imaging. For observations that were made as a function of time, a new BEC and tunnel array were created for each time step due to the destructive process of absorption imaging. In the following descriptions, a high-intensity lattice refers to trap depths of  $\sim 2.1E_R$ , and a low-intensity lattice refers to trap depths of  $\sim 1.4E_R$ . We typically loaded about 30 potential wells, with up to  $\sim 1000$  atoms per potential well.

### 7.6.1 Low Intensity lattice

When we turned on the optical trap at a low intensity, we observed pulses of atoms falling from the trap, as shown in Fig. 7.6 for various time delays. Images (b)-(e), with identical intensity scales, show saturated images of the lattice array in order to highlight the pulses. For comparison, Fig. 7.6(a) shows an unsaturated image of a magnetically trapped BEC. Due to limits in optical resolution, individual lattice sites

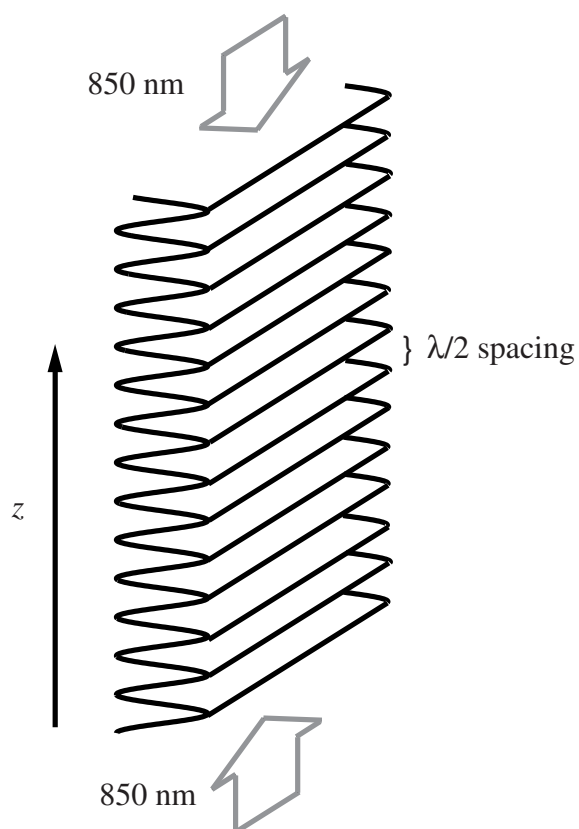


Figure 7.5: An illustration of the vertical periodic potential (oscillating lines) formed by the ac Stark shifts of the retro-reflected optical trapping beams (arrows).

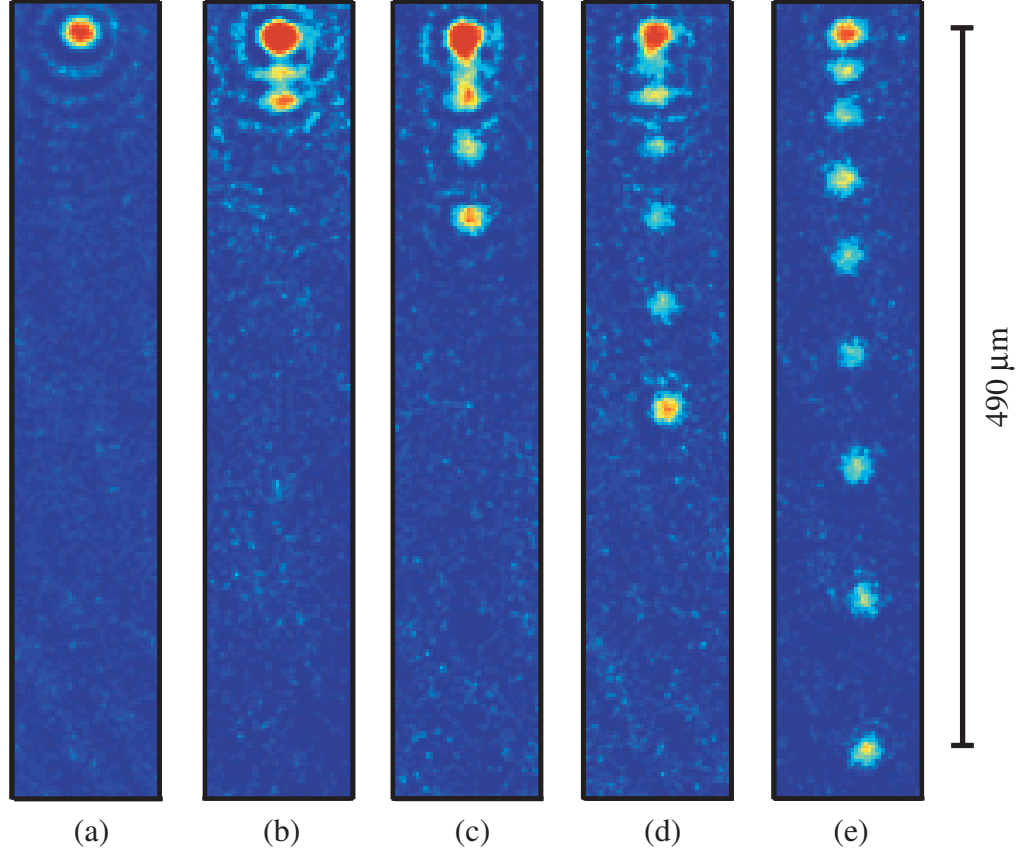


Figure 7.6: (a) Absorption image of a BEC in a weak TOP trap. (b)-(e): Absorption images taken after transferring the atoms into the optical lattice and allowing (b) 3 ms, (c) 5 ms, (d) 7 ms, and (e) 10 ms of tunneling. Excerpted from Ref. [31].

are not resolvable. In each of images (b)-(e), the pulse at the lowest part of the image was the first emitted pulse. The last emitted pulse was not resolvable from the image of the trap array.

The measurement of Fig. 7.6(e) was made 10 ms after the atoms were loaded into the optical trap. Each pulse contained  $\sim 1000$  atoms. The output of the tunnel array was similar to the output expected based on our model and calculations. We measured the spatial separations of the pulses in the images, and with a value of  $9.8 \text{ m/s}^2$  for  $g$ , we inferred the time intervals between the pulses. The measured period

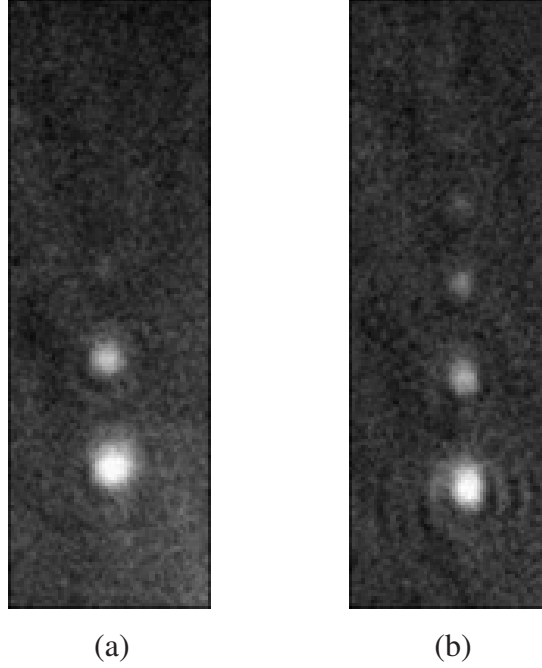


Figure 7.7: Atom pulses were observed for trap depths of  $\sim E_R$ , where bound states are not well defined.

of  $1.10 \pm 0.05$  ms agreed well with the expected value of  $T_J = 2\pi/\omega_J = 1.09$  ms. The uncertainty in the measurement was limited by the uncertainty in the calibration of the imaging system. Pulses were also observed for less intense optical traps of  $\sim 1 E_R$ , as shown in Fig. 7.7. In these cases, the tunnel array was depleted more quickly, with more atoms per pulse but fewer pulses. The pulse frequency however remained the same. Because well defined bound states should not exist at this trap depth, the pulses were possibly the result of above-barrier quantum reflections.

We integrated over the transverse absorption profile of Fig. 7.6(e) to produce the cross section shown in Fig. 7.8. We fit the cross section with a series of Gaussian distributions constrained to be periodic in time, resulting in a measurement of  $9.6 \pm 0.4$  m/s<sup>2</sup> for  $g$ , with the error again dominated by imaging calibration uncertainty. The measurement resolution was  $\delta g \sim 10^{-4}g$ , or  $\delta g \sim 10^{-5}g/\sqrt{Hz}$  for the 10-ms measurement. The accuracy of the measurement might be improved by using

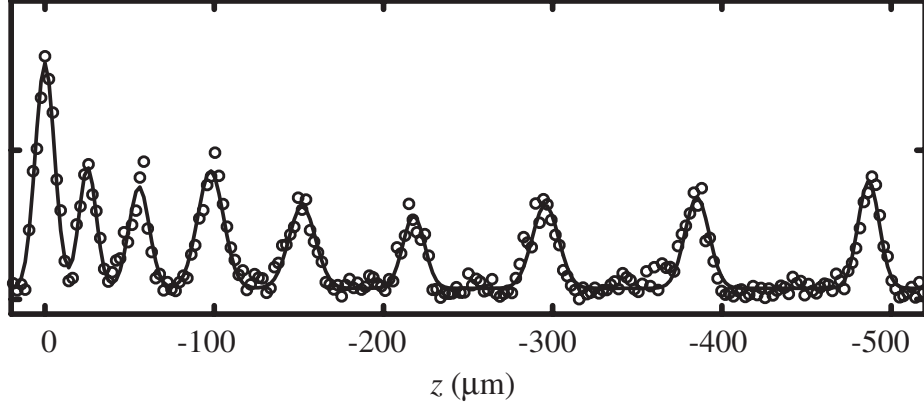


Figure 7.8: The integrated absorption cross section for Fig. 7.6(e), obtained by summing over the horizontal profile. The circles are the data. The solid line is a non-linear least squares fit to a series of Gaussian pulses, constrained to be separated by a fixed time interval, with  $g$  as a fitting parameter. Excerpted from Ref. [31].

a resonant probe laser beam and fluorescence detector to determine the temporal distribution of the atom pulses, thereby eliminating uncertainties due to the imaging system. The resolution of the measurement may also be enhanced by generating pulses at higher frequencies. This could be accomplished by increasing the trapping laser wavelength, using a different laser beam geometry, or by combining standing waves of different frequencies to form a super-lattice.

### 7.6.2 High-intensity lattice

When we loaded the atoms into the high-intensity lattice, we measured trap lifetimes of  $\sim 50$  ms, much shorter than would be expected due to 3-body recombination [120] or to off-resonant photon scattering. However, the lifetime is consistent with tunneling time estimates based on our numerical calculations and the tunneling probability formula of Eq. 7.9 for  $\epsilon \sim E_R$ . Pulses of atoms were not observed in this case, possibly due to a relatively low number of atoms per pulse.

### 7.6.3 Hold and Release

In this experiment, the BEC was loaded into a high-intensity lattice and held for a variable time ( $\sim 5$  ms) before the lattice was suddenly turned off. The atom distribution was measured after a subsequent 5-ms of ballistic expansion. Because of the Fourier relationship between the spatial and momentum distributions of a ground state wavefunction, the ballistic expansion images provided a measurement of the momentum distribution of the trapped atoms as well as information about the initial spatial confinement of the atoms. To model the ballistically expanding atom wavepackets, we assumed an initial set of traps with the distribution of atoms localized to  $\sim \lambda/4$  within each well (minimal coupling). The number of atoms in each well was determined by the position of the well in a Gaussian envelope distribution encompassing all of the wells. The Fourier transform of this spatial distribution is a set of wavepackets distributed over momentum-space. The  $2\hbar k$  spacing between the momentum-space wavepackets is determined by the  $\lambda/2$  spatial separation between the traps. The widths of the wavepackets are identical, and are determined by the number of traps in the spatial distribution.

For the case where the macroscopic phases of the released traps are identical, the number of momentum-space wavepackets that can be observed is determined by the initial spatial localization of the individual traps. For our experimental parameters (trap localization of  $\sim \lambda/2$ ), this corresponds to a single peak in the momentum distribution. Tighter confinement within each well, with the same periodicity, would produce more visible momentum peaks (via the Heisenberg uncertainty relations). Weaker confinement would produce a single momentum peak, but the width of the peak would broaden. If the initial phase differences between adjacent traps are  $\pi$ -rad, then two peaks will be observed with a separation of  $2\hbar k$ . Figure 7.9 shows the expected velocity distributions for atoms released from an optical trap with  $\sim 30$  wells loaded, with spatial localization of  $\lambda/4$ . The relative phase difference between adjacent wells is listed for each plot. Figure 7.10 shows the velocity distributions for various confinements and numbers of wells loaded, with  $\pi$ -rad phase shifts between adjacent wells.

Experimentally, when we let the trapped atoms ballistically expand after a fixed

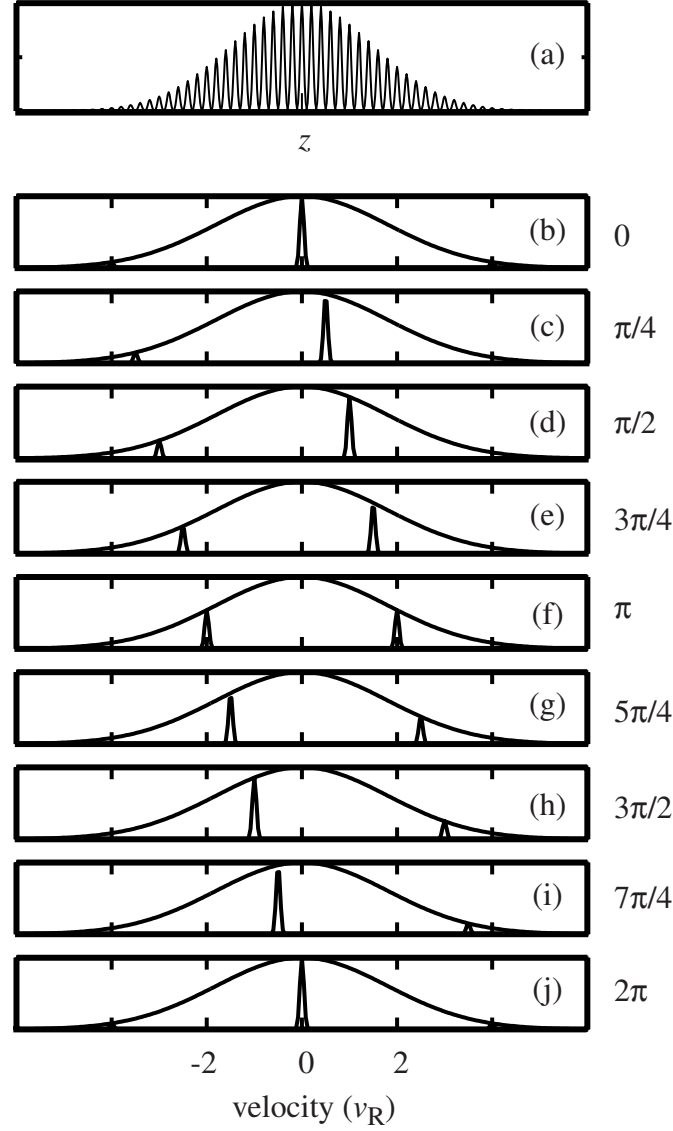


Figure 7.9: (a) The simulated spatial distribution of atoms in the optical trap before release. The plot shows a spatial localization of  $\lambda/4$  for the traps, which are separated by  $\lambda/2$ . Plots (b)-(j) show the velocity distribution for the relative phase differences listed by each plot. The broad Gaussian distribution in these plots is a relative momentum peak envelope distribution, which grows in width with tighter initial confinement, revealing more velocity peaks separated by  $2v_R$  ( $v_R = \hbar k/m$ ).



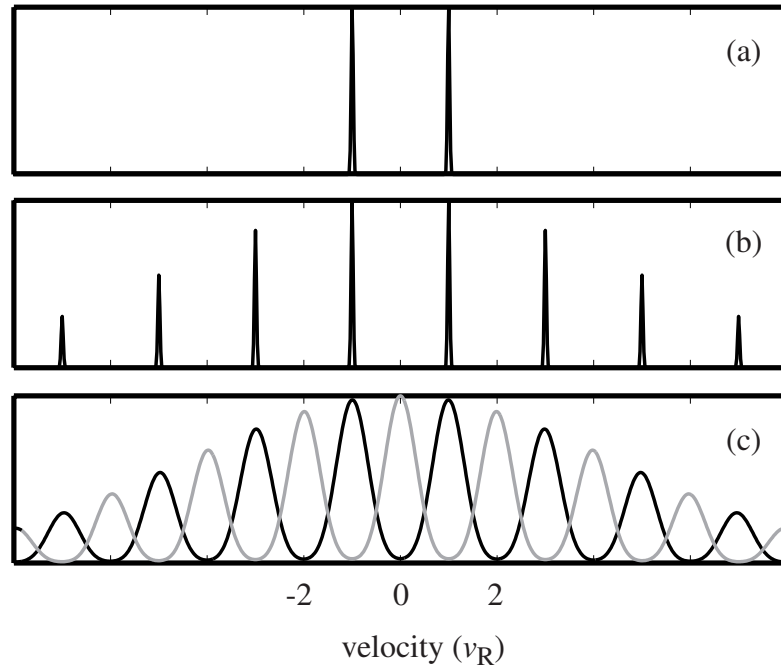


Figure 7.10: The calculated velocity distribution for traps with (a)  $\lambda/2$  spatial localization of the wells, and 30 wells loaded, (b)  $\lambda/20$  localization and 30 wells loaded, and (c)  $\lambda/20$  localization and 2 wells loaded with  $\pi$  rad phase shifts between wells (dark line) and 0 rad shifts (gray line). This last case is similar to the case of usual 2 slit diffraction.

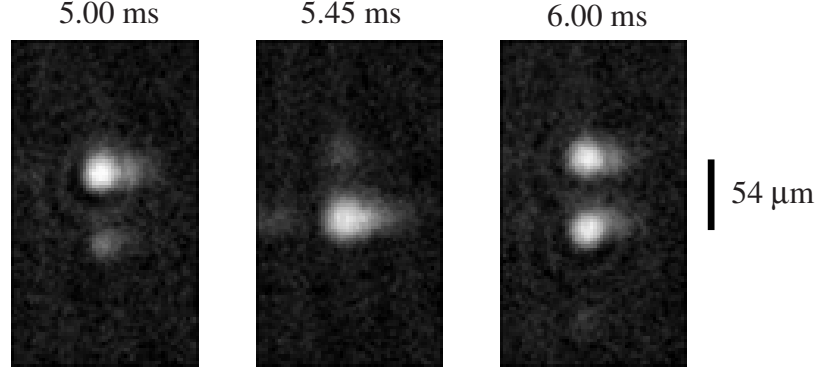


Figure 7.11: Time of flight absorption images, after 5 ms of ballistic expansion. The atoms were held in a high-intensity lattice for the times shown, then released.

holding time in a high-intensity lattice, we observed a single prominent momentum peak and a single minor peak after 5 ms of expansion. The distribution of atoms among momentum components varied with the relative phases of the atoms as they were released from the traps. The relative phases evolved with time due to the differences in gravitational potential energy. As we increased the time that the atoms were held in the optical trap and then observed the time of flight pattern, one of the peaks grew in amplitude while the other decreased until one peak remained. As holding time increased further, two peaks were observed in the distribution. The separation was  $\sim 54 \pm 4 \mu\text{m}$ , agreeing well with the expected separation of  $2v_R \cdot (5 \text{ ms}) = 54 \mu\text{m}$ . This process was a signature of the time-domain interference of the macroscopic states of the source. Figure 7.11 shows the observed time of flight patterns for three hold times.

#### 7.6.4 Dephasing and loss of coherence

We expected the phase coherence of the lattice array states to be lost due to the mean-field interaction of the atoms. At potential well depths of  $1.4E_R$ , we calculated a mean-field energy of  $\sim 4k_B \cdot \text{nK}$  for our peak densities ( $\sim 10^{13} \text{ cm}^{-3}$ ), much less than the  $\sim E_R = 157 k_B \cdot \text{nK}$  kinetic energy of atoms in the traps. Nevertheless, the mean-field

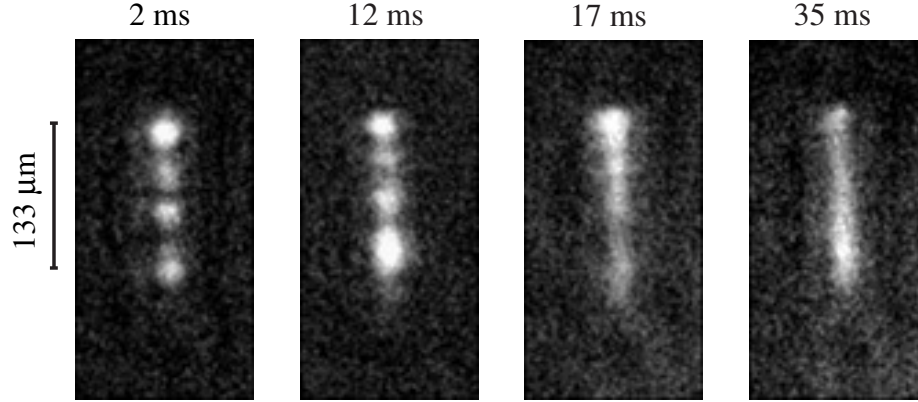


Figure 7.12: Tunnel array output, imaged after 5 ms of tunneling, showing the loss of phase coherence of the trapped atoms. Before inducing tunneling by dropping the intensity of the lattice, the atoms were held at high intensity for the times shown.

interaction will shift the chemical potentials of the trapped atoms by an amount that depends upon the density of atoms in each well. For our parameters, this corresponds to a maximum frequency shift of 80 Hz for the ground state energies. The maximum *relative* frequency shift is 4 Hz between adjacent wells. The result of a frequency shift is a dephasing of the array output due to slight variations in the oscillation frequencies of the tunneling currents. The timescale over which this dephasing happens should be proportional to the density of the traps. For our densities in the low-intensity traps, we did not expect to see signs of dephasing in the 10-ms measurements described above. For higher densities and longer measurement times, we expected dephasing to occur.

We observed dephasing of the tunnel array output by first holding the atoms in a high-intensity trap for a variable amount of time, then by decreasing the potential depths to  $1.4E_R$  in order to induce tunneling. We then imaged the atoms after 5 ms of tunneling in the low-intensity traps. By holding the atoms in a high-intensity trap, the densities of the wells were increased and the timescale for dephasing was shortened, compared to that of the low-intensity traps. The images in Fig. 7.12 show

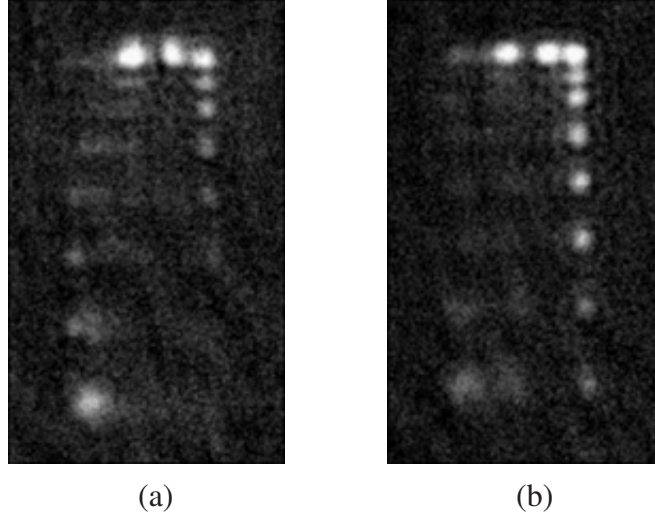


Figure 7.13: Images of multiple-traps in the optical lattice. The lattice split during the optical trap loading procedure, and the separate trap sections independently displayed output pulses.

a comparison of pulsed output and dephased output showing a loss of coherence, observed after various holding times in a strong lattice. The dephased output was qualitatively similar to the model output for random initial phases of the lattice states.

### 7.6.5 Multiple traps

We occasionally obtained multiple transverse traps visible in the absorption images during the alignment procedure due to intensity variations in the transverse beam profile on top of a smooth Gaussian distribution. These variations were due to back-reflected light from the vacuum chamber viewport surfaces. These multiple-traps would also undergo pulsing. Examples of such images are shown in Fig. 7.13.

Perhaps these traps can be thought of as a type of 2-dimensional lattice, or a transverse array of atomic tunnel arrays. These images suggest ideas of future experiments, where interference of pulses from adjacent arrays may be observed. When we observed the traps created with a particular beam alignment, we observed a time

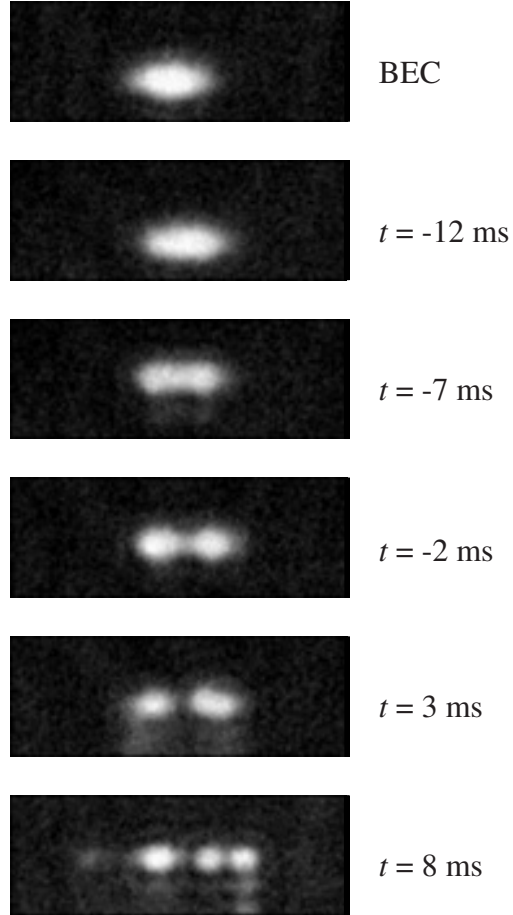


Figure 7.14: A sequence of images showing the formation of multiple transverse traps. The magnetic trap turns off at  $t = 0$  ms. The lattice starts ramping on at  $t = -20$  ms. Note that in the final image at  $t = 8$  ms, the trap section on the left side of the image has been nearly depleted due to tunneling (as in Fig. 7.13).

dependence in the number of horizontally distributed traps, shown in Fig. 7.14.

### 7.6.6 Launching pulses upwards

Figure 7.15 shows an example of a force other than gravity used to create the atom interference in the tunnel array. For this image, a BEC held in a magnetic trap was overlapped with the optical standing wave at low intensities. However, instead of turning off the harmonic trapping potential, the bottom of the potential well was shifted vertically upward to a strength that applied a force approximately equal to the force of gravity but in the opposite direction. The energy gradient was approximately equal over the length of the tunnel array.

The potential well was shifted by reducing the strength of the rotating TOP bias field by a factor of 2, thereby increasing the trap spring constants and shifting the center of the oscillator. For the trap strengths used, the minimum of the potential well was shifted upwards by  $137 \mu\text{m}$ .

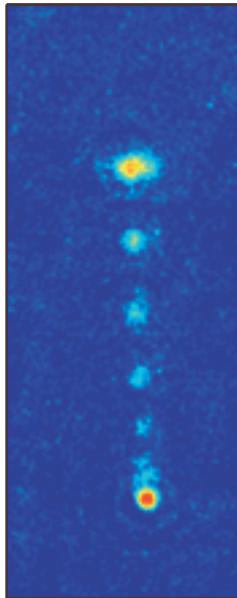


Figure 7.15: Atom pulses launched upwards due to the force of a magnetic field gradient instead of gravity. Image dimensions:  $200 \mu\text{m}$  horizontal by  $500 \mu\text{m}$  vertical.

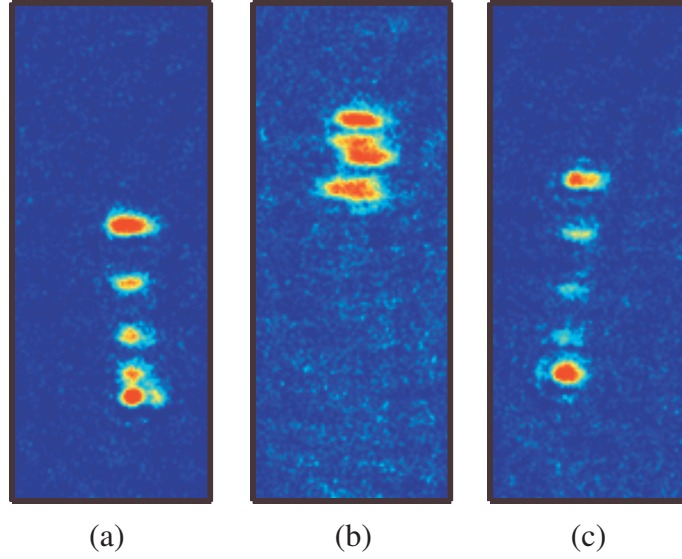


Figure 7.16: Atom pulse train in the harmonic potential well of a magnetic trap. (a) Pulse train on initial fall upwards in harmonic trap. (b) Pulse train with all pulses near upper turning point. (c) Pulse train returning to lower turning point in trap. All images  $200\ \mu\text{m}$  horizontal by  $500\ \mu\text{m}$  vertical.

### 7.6.7 Pulses in a harmonic potential

Using the same technique as used to launch pulses upwards, atom pulses were also observed oscillating in a harmonic potential. After the minimum of the magnetic potential well was shifted upwards, the trapped atoms were held for 5 to 10 ms while atom pulses “fell” (upwards) in the harmonic potential. Then the optical standing wave was removed, and the entire pulse train oscillated in the magnetic trap at the trap frequency. Figure 7.16(a) is an image showing the pulse train as it is initially falling upwards in the trap. Figure 7.16(c) shows the pulse train after  $\sim 30$  ms, as it is approaching the lower turning point of the trap, where each pulse originated. Note that the upper groups of atoms in Fig. 7.16(a) have turned around first and are the lower groups on atoms in Fig. 7.16(c), indicating that these groups of atoms have passed through each other near the upper turning point. Figure 7.16(b) shows the pulse train near this point in time.

## 7.7 Atomic tunnel array: applications

### 7.7.1 Measurements of weak forces

One application of tunnel arrays might be realized in the measurements of weak forces. As we demonstrated with a measurement of  $g$ , the tunnel array can be used to make an ac measurement of a dc force, thereby increasing measurement resolution. For example, a tunnel array near a surface may provide a means of measurement of Van der Waals/Casimir forces.

We can also estimate the potential resolution that could be obtained in a measurement of  $g$ , under ideal conditions. Assuming two condensates separated by 1 cm, an observation of a 1 rad phase shift after 100 s of tunneling between the traps would give an acceleration resolution of  $7 \times 10^{-11}g$ . With  $10^8$  atoms in the array, the resolution is increased by a factor of  $\sqrt{10^8}$ , giving a measurement resolution of  $7 \times 10^{-15}g$ , or  $7 \times 10^{-14}g/\sqrt{Hz}$ . The best commercial accelerometers currently have a resolution of  $10^{-11}g/\sqrt{Hz}$ . If instead we have a tunnel array with a spatial extent of 1 cm, the analysis is complicated by the spatial structure of the array. We can estimate that the accuracy of a measurement of  $g$  will nevertheless be comparable to the above analysis, due to an equivalent total gravitational energy (phase) shift across the extent of the array. Phase-spreading due to mean-field interactions would degrade these resolution estimates, and would need to be considered in a more rigorous analysis.

### 7.7.2 BEC optical trapping experiments

Tunneling dynamics of an array should be considered in experiments aimed at trapping a BEC in an optical lattice with a force (such as gravity) present. At trap depths such as the ones described here, tunneling is certainly important. However, even deeper traps may have interesting tunneling resonances for certain configurations: tunneling might for example proceed from the lowest bound state of one well to the second bound state, at the same energy, of another well. In this manner, it is conceivable that atoms may be quickly lost from the trap, or may undergo oscillation dynamics.



The atom arrays might also be an interesting test of Cooper pairing in a superfluid Fermi system, when such a system is produced. A superfluid Fermi system may undergo pulsing tunnel dynamics (Josephson type effects for particle pairs) as mentioned at the end of section 7.2. However, above the BCS transition, the tunneling dynamics should be quite different.

### 7.7.3 Atom laser

The atomic tunnel array can be considered a source of coherent matter-wave or “atom laser” [102] output. As we have discussed, atom pulses from an array can be modeled similarly to pulses of a mode-locked laser. In this respect, the pulsed output that we have observed is a demonstration of a “mode-locked atom laser.” The initial mode-locking is manifested by loading the entire array of traps from a single BEC, ensuring a definite phase relationship between the array of states. Estimates of the phase-space densities of the pulses that we observed, based on number of atoms per pulse and pulse velocity spread, indicate that the pulses are in the quantum degenerate regime. Additionally, the observation of periodic pulses is an indication of the coherence length of the array output. We conclude that the coherence length of the atom laser is  $> 500\mu\text{m}$ , much larger than the dimensions of the resonator (the array). The output of the atom laser may be envisioned as playing a role in the transport of degenerate groups of atoms for use in applications such as nano-fabrication or possibly in loading a steady-state BEC confined to a trap in a different region in space.

## 7.8 Future improvements

The experiments of atoms trapped in optical lattices can be enhanced with improvements to the condensate creation methods described at the end of the previous chapter. Some planned improvements however are specific to the optical trapping experiments.

The most obvious improvement to the system is to obtain the ability to use deeper potential wells. This would be beneficial for experiments with the goals of observing

long holding times in the lattice, and for studies of mean-field interactions where densities are higher and atoms more localized in stronger traps. Deeper traps would be needed to reach the higher precision measurements of  $g$  mentioned in section 7.7.1, where long holding times would be needed to make observations of many periods of the tunnel output (thereby increasing resolution).

Another improvement would be the use of a resonant probe beam situated below the trap. Falling pulses of atoms would scatter light from the beam as they fell through the beam. The scattered light would be collected and focused onto a detector, recording the arrival times of the atoms in the pulses. Such a probe beam setup would allow possible quantum statistical measurements by measuring the arrival times and positions of individual atoms in the pulses as they fell through the beam. This could also enable unique measurements of collective radiation effects of degenerate atoms, such as superradiance.

Although the optical trapping beam was spatially filtered, the quality of the wavefront should be further improved. The vacuum chamber windows that the light passed through reflected  $\sim 15\%$  of the light, possibly contributing to difficulties in alignment of the retro-reflected beam to positions where high-quality traps were observed. By improving the beam quality, possibly by replacing the windows with ones anti-reflection coated at 850 nm, the multiple-trap images should also disappear.

## 7.9 Summary

We observed periodic pulsed atom output from atoms trapped in an optical lattice. The pulsed output from our atomic tunnel array can be described using the principles of the Josephson effect, and are additionally a demonstration of a mode-locked atom laser. For further elaboration and clarification of our interpretation of Josephson effects, refer to Appendix B. The subject of Bose-Einstein condensates trapped in optical lattices is rich with possible experiments and potentially useful applications. The observation of pulses in this experiment is yet another link between the physics of superfluids and superconductors and Bose-Einstein condensation in a dilute atomic gas.

# Chapter 8

## Conclusions

We have demonstrated that Bose-Einstein condensed atoms can display unique and interesting characteristics when trapped in a periodic external potential. In our experiment, a Bose-Einstein condensate of  $^{87}\text{Rb}$  atoms was transferred from a magnetic trap into a standing-wave optical trap. The optically trapped atoms filled  $\sim 30$  sites in the vertically oriented periodic potential. Because of the acceleration due to gravity and the weak trapping potential, tunneling occurred between the barriers of the optical potential. As a result of the tunneling, the gravitational energy difference between the lattice sites, and the phase coherence of the trapped atoms, pulses containing  $\sim 1000$  atoms were observed falling from the trap at periodic time intervals. The occurrence of atom pulses was due to an interference between the atoms in different potential wells, similar to the ac Josephson effect observed with superconductors. A careful measurement of the pulse period, determined by the gravitational energy difference between the wells, produced a high resolution measurement of the gravitational acceleration of  $\delta g/g \sim 10^{-5}/\sqrt{Hz}$ .

Many additional experimental investigations may be developed using similar atomic tunnel arrays. For example, tunnel arrays and periodic potentials might be used in creating Fock states of large numbers of atoms or in applications of high-resolution measurements of the strength of gravity and gravity gradients. Tunnel arrays may possibly have applications in nano-fabrication, cold-atom transport, optical cooling, experiments where a BEC is constantly replenished from a separate

source, or as a test of BCS pairing in fermionic gases (where a pulse frequency would depend upon the mass of a pair of atoms). The arrays could be used in studies of relative pulse coherence for further development of atom-laser concepts, or in studies of collisions between condensates. Precision measurement techniques could be extended to measurements of  $\hbar/m$  or van der Waals forces, for example. Tunnel arrays certainly merit further study in future investigations.

With our images of condensed atoms in a weak TOP trap, quantitative analysis of condensate parameters could be made with *in situ* imaging techniques. With a high enough imaging resolution, the measured parameters may be compared with developing theories. The techniques we used to reach condensation included two additional uses for the rotating bias magnetic field of the TOP trap. First, we used a low-amplitude rotating field to increase the number of atoms in a dark MOT. Second, we used the rotating field as our primary method of evaporative cooling. Although TOP-induced evaporative cooling had been previously demonstrated, we showed that it was efficient at cooling atoms to the BEC threshold. We additionally demonstrated the technique of on-resonance dark-ground imaging. Similar high-resolution imaging techniques may contribute to future studies of small-number condensates, and possibly lead to the ability to spatially resolve and detect atoms near the single-atom limit. Such achievements would open up possible experiments with condensates such as measurements of atom-number fluctuations and quantum optics-type experiments with condensates.

In developing the  $^{87}\text{Rb}$  experiment, we found that atom desorption from the inner walls of the stainless steel vacuum chamber could be induced when the walls were illuminated with white light. The process was used to modulate the vapor pressure in the cell. This allowed us to increase the number of atoms in our magneto-optic trap while maintaining long trap lifetimes. The method is applicable to evaporative cooling experiments and possibly to other atomic species. The techniques might, for example, be modified in such a way that atomic beam sources might be replaced with simpler systems using light-induced desorption.

Prior to our Rb studies, we developed techniques for use in studying quantum

many-body effects in lithium. We demonstrated the ability to trap Li atoms in far-off-resonant optical lattices tuned to the red or blue of resonance. We measured adiabatic cooling of the trapped atoms when the trapping spring constants of the optical wells were slowly reduced, and we used the lattice to select atoms with energies slightly below the photon recoil energy. We also measured the loading rate of  $^7\text{Li}$  atoms into a MOT with a Li source located near the MOT. Atoms were directly loaded into the trap without a precooling stage. We showed that this method was comparable to other loading methods. We also demonstrated an increase in the number of atoms loaded into the trap by frequency modulating the laser light used for the trapping beams. The spectrally broadened light let us capture atoms of energies higher than single-frequency trapping light would allow. The result of these two techniques was a relatively simple Li trapping apparatus, with the ability to quickly load large numbers of atoms into a MOT. A modification of these techniques might improve trap loading with species other than Li. Further theoretical study is needed regarding these possibilities.

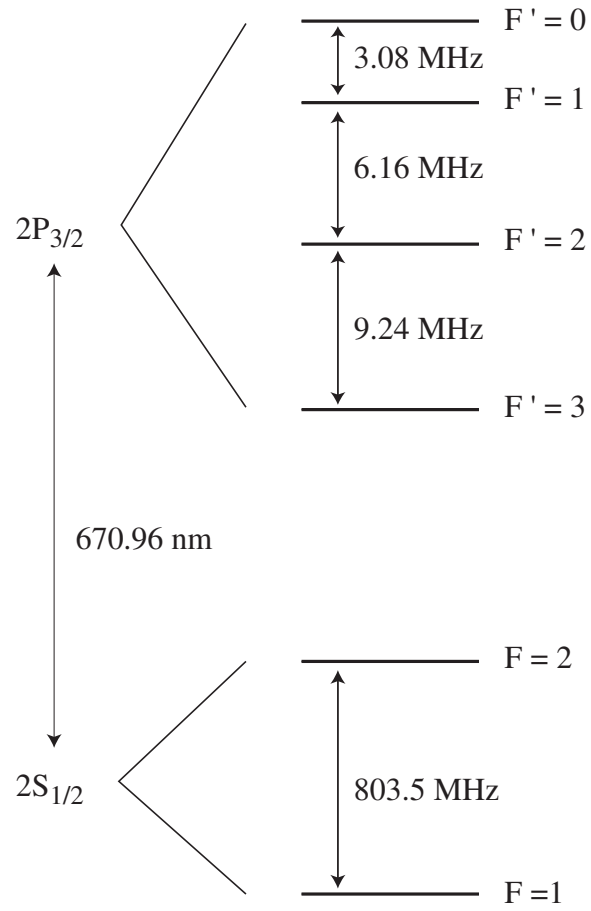
The methods and experiments mentioned above were a result of our efforts to observe quantum many-body effects in Li and Rb. The experiments that we have discussed can be viewed as successful steps forward along the path towards observation of various quantum many-body effects and a better understanding of Bose-Einstein condensation, superfluidity, and the possible development of applications of these physical phenomena.

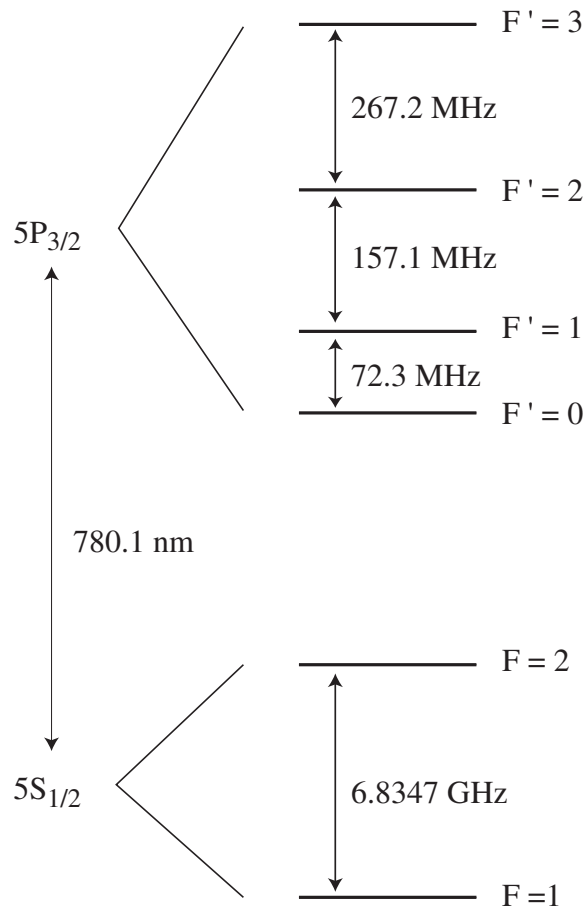
# Appendix A

## Characteristics of $^7\text{Li}$ and $^{87}\text{Rb}$

Property	$^7\text{Li}$	$^{87}\text{Rb}$
cooling transition	$2S_{1/2}, F = 2 \rightarrow 2P_{3/2}, F' = 3$	$5S_{1/2}, F = 2 \rightarrow 5P_{3/2}, F' = 3$
$\lambda$ (nm)	671	780
$m$ (kg)	$1.2 \times 10^{-26}$	$1.5 \times 10^{-25}$
$\Gamma/2\pi$ (MHz)	5.9	5.9
$\tau_n$ (ns)	27	27
$I_{sat}$ (mW/cm <sup>2</sup> )	2.4 (swing transition)	1.6 (swing transition)
$T_D$ ( $\mu\text{K}$ )	146	146
$E_R$ at 671 nm	$k_B \cdot 3.2\mu\text{K}$	
$E_R$ at 780 nm		$k_B \cdot 0.19\mu\text{K}$
$E_R$ at 850 nm		$k_B \cdot 0.16\mu\text{K}$
$\sigma_{scat}$ ( $10^{-9}$ cm <sup>2</sup> )	2.1 (at 671 nm)	2.9 (at 780 nm)

Table A.1: Properties of Li and Rb.

Figure A.1: The energy level structure of  ${}^7\text{Li}$ .

Figure A.2: The energy level structure of  $^{87}\text{Rb}$ .



# Appendix B

## Josephson effects and Bloch oscillations

The distinction between the Josephson effect and Bloch oscillations, especially in regard to our atomic tunnel array experiment, is an issue that must be addressed. Confusion also arises in the interpretation of what has been referred to in this thesis as macroscopic interference, as well as which phenomena may be described as macroscopic interference. This appendix is meant to be a clarification of our views regarding these issues.

As a brief overview of the following discussion, we first note that the physics behind the Josephson effect and Bloch oscillations can be explained by considering single-particle states. Second, in certain configurations, the ac Josephson effect and Bloch oscillations are different labels for the same process, explained using different language and different equations.

We first consider the ground state of a split potential well, with an energy offset between the two segments of the well (we imagine a potential-energy gradient applied to a split potential well. If the barrier between the two sections is high enough, the tunneling rate through the barrier will be low. The energetically lowest two basis states for the entire potential well can then be approximated as one that localizes a particle on the left of the barrier, and one that localizes a particle on the right of the barrier. The energy difference between the sides of the potential determines the

energy difference between the left (L) and right (R) basis states.

With a large (but non-infinite) barrier between the sections, L and R overlap slightly and interfere. With different energies, differences in the phase-evolution rate ( $E/\hbar$ ) between L and R will produce time-dependent interference. This is equivalent to a probability current oscillating between the two sides of the potential well. This explanation also describes the oscillations in the ac Josephson effect. So far, we have not explicitly assumed any restrictions on the number of particles in state L or R, although we have assumed that (i) we can write localized basis states, and (ii) we can speak about a relative phase between the states. These assumptions are valid if the potential wells are separated by a high-enough barrier.

In common usage, the term “Josephson Effect” *implies* interference between macroscopically occupied quantum states. The physics behind the effect is the same as the effect described above for single-particle states, but the language is different. To extend the equations describing the single-particle effect to describing the Josephson effect, we must assume that we can write a macroscopically occupied state as having an amplitude (corresponding to the number of particles in the state) and a relative phase (corresponding to the relative energy of the quantum states). Then there is no difference between the mathematical descriptions of the Josephson effect with a macroscopic wavefunction and the oscillating probability currents of a single-particle state. The difference is in terminology.

However, if interactions between particles are considered, the physics becomes more complicated. The energy of each interfering state can be altered by the number of particles in each state. For example, for the L and R single-particle states in a symmetric double-well potential, there is no oscillating current (this may be interpreted as an oscillation of zero frequency). But with a large difference in particle number between L and R, even in a symmetric split potential, the mean-field energy differences would supply the necessary chemical potential differences for Josephson oscillations. This mean-field-induced chemical-potential difference can lead to many interesting experiments. But since this case is not necessary to the discussion here (and it was negligible for short times in our experiment), it will not be further considered here.

Now consider a confining potential that is split into a few segments instead of

just two, with high (but non-infinite) barriers, and a linear potential-energy gradient that is applied to the potential well. We can choose to consider basis states that describe particles that are localized in individual potential-well segments. We then return to the physics described above: localized basis states, and relative energy differences leading to oscillating probability currents. If the states are macroscopically occupied, we would call these oscillations a Josephson effect, even though there are more than two wells. (The Josephson effect is usually thought of in terms of a Josephson junction of two superconductors joined by a weak link.) Since the applied potential-energy gradient is linear, the oscillation frequencies between adjacent trap segments are identical. For all of the currents to be in-phase, the relative phases of the individual states must all be identical at some point in time.

We finally consider an infinitely long, tilted, periodic potential. What basis states should be used for determining the dynamics of the particles trapped in the potential? As in the above example, we can choose a basis where particles are approximately localized in individual wells. For this potential, this basis is the Wannier-Stark basis. An alternative basis would be the Bloch states, which describe de-localized particles, quantized in momentum. Depending on the energy gradient applied to the periodic potential, one basis might be more convenient than the other. In our experiment, the gravitational energy shift was strong enough that we used the Wannier-Stark basis, with particles in each state localizing in a small region around a corresponding lattice site. A weaker potential-energy gradient in this basis would lead to states that were localized to a lesser extent. Conversely, if the gradient were stronger, or if the barriers between the wells were higher, the states would be even more localized in individual potential-well segments.

The concepts of the two-well Josephson effect can be easily extended to the periodic potential to determine the dynamics of the system. This is a justified approach in our experiment because we are loading the trap from a single BEC, so the relative phases among the lattice sites are initially identical. One additional point may now be mentioned: there is a probability of atoms jumping into a higher-lying energy band, which for our configuration is a continuum of untrapped states. The probability of such a transition occurring is highest at the lower turning point of each oscillation, so

atom “pulses” are formed and fall at the Josephson oscillation frequency. The pulses, then, occur at points in time when the macroscopic wavefunctions of the lattice states are properly phased to constructively interfere in the continuum. An image of falling pulses is thus a single direct measurement of macroscopic interference.

A similar measurement could also be made with a single particle, without requiring a BEC. For this, we imagine a single particle in the ground state of the harmonic magnetic potential. We adiabatically apply the lattice, and then remove the magnetic field. The atom is trapped in the lattice for an undetermined time, and eventually falls from the lattice. We would take a picture to determine the position of the atom at a fixed time delay after putting the atom in the lattice. We could then do the identical experiment 10,000 times, add all of the images together, and the result should look like our single image of macroscopic interference. The physics in the two cases is the same, but the measurement is very different. This case would not be called a Josephson effect measurement since it does not involve macroscopically occupied states. However, the underlying physics (oscillations of probability currents due to time-domain interference resulting from energy differences) is the same.

The Josephson oscillations in our experiment can equivalently be called Bloch oscillations, as would be described by using the Bloch basis instead of the Wannier-Stark basis. The equations that describe the Josephson effect in a lattice map on to the equations that produce the Wannier-Stark wavefunctions. These in turn are an alternative (but equivalent) way of describing in an energy basis the physics that gives rise to Bloch oscillations in the Bloch (or momentum) basis.

The term “Bloch oscillation” does not imply (nor exclude) macroscopically occupied single-particle quantum states. The desired condition for observing Bloch oscillations is particles confined to the lowest energy band of a lattice. Bloch oscillations reveal the distribution of particles in momentum space, and are single-particle effects which can be observed without having a BEC. The observation of Bloch oscillations can not be considered a Josephson effect measurement, not because the physical principles are different, but because the terminology is applied to different conditions.

As an analogy, we point out that photon interference can be achieved with an

incoherent light source (a light bulb) if the interfering modes are sufficiently restricted. We do not need the concept of a laser in order to discuss interference and diffraction, which are single-photon effects. The light is not called a laser beam unless a large number of photons exist in a single cavity mode (generated, of course, by means quite different than the light of an ordinary light bulb). On one level, the difference is a matter of intensity. With the proper filters and mode selection, an ordinary light-bulb source can be made to emit the same frequency, bandwidth, and directionality as the output of a laser, but with *much* less intensity.

Similarly, the atomic tunnel arrays would still produce atom pulses if the periodic potential could be loaded from a trap above the BEC threshold. However, differences should be noticeable. First, the atoms would need to be loaded into the (longitudinal) ground states of the lattice. This would be more difficult to do with atoms above the BEC threshold. Second, atom pulses would probably be less-well defined. With a BEC, the coherence length of the trapped atoms extends over the entire trapped lattice states (at least), and destructive and constructive interference in the array output is expected. With the shorter coherence lengths that would exist in a non-BEC (but still very cold) sample, interference should not be as complete. Finally, experiments just above the BEC threshold may be difficult (and interesting) to interpret. Depending on the parameters of the magnetic and optical trapping potentials and the characteristics of the trapped atoms, the non-BEC atoms in the magnetic trap might undergo condensation by adiabatic application of the lattice [121].

Other confusing aspects arise due to terminology. For example, even with macroscopic wavefunctions, the “Josephson effect” term is usually only applied in situations where the degree of coupling between wavefunctions is within a certain range (placing the tunneling rates in a particular range) [104]. Also, the “Bloch oscillations” term is not applied to a single particle in a double well (where Bloch states are not relevant, though “delocalized” states can be considered). In our experiment, the term Josephson Effect is appropriate (by virtue of energy differences between macroscopic wavefunctions), as is the term Bloch Oscillation (by virtue of a tilted periodic potential). But in general, while the physical principles are extended to one limit or another, the terminology is not, leading to some confusion.

# Bibliography

- [1] T. Hänsch and A. Schawlow, *Opt. Comm.* **13**, 68 (1975).
- [2] D. Wineland and H. Dehmelt, *Bull. Am. Phys. Soc.* **20**, 637 (1975).
- [3] S. Chu, L. Hollberg, J. Bjorkholm, A. Cable, A. Ashkin, *Phys. Rev. Lett.* **55**, 48 (1985).
- [4] P. Lett, R. Watts, C. Westbrook, W. Phillips, P. Gould, H. Metcalf, *Phys. Rev. Lett.* **61**, 169 (1988).
- [5] J. Dalibard and C. Cohen-Tannoudji, *J. Opt. Soc. Am. B* **6**, 2023 (1989).
- [6] P. Ungar, D. Weiss, E. Riis, S. Chu, *J. Opt. Soc. Am. B* **6**, 2058 (1989).
- [7] E. Raab, M. Prentiss, A. Cable, S. Chu, D. Pritchard, *Phys. Rev. Lett.* **59**, 2631 (1987).
- [8] D. Weiss, B. Young, S. Chu, *Appl. Phys. B* **59**, 217 (1994); M. Kasevich and S. Chu, *Appl. Phys. B* **54**, 321 (1992).
- [9] T. Gustavson, P. Bouyer, M. Kasevich, *Phys. Rev. Lett.* **78**, 2046 (1997).
- [10] M. Snadden, J. McGuirk, P. Bouyer, K. Haritos, M. Kasevich, *Phys. Rev. Lett.* **81**, 971 (1998).
- [11] G. Timp, R. Behringer, D. Tennant, J. Cunningham, M. Prentiss, K. Berggren, *Phys. Rev. Lett.* **69**, 1636 (1992).
- [12] K. Gibble and S. Chu, *Phys. Rev. Lett.* **70**, 1771 (1993).

- [13] A. Clairon, C. Salomon, S. Guellati, W. Phillips, *Europhys. Lett.* **16**, 165 (1991).
- [14] T. Walker and P. Feng, *Advances in Atomic, Molecular, and Optical Physics* **34**, 125 (1994).
- [15] A. Hemmerich, C. Zimmerman, T. Hänsch, *Europhys. Lett.* **22**, 89 (1993).
- [16] G. Grynberg, B. Lounis, P. Verkerk, J. Courtois, C. Salomon, *Phys. Rev. Lett.* **70**, 2249 (1993).
- [17] S. Chu, J. Bjorkholm, A. Ashkin, A. Cable, *Phys. Rev. Lett.* **57**, 314 (1986).
- [18] M. Kasevich, D. Weiss, S. Chu, *Opt. Lett.* **15**, 607 (1990).
- [19] M. Renn, D. Montgomery, O. Vdovin, D. Anderson, C. Wieman, E. Cornell, *Phys. Rev. Lett.* **75**, 3253 (1995).
- [20] For example, see M. Kasevich and S. Chu, *Phys. Rev. Lett.* **67**, 181 (1991).
- [21] Nobel Prize in Physics 1997, Royal Swedish Academy of Sciences, Sweden (1997).
- [22] M. Anderson, J. Ensher, M. Matthews, C. Wieman, E. Cornell, *Science* **269**, 198 (1995).
- [23] C. Bradley, C. Sackett, J. Tollett, R. Hulet, *Phys. Rev. Lett.* **75**, 1687 (1995);  
C. Bradley, C. Sackett, R. Hulet, *Phys. Rev. Lett.* **78**, 985 (1997).
- [24] K. Davis, M.-O. Mewes, M. Andrews, N. van Druten, D. Durfee, D. Kurn, W. Ketterle, *Phys. Rev. Lett.* **75**, 3969 (1995).
- [25] D. Fried, T. Killian, L. Willmann, D. Landhuis, S. Moss, D. Kleppner, T. Greytak, *Phys. Rev. Lett.* **81**, 3811 (1998).
- [26] R. Hanbury Brown and R. Twiss, *Nature* **177**, 27 (1957).
- [27] B. Anderson and M. Kasevich, *Phys. Rev. A* **50**, R3581 (1994).
- [28] B. Anderson, T. Gustavson, M. Kasevich, *Phys. Rev. A* **53**, R3727 (1996).

- [29] B. Anderson and M. Kasevich, in preparation.
- [30] B. Anderson and M. Kasevich, *Phys. Rev. A* **59**, R938 (1999).
- [31] B. Anderson and M. Kasevich, *Science* **282**, 1686 (1998).
- [32] J. Kim, B. Friedrich, D. Katz, D. Patterson, J. Weinstein, R. DeCarvalho, J. Doyle, *Phys. Rev. Lett.* **78**, 3665 (1997).
- [33] See, for example, *J. Opt. Soc. Am. B* **6**, No. 11 (1989).
- [34] H. Lee, C. Adams, M. Kasevich, S. Chu, *Phys. Rev. Lett.* **76**, 2658 (1996).
- [35] N. Masuhara, J. Doyle, J. Sandberg, D. Kleppner, T. Greytak, H. Hess, G. Kochanski, *Phys. Rev. Lett.* **61**, 935 (1988).
- [36] For an excellent discussion of evaporative cooling of trapped atoms, see W. Ketterle and N. van Druten, *Advances in Atomic, Molecular, and Optical Physics* **37**, 181 (1996), and references therein.
- [37] For a discussion of light forces on a two-level atom, see J. Gordon and A. Ashkin, *Phys. Rev. A* **21**, 1606 (1980).
- [38] For a discussion of spontaneous and induced emission, see J. Sakurai, *Advanced Quantum Mechanics* (Addison-Wesley, Reading, MA 1978), pp. 36-41.
- [39] D. Wineland and W. Itano, *Phys. Rev. A* **20**, 1521 (1979).
- [40] C. Monroe, W. Swann, H. Robinson, C. Wieman, *Phys. Rev. Lett.* **65**, 1571 (1990).
- [41] For a review, see W.D. Phillips in *Laser Manipulation of Atoms and Ions*, Proceedings of the Varenna Summer School, edited by E. Arimondo, W. Phillips, and F. Strumia (North-Holland, Amsterdam, 1993), pp. 289-343.
- [42] V. Letokhov and V. Minogin, *Phys. Rep.* **73**, 1 (1981).



- [43] A. Migdall, J. Prodan, W. Phillips, T. Bergeman, H. Metcalf, *Phys. Rev. Lett.* **54**, 2596 (1985).
- [44] T. Bergeman, P. McNicholl, J. Kyacia, H. Metcalf, N. Balazs, *J. Opt. Soc. Am. B* **6**, 2249 (1989).
- [45] J. Tollet, C. Bradley, C. Sackett, R. Hulet, *Phys. Rev. A* **51**, R22 (1995).
- [46] T. Bergeman, G. Erez, H. Metcalf, *Phys. Rev. A* **35**, 1535 (1987).
- [47] W. Petrich, M. Anderson, J. Ensher, E. Cornell, *Phys. Rev. Lett.* **74**, 3352 (1995).
- [48] A. Einstein, *Sitzungsber. Kgl. Preuss. Akad. Wiss.* **1924**, 261 (1924); *ibid.* **1925**, 3 (1925).
- [49] A. Kastberg, W. Phillips, S. Rolston, R. Spreuw, P. Jessen, *Phys. Rev. Lett.* **74**, 1542 (1995).
- [50] J. Chen, J. Story, J. Tollet, R. Hulet, *Phys. Rev. Lett.* **69**, 1344 (1992).
- [51] S. Bose, *Z. Phys* **26**, 178 (1924).
- [52] S. de Groot, G. Hooyman, S. ten Seldam, *Proc. R. Soc. London Ser. A* **203**, 266 (1950).
- [53] See, for example, G. Baym and C. Pethick, *Phys. Rev. Lett.* **76**, 6 (1996).
- [54] P. Ruprecht, M. Holland, K. Burnett, M. Edwards, *Phys. Rev. A* **51**, 4704 (1995).
- [55] C. Sackett, J. Gerton, M. Welling, R. Hulet, *Phys. Rev. Lett.* **82**, 876 (1999).
- [56] D. Weiss, B. Young, S. Chu, *Phys. Rev. Lett.* **70**, 2706 (1993).
- [57] M. Kasevich and S. Chu, *Phys. Rev. Lett.* **67**, 181 (1991).
- [58] W. Ertmer, R. Blatt, J. Hall, M. Zhu, *Phys. Rev. Lett.* **54**, 996 (1985).
- [59] M. Zhu, C. Oates, J. Hall, *Phys. Rev. Lett.* **67**, 46 (1991).

- [60] W. Phillips, J. Prodan, H. Metcalf, *J. Opt. Soc. Am. B* **2**, 1751 (1985).
- [61] R. Gaggl, L. Windholz, C. Umfer, C. Neureiter, *Phys. Rev. A* **49**, 1119 (1994).
- [62] A. Cable, M. Prentiss, N. Bigelow, *Opt. Lett.* **15**, 507 (1990).
- [63] See, for example, W. Ketterle and D. Pritchard, in *Fundamentals of Quantum Optics III*, edited by F. Ehlotzky (Springer-Verlag, New York, 1993), pp. 77-89.
- [64] K. Lindquist, M. Stephens, C. Wieman, *Phys. Rev. A* **46**, 4082 (1992).
- [65] See, for example, A. Smith, K. Burnett, P. Julienne, *Phys. Rev. A* **46**, 4091 (1992).
- [66] J. Kawanake *et al.*, *Phys. Rev. A* **48**, R883 (1993).
- [67] N. Ritchie, E. Abraham, Y. Xiao, C. Bradley, R. Hulet, P. Julienne, *Phys. Rev. A* **51**, R890 (1995).
- [68] R. Hulet (private communication to Mark Kasevich).
- [69] K. Gibble, S. Kasapi, S. Chu, *Opt. Lett.* **17**, 526 (1992).
- [70] E. Riis (private communication to Mark Kasevich).
- [71] W. Ketterle, K. Davis, M. Joffe, A. Martin, D. Pritchard, *Phys. Rev. Lett.* **70**, 2253 (1993).
- [72] C. Westbrook, R. Watts, C. Tanner, S. Rolston, W. Phillips, P. Lett, P. Gould, *Phys. Rev. Lett.* **65**, 33 (1990).
- [73] P. Jessen, C. Gerz, P. Lett, W. Phillips, S. Rolston, R. Spreuw, C. Westbrook, *Phys. Rev. Lett.* **69**, 49 (1992);
- [74] P. Verkerk, B. Lounis, C. Salomon, C. Cohen-Tannoudji, J. Courtois, G. Grynberg, *Phys. Rev. Lett.* **68**, 3861 (1992).
- [75] A. Hemmerich and T. W. Hänsch, *Phys. Rev. Lett.* **70**, 410 (1993).

- [76] U. Drodofsky, J. Stuhler, B. Brezger, T. Schulze, M. Drewson, T. Pfau, J. Mlynek, *Microel. Engin.* **35**, 285 (1997).
- [77] S. Friebel, C. D'Andrea, J. Walz, M. Weitz, T. Hänsch, *Phys. Rev. A* **57**, R20 (1998).
- [78] A. Clairon *et al.*, in *1994 CPEM Digest*, edited by E. DeWeese and G. Bennett (New York, IEEE, 1994);
- [79] See articles K. Davis, M.-O. Mewes, M. Joffe, M. Andrews, W. Ketterle, *Atomic Physics 14*, edited by C. Wieman and D. Wineland (AIP, New York 1995); and W. Petrich, M. Anderson, J. Ensher, E. Cornell, *ibid.*
- [80] F. Moore, J. Robinson, C. Bharucha, P. Williams, M. Raizen, *Phys. Rev. Lett.* **73**, 2974 (1994).
- [81] M. Dahan, E. Peik, J. Reichel, Y. Castin, C. Salomon, *Phys. Rev. Lett.*, **76**, 4508 (1996).
- [82] D. Chaikovsky and G. Zaslavsky, *Chaos* **1**, 463 (1991).
- [83] T. Geisel, A. Zacherl, G. Radons, *Z. Phys. B* **71**, 117 (1988).
- [84] C. Myatt, N. Newbury, R. Ghrist, S. Loutzenheiser, C. Wieman, *Opt. Lett.* **21**, 290 (1996).
- [85] A. Bonch-Bruevich, T. Vartanyan, Yu. Maksimov, S. Przhibel'skii, V. Khromov, *Sov. Phys. JETP* **70**, 993 (1990).
- [86] M. Meucci, E. Mariotti, P. Bicchi, C. Marinelli, L. Moi, *Europhys. Lett.* **25**, 639 (1994). See also J. Xu, M. Allegrini, S. Gozzini, E. Mariotti, L. Moi, *Opt. Comm.* **63**, 43 (1987); and E. Mariotti, S. Atutov, M. Meucci, P. Bicchi, C. Marinelli, L. Moi, *Chem. Phys.* **187**, 111 (1994).
- [87] For a general discussion of adsorption and desorption, see Morrison, S. Roy, *The Chemical Physics of Surfaces*, second edition (Plenum Press) 1990; and R. Masel,

- Principles of Adsorption and Reaction on Solid Surfaces* (John Wiley & Sons, Inc.) 1996.
- [88] M. Anderson, W. Petrich, J. Ensher, E. Cornell, *Phys. Rev. A* **50**, R3597 (1994).
- [89] J. Ensher, D. Jin, M. Matthews, C. Wieman, E. Cornell, *Phys. Rev. Lett.* **77**, 4984 (1996).
- [90] M.-O. Mewes, M. Andrews, N. van Druten, D. Kurn, D. Durfee, W. Ketterle, *Phys. Rev. Lett.* **77**, 416 (1996).
- [91] W. Petrich, M. Anderson, J. Ensher, E. Cornell, *J. Opt. Soc. Am. B* **11**, 1332 (1994).
- [92] M. Andrews, M.-O. Mewes, N. van Druten, D. Durfee, D. Kurn, W. Ketterle, *Science* **273**, 84 (1996).
- [93] For a discussion of optimization of evaporative cooling, see, C. Sackett, C. Bradley, R. Hulet, *Phys. Rev. A* **55**, 3797 (1997).
- [94] See, for example, J. Goodman, *Introduction to Fourier Optics*, (New York, McGraw Hill, 1968).
- [95] M. Naraschewski and S. Stamper-Kurn, *Phys. Rev. A*, **58**, 2423 (1998).
- [96] S. Giorgini, L. Pitaevskii, S. Stringari, *Phys. Rev. A* **54**, R4633 (1996).
- [97] S. Grossman and M. Holthaus, *Phys. Lett. A* **208**, 188 (1995).
- [98] W. Ketterle and N. van Druten, *Phys. Rev. A* **54**, 656 (1996).
- [99] C. Sackett, C. Bradley, M. Welling, R. Hulet, *App. Phys. B* **65**, 433 (1997).
- [100] C. Bradley, C. Sackett, R. Hulet, *Phys. Rev. A* **55**, 3951 (1997).
- [101] M. Andrews, C. Townsend, H.-J. Miesner, D. Durfee, D. Kurn, W. Ketterle, *Science* **275**, 637 (1997);

- [102] M.-O. Mewes, M. Andrews, D. Kurn, D. Durfee, C. Townsend, W. Ketterle, *Phys. Rev. Lett.* **78**, 582 (1997).
- [103] E. Burt, R. Ghrist, C. Myatt, M. Holland, E. Cornell, C. Weiman, *Phys. Rev. Lett.* **79**, 337 (1997).
- [104] I. Zapata, F. Sols, A. Leggett, *Phys. Rev. A* **57**, R28 (1998).
- [105] For recent work with superfluid  $^3\text{He}$ , see, S. Pereverzev, A. Loshak, S. Backhaus, J. Davis, R. Packard, *Nature* **388**, 449 (1997); S. Backhaus, S. Pereverzev, A. Loshak, J. Davis, R. Packard, *Science* **278**, 1435 (1997).
- [106] B.D. Josephson, *Phys. Lett.* **1**, 251 (1962); see also, P. Anderson, *Basic Notions of Condensed Matter Physics* (Benjamin/Cummings Publishing Co., Menlo Park, CA, 1984) and references therein.
- [107] See, for example, A. Barone and G. Paternó, *Physics and Applications of the Josephson Effect* (John Wiley and Sons, New York, 1982).
- [108] See, for example, R. Feynman, *Lectures on Physics*, Vol. 3 (Addison-Wesley, New York, 1965), ch. 21.
- [109] See, for example, B. Taylor, W. Parker, D. Langenberg, *Rev. Mod. Phys.* **41**, 375 (1969).
- [110] See, for example, P.W. Anderson, in *Quantum Fluids*, D.F. Brewer, Ed. (John Wiley and Sons Inc., New York, 1966), p. 146-173; P.W. Anderson, in *Lectures on the Many-Body Problem*, E.R. Caianiello, Ed. (Academic Press, New York, 1964), p. 113-135.
- [111] H. Stoof, M. Houbiers, C. Sackett, R. Hulet, *Phys. Rev. Lett.* **76**, 10 (1995); M. Houbiers, R. Ferwerda, H. Stoof, W. McAlexander, C. Sackett, R. Hulet, *Phys. Rev. A* **56**, 4864 (1997).
- [112] T. Müller-Seydlitz, M. Hartl, B. Brezger, H. Hänsel, C. Keller, A. Schnetz, R. Spreew, T. Pfau, J. Mlynek, *Phys. Rev. Lett.* **78**, 1038 (1997).

- [113] A. Siegman, *Lasers* (University Science Books, Mill Valley, CA 1986).
- [114] E. Gross, *Nuovo Cimento* **20**, 454 (1961); L. Pitaevskii, *Sov. Phys. JETP* **12**, 155 (1961).
- [115] W. Press, B. Flannery, S. Teukolsky, W. Vetterling, *Numerical Recipes in C* (Cambridge University Press, Cambridge 1988), ch. 17.
- [116] F. Bloch, *Z. Phys* **52**, 555 (1928).
- [117] C. Zener, *Proc. R. Soc. London A* **145**, 523 (1934).
- [118] G. Wannier, *Phys. Rev.* **117**, 432 (1961); H. Fukuyama, R. Bari, H. Fogedby, *Phys. Rev. B* **8**, 5579 (1973); D. Emin and C. Hart, *Phys. Rev. B* **36**, 7353 (1987).
- [119] Observation of atomic Wannier-Stark ladders is reported in S. Wilkinson, C. Bharucha, K. Madison, Qian Niu, M. Raizen, *Phys. Rev. Lett.*, **76**, 4512 (1996).
- [120] From the probe absorption we infer a peak trap density of  $\sim 10^{13}$  atoms/cm<sup>3</sup>. Using the three-body loss coefficient from P. Fedichev, M. Reynolds, G. Shlyapnikov, *Phys. Rev. Lett.* **77**, 2921 (1996), we estimate a collision time of  $\sim 4 \times 10^3$  s.
- [121] D. Stamper-Kurn, H.-J. Miesner, A. Chikkatur, S. Inouye, J. Stenger, W. Ketterle, *Phys. Rev. Lett.* **81**, 2194 (1998).